WALL-SHAPED HIERARCHICAL MICROSTRUCTURE FOR GECKO-LIKE ATTACHMENT

A Dissertation
Presented to
The Academic Faculty

by

Jaekang Kim

In Partial Fulfillment
of the Requirements for the Degree
Doctor of Philosophy in the
George W. Woodruff School of Mechanical Engineering

Georgia Institute of Technology
December 2020

WALL-SHAPED HIERARCHICAL MICROSTRUCTURE FOR GECKO-LIKE ATTACHMENT

Approved by:

Dr. Michael Varenberg, Advisor
Woodruff School of Mechanical Engineering
Georgia Institute of Technology

Dr. David Hu
Woodruff School of Mechanical Engineering
Georgia Institute of Technology

Dr. Itzhak Green
Woodruff School of Mechanical Engineering
Georgia Institute of Technology

Dr. Daniel Goldman
School of Physics
Georgia Institute of Technology

Dr. Jeffrey Streator
Woodruff School of Mechanical Engineering
Georgia Institute of Technology

Date Approved: August 14, 2020

ACKNOWLEDGEMENTS

It has been a long hard journey to achieving my lifelong dream. I felt interested in mechanical engineering about 10 years ago. After then, I have always dreamed of becoming a teacher, engineer, and researcher in mechanical engineering. Now, I'm standing right behind the finish line as a student. Before completing the last step and moving forward to the first step as an independent researcher, I would like to express my sincere gratitude to the people who have believed in me, encouraged me, and supported me.

I would like to first thank my advisor, Dr. Varenberg. He allowed me to get involved in Biomimetics in Tribology and has always guided me in the right direction. It is my great honor to have him as my academic advisor and mentor. Furthermore, I would like to express my sincere thanks to my dissertation committee members, Dr. Green, Dr. Streator, Dr. Hu, and Dr. Goldman. I appreciate their valuable time and efforts to review my dissertation. Also, I would like to thank our lab members, Yingdan, Ye, and Yuan. Whenever I had hard times, they always helped me as my family. In addition, I would like to express my sincere gratitude to Dr. Whiteman, Dr. Donnell, Dr. Fedorov, and Ms. Henry, who have supported me and other ME graduate students in the department.

Last but not least, I would like to thank my family, friends, and everyone, who have always supported me during the long journey. No matter how far away you are or how different our lives become, I won't forget what you have done for me. Especially my father and brother, you mean the world to me. I love you always. Thanks for everything.

TABLE OF CONTENTS

LIST OF TABLES

LIST OF FIGURES

SUMMARY

Temporary biological attachment systems have long intrigued scientists and engineers because the animals that possess these systems are capable of climbing walls and even walking on ceilings irrespective of their surface properties. However, unlike prototype biological spatulate contact elements, which show a non-sticky default state, strong shear-induced attachment, and insensitivity to surface conditions, current biomimetic microstructured adhesives are deficient in these abilities. As an alternative to existing bio-inspired dry adhesives, a wall-shaped hierarchical microstructure has been suggested, but it is still unclear how loading and surface conditions, as well as material and geometrical properties affect the adhesive and frictional performance of the microstructure. It is also evident that its current mold-based manufacture can be considered impractical. To this end, the attachment performance of wall-shaped adhesive microstructures in various conditions, along with a new manufacturing technique, was examined, focusing on the following. 1) Developing a novel, cost-effective method for fabricating shear-activated biomimetic adhesives. 2) Finding the effects of loading condition (pre-load, pulling angle, and preliminary displacement), with the goal of gaining insight into how to use the adhesive microstructures. 3) Understanding the effects of the counterface surface conditions (topography and chemistry), with the goal of gaining insight into where to use the adhesive microstructures. 4) Investigating the effects of the microstructure shape and material properties, with the goal of gaining insight into what path to take to improve their attachment/detachment performance.

CHAPTER 1.   INTRODUCTION

1.1   Motivation

Bionics is employed in many areas, since nature can suggest solutions for the design of engineering systems based on millions of years of evolution by natural selection [1]. Natural materials and organisms have inspired countless technologies used in such fields as chemical engineering, robotics, optics, materials engineering, architecture, and so on [2-6]. Among the animals that have attracted scientific attention in this respect, the Tokay Gecko is one of the most studied ones, since the gecko lizard is the heaviest animal that can climb walls using its dry adhesive toe pads [7, 8]. Inspired by the gecko's attachment system, researchers tried to design dry adhesives that show strong adhesion and high reusability, leave no residues, and require no special counterface properties, the properties that are not seen in other technical attachment devices in current use.

The dry adhesives based on universal van der Waals forces [9] may have many industrial applications as pick-and-place or transfer tools, for instance, in the semiconductor industry [10]. Interestingly, existing wafer transfer robots mainly rely on the use of vacuum grippers [11]. However, due to relatively high contact pressure and cyclic loading in chucking incoming wafers, the stiff contact elements of the transfer grippers wear and contaminate the working environment [12], which is a critical issue in the semiconductor industry. In addition, vacuum-operated systems are complex and expensive [13]. Other sectors, such as household, medicine, sports, aerospace, etc. could also find use for more efficient, cost-effective, clean, easily detachable and simple bio-

inspired grippers. However, much more research is needed before bio-inspired dry adhesives are widely employed for industrial and domestic use.

1.2 State of the Art

Thin-film-ended hairy adhesive structures have evolved independently in insects, arachnids, and reptiles to secure their locomotion on substrates of arbitrary orientation, geometry and chemical composition as shown in Figure 1-1 [14, 15]. These micro- and nanoscale structures have drawn significant interest during the last two decades and numerous attempts were made to reconstruct their abilities [7, 8, 16-21].

Direct replication of adhesive hairs represents a technological challenge due to their complex hierarchical geometry [17, 22, 23], and careful abstraction and simplification have to be exercised to create an attachment surface mimicking their robust performance. Since it was revealed that terminal thin-film elements operate using intermolecular [7, 9] and, possibly, also capillary [24, 25] forces, which allowed these structures to be replicated with engineering materials, much effort has been put into the development of biomimetic adhesive surfaces [26, 27]. Consequently, several types of biomimetic microstructured adhesive surfaces were suggested based on simple shapes of pillar, mushroom, wedge and flap geometries, as shown in Figure 1-2 [26-35].
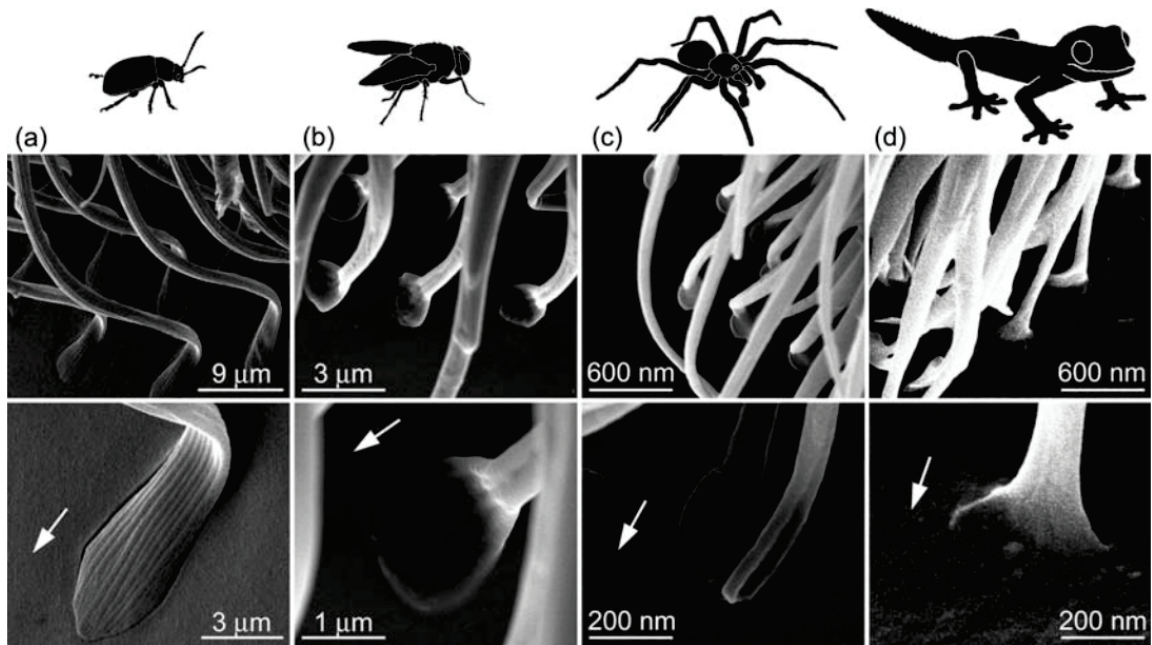
Figure 1-1 – Cryo-SEM images of spatula-shaped thin-film terminal elements, while in contact with smooth glass, in hairy attachment pads found in animals of evolutionary remote lineages. (a) Beetle (G. viridula). (b) Fly (C. vicina). (c) Spider (C. salei). (d) Tokay gecko (G. gekko). Arrows point in distal direction [15].
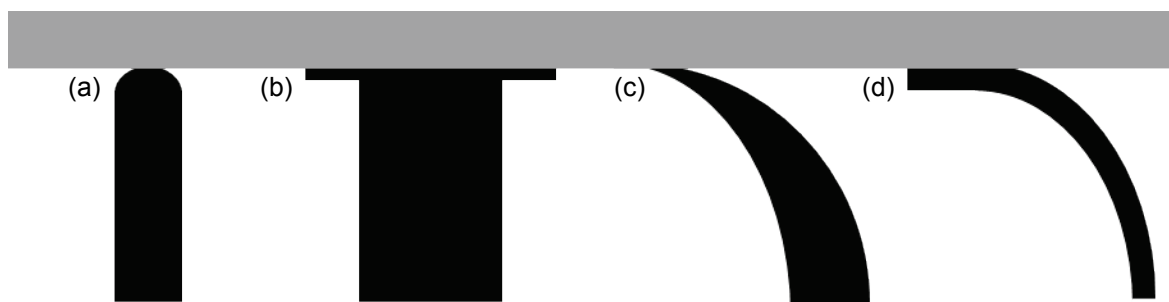
Figure 1-2 – Simple biomimetic structures having (a) pillar-, (b) mushroom-, (c) wedge- and (d) flap-shaped geometry of contact elements.

Due to its simplicity, a pillar-shaped structure was the first utilized to try making a dry adhesive [34, 35]. However, the structure showed poor adhesion compared to a smooth flat [36]. A mushroom-shaped structure [28], mimicking the hairs evolved in male leaf beetles for passive long-term attachment during pairing, demonstrated greater pull-off force compared to smooth flat surfaces. While the mushroom-shaped structure remains the most thoroughly studied to date due to the well-established manufacture procedures [37], it could not be detached with a zero force, which means that it is hard to control the adhesion, unlike biological attachment systems. Eventually it was understood that shear-induced (directional and controllable) attachment, which is the key feature of biological hairy structures employing thin-film adhesion, characterizes only the wedge- and flap-shaped microstructures [30-32] that most closely resemble biological spatulate contact elements found in all hairy attachment pads regardless of the animal group.

There have been many attempts to utilize dry adhesives in robotic applications because the artificial structures have performed reasonably well on smooth substrates, which makes them suitable for such industrial applications as silicon wafer or display panel handling [38-40]. Wall-climbing gecko-inspired robots have been also developed and studied with the help of reversible dry adhesives, which can secure locomotion against smooth walls without the aid of glue, suction, electromagnetic forces, etc. A gecko-like climbing robot [41] and even a climbing device for a human being [42] were made for operation on a vertical smooth glass wall. Because dry adhesives can work in vacuum conditions, thanks to the van der Waals interaction that operates between any pair of materials in contact, NASA Jet Propulsion Laboratory has also tried to implement this technology in their gecko-inspired robot for use in space [43] (Figure 1-3a).

4

Pick-and-place robots have shown great potential to be improved by using dry adhesives. Since these adhesives can be repeatedly used and do not leave a trace on the contacted surface due to a low contact pressure, they can be used in the consumer electronics industry, which requires highly precise and clean transfer of products. In line with the above, OnRobot has produced gecko-inspired grippers designed for such uses [44] (Figure 1-3b). With 140 N of preload, their newest version of gecko gripper can lift up to 6.5 kg of polished mirror-like steel or solar panel. However, although the mushroom-shaped adhesive can generate a high attachment force, it requires high detachment force as well due to the non-directionality of the structure. In addition, while the friction of wedge- or flap-shaped adhesive microstructures was reported to be rather strong, their adhesive performance is still not comparable to that of biological attachment systems, such as in geckos, on horizontal overhung surfaces [45-47].
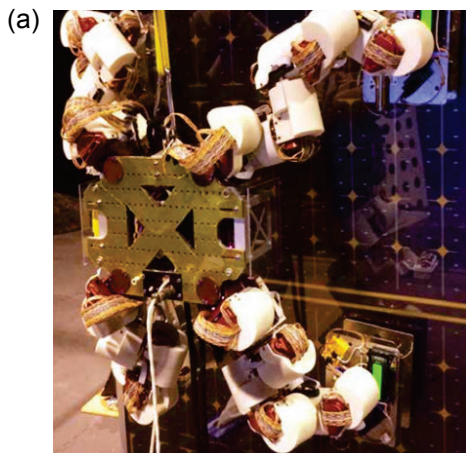
Figure 1-3 – (a) Limbed excursion mechanical utility robot developed by NASA Jet Propulsion Lab and (b) OnRobot Gecko Gripper commercially available for pick-and-place machine.

In addition to the limitations in performance of today's bio-inspired dry adhesives, manufacturing these adhesives is still a time-consuming and complicated task. Currently, these adhesives are manufactured using template-based molding, with the templates being fabricated using such techniques as photolithography, laser micromachining, and ultraprecision cutting [32, 40, 45, 48, 49]. The main fabrication technique employed so far is photolithography [45], which is a well-defined process composed of several mechanical, optical and chemical procedures. However, various expenditures associated with the preparation of molding templates call for research on other manufacturing techniques. An alternative approach to molding dry adhesives using templates can be based on a much simpler drawing technique. It was reported earlier that a process of dipping an AFM probe or a thin wire into an SU-8 solution, then drawing it back and holding it until the SU-8 has polymerized can be used to create high-aspect ratio fibers of a μm-scale diameter [48, 50], which cannot be easily obtained using typical molding techniques. PMMA was also shown to develop similar high-aspect ratio structures whose geometry depended on polymer viscosity, temperature, and drawing speed [51-54].

As an effort to overcome performance limitations, a wall-shaped adhesive microstructure [33] has been fabricated recently. The wall-shaped geometry was designed to have a significantly longer total peeling line [15] (the sum of lengths of all cracks opening at the same time between the thin-film-based contact elements and the counterface) compared to an adhesive array composed of fibrillar projections. This can be explained by the Kendall's thin-film peeling model [55] (Figure 1-4a). The peeling force F can be expressed using the film width b, Young's modulus E, film thickness d, fracture energy R, and peeling angle θ as follows.

$$F = bdE \left\{ (cos\theta - 1) + \sqrt{(\cos\theta - 1)^2 + \frac{2R}{dE}} \right\}$$ (1)

As can be seen in Eq. (1), the peeling force F is proportional to the film width b, not the real contact area. Hence, this suggests that by increasing the total peeling length through contact splitting within the same contact area, the total peeling force per unit area can be greatly improved as shown in Figure 1-4.
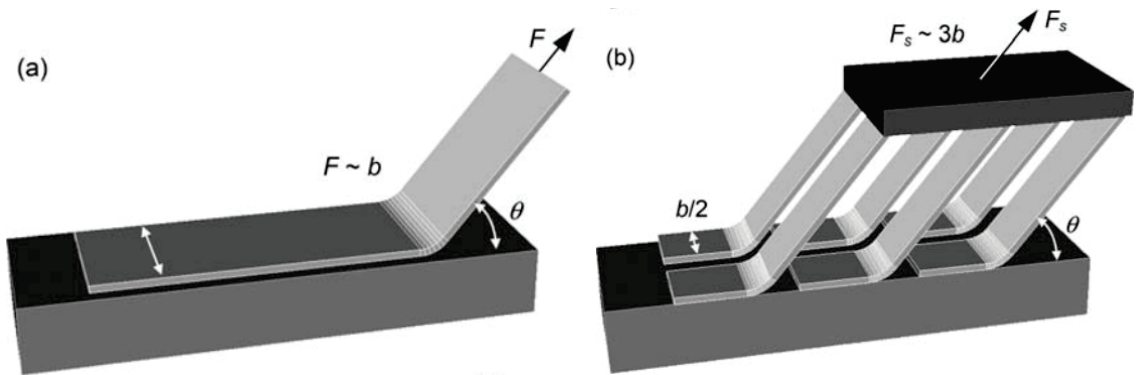
Figure 1-4 – Graphical representation of the effect of adhesion enhancement by increasing the peeling line length. (a) A single piece of elastic film peeling from a rigid substrate. Peeling force F is proportional to the film width b (at constant peel angle θ for given pair of materials). (b) A series of elastic films covering the same contact area as in (a). Peeling force Fs is threefold the value F in (a) due to an overall growth of the peeling line length calculated as a sum of individual film widths [15].

With the help of an extended total peeling line length, as well as increased flap height and reduced flap thickness, the wall-shaped adhesive microstructure showed significantly higher friction than other structures, which suggests that the current dry adhesive paradigm of fibrillar projections can be re-examined. Moreover, the templates for making wall-

shaped microstructures were prepared by laser-micromachining, which is much simpler than photolithography and has better scaling-up potential.

The performance of bio-inspired dry adhesives has been studied under different loading, surface and environmental conditions. For shear-induced attachment, the main loading parameters are the tangential displacement, for which a dry adhesive is dragged prior to pulling, and the angle, at which it is pulled off of the substrate [7, 56, 57]. Thus, load-drag-pull test is generally used to measure a shear-induced attachment [45], with some bio-inspired adhesives showing quantifiable attachment ability. To allow for a better representation of the shear-induced attachment test results, an adhesion circle (a graph that indicates the pull-off force with respect to an azimuthal pulling angle or drag displacement) has been recently suggested [58]. However, to our knowledge, the effect of combination of the drag displacement and pulling angle on the attachment performance of these dry adhesives has not been investigated yet.

Several counterface roughness studies performed with artificial fibrillar adhesive structures reported that the attachment abilities of these structures are significantly reduced with increasing roughness. Because the ultimate goal of mimicking biological adhesives is to achieve efficient and easily controllable adhesion on any surface, it is important to understand how to overcome the negative effects of roughness on attachment of thin films. It was shown that gecko adhesion is lower if the substrate waviness wavelength is comparable to the length of the lamella (low-level-hierarchy attachment element) and the inter-lamella spacing, and if the substrate roughness is comparable to the lateral dimension of a single spatula (high-level-hierarchy attachment element) [59, 60]. Several studies performed with artificial fibrillar structures reported that their attachment abilities are

8

reduced if the fibril dimensions are similar to the root-mean-square roughness, the mean spacing between local peaks, and the surface waviness characteristics of the substrate [61-64]. Analogous negative effects of roughness on the adhesion and friction of biomimetic thin-film based structures were also recently demonstrated [65-69], although positive effects associated with an increase in roughness were reported as well [70]. In general, splitting a large contact area into finer sub-contact areas is thought to result in higher adaptability to rough surfaces, stronger adhesion, and more uniform stress distribution with higher tolerance to defects [15, 71-75]. However, although it is generally believed that contact splitting helps to mitigate the negative effects of roughness on adhesion- and friction-based attachment [64, 71, 73], no decisive experimental validation of this hypothesis has been performed so far for thin-film-based adhesives.

Surface chemistry, which defines surface free energy, is also a significant factor that determines the adhesion between two contacting objects [76, 77]. Although surface chemistry is less important than surface geometry, it may still prevent establishment of reliable attachment in some cases. For instance, geckos, which are known to be the heaviest animals able to run in an overhanging position [8], exhibit poor adhesion on a PTFE surface [78, 79]. It was also shown that adhesive force between a gecko seta and a surface is strongly related to the water contact angle (θ) of the counterface and is proportional to $\sqrt{1 + cos\theta}$ for $\theta > 60°$ [80, 81]. Beetles cannot escape Glass containers coated with Fluon [82]. Synthetic dry adhesive based on Carbon nanotubes was also reported to perform worst when tested against a Teflon substrate [83].

Surface free energy, which is determined by surface chemistry and defines attractive forces between contacting surfaces, is composed of several parts that can be

attributed to dispersion interaction, dipole-dipole interaction, dipole-induced dipole interaction, hydrogen bonding, π-bonding, electrostatic interaction and acceptor-donor interaction [84]. Considering this variety, one may expect that some materials can be more universal than others in their adhesive interaction with random counterfaces, and, hence, be preferable for dry adhesives.

The polymeric materials that have been used for this purpose so far are polydimethylsiloxane (PDMS), polymethyl methacrylate (PMMA), polypropylene (PP), polyvinylsiloxane (PVS), polyurethane (PU), and polyurethane acrylate (PUA) [45, 85]. Given that PU is also widely used in industry due to its high resistance to cutting, wear, fatigue and chemicals [86], it is interesting to test its adhesive capabilities in response to various counterface chemistries. However, to our knowledge, no direct studies on the relationship between surface free energy and pull-off force of biomimetic adhesives have been performed yet.

In addition, the effects of the durability/repeatability, humidity/temperature, and contamination have been studied. The durability was investigated by repeated loading tests [30, 87-89]. It was shown to depend strongly on material; with polydimethylsiloxane (PDMS) adhesives demonstrating durability of over 10,000 cycles, and polyurethanacrylate (PUA) adhesives having durability of less than 100 cycles. It was reported that an ultrathin platinum coating of less than 10 nm can increase the durability of dry adhesives, although this coating undermines their attachment abilities [89].

The humidity/temperature effect on the pull-off force was studied in relation to capillary action [90-92]. Although the attractive force was found to arise mainly due to van

der Waals forces [9], it was shown that humidity is also important and that there is an optimum humidity to reach a peak performance of dry adhesives [90]. It was also found that adhesion of a biomimetic mushroom-shaped adhesive is more sensitive to humidity at low temperature than at high temperature, which is also observed in attachment of live geckos [93].

Since it was revealed that geckos' toe pads have a self-cleaning ability [16, 94] which ensures the repeatable attachment even after contact with a dirty surface, there were attempts to make dry adhesives that have the self-cleaning ability and to test the self-cleaning ability of artificial dry adhesives [95-101]. Contamination effects on the pull-off force were reported in terms of the dry/wet self-cleaning ability and the contaminant size dependency [95-97]. It was shown that the ratio of the contaminant size to the characteristic size of the adhesive structure strongly affects the self-cleaning ability of the adhesive structure. In these studies, the diameter of the contaminant particles associated with the dimension of adhesive structures was the most important factor that determined the recovery of the peeling force. In general, pillar-shaped adhesive structures [97, 98] showed better self-cleaning ability compared to wedge- and flap-shaped adhesive structures [100, 101] while their attachment performance was inferior to that of the wedge- and flap-based structures.

1.3   Problem Statement & Research Goals

In light of the above, it is clear that we have to gain better understanding of the mechanisms involved in dry adhesion to design efficient biomimetic dry adhesives. This includes (a) verification of the very basic concept of the pulling angle optimum [55, 102, 103], which has not yet been examined, and its correlation to normal pre-load and preliminary tangential displacement; (b) investigation of the effects of surface conditions such as surface chemistry and surface roughness, and validation of the hypothesis that contact splitting helps to mitigate the negative effects of roughness on adhesion- and friction-based attachment; and (c) studies of the effects of material and geometrical properties on shear-induced attachment performance. Furthermore, it is also necessary to develop a simple scalable manufacturing method to pave the way for the future use of this promising technology.

To this end, in this work, we systematically studied the effect of pulling angle on the normal and tangential components of the pull-off force at different preliminary tangential displacements using wall-shaped adhesive microstructures of different heights. In addition, the effect of pre-load on the frictional and adhesive performances was investigated. We also examined the adhesive and frictional behavior of the original and carefully split wall-shaped adhesive microstructures on different surfaces ranging across several orders of magnitude in roughness. The effect of pre-load on sliding inception on rough surfaces was studied as well. In order to allow future engineering of successful biomimetic dry adhesives, we investigated the correlations between the attachment performance of the wall-shaped adhesive microstructure and such properties as surface free energy, Young's modulus, and the microstructure geometry. Lastly, considering that drawing technique

showed its utility in manufacturing microscale fibrillar structures [48, 51] while no direct attempt to manufacture biomimetic adhesives this way has been made yet, we systematically studied the drawing-based approach to the fabrication of the wall-shaped adhesive microstructures.

It is also worth mentioning here that although durability and environmental conditions are known to affect the adhesive and frictional performance of dry adhesives, these parameters were not examined in our study due to the lack of time. These secondary (compared to the above) parameters will be left to future studies.

CHAPTER 2.   METHODS AND MEANS

In this chapter, the manufacturing techniques used to fabricate our wall-shaped adhesive microstructures are covered. Currently, microstructured dry adhesives are prepared using template-based molding, and the templates are fabricated by such techniques as photolithography (the most popular manufacturing technique) and super-precise cutting [40, 45, 104]. However, these templates are expensive to prepare, and their manufacturing requires substantial time. In addition, one template can be used only for preparation of one specific shape of a structured sample. To overcome these shortcomings, we started with laser micromachining for template preparation and later developed a novel cost-effective and simple drawing-based approach to the manufacture of dry adhesives. All equipment used in this study to test and characterize the adhesive microstructures and their counterfaces is also presented here.

2.1   Experimental Setup

2.1.1   Force Testing

All force tests were carried out in a custom-built tribotester [105] (Figure 2-1). The tribotester incorporates two main units used for driving and measuring purposes. The drive unit consists of three motorized translation stages (two M-111.1DG and one M-227.10, Physik Instrumente, Karlsruhe, Germany) used to load the contact by moving the counterface specimen. The measurement unit consists of two S-beam load cells LSB200-50g (FUTEK, Irvine, CA) used to determine the forces acting on the tested specimen. The

load cells are fixed in such a way that normal force acts in the plane in which the tangential load cell is not sensitive, and tangential force acts in the plane in which normal load cell is not sensitive, thus preventing crosstalk between force sensors. To guarantee full contact and fulfill the 'equal load sharing' principle during force measurements in a flat-on-flat contact scheme essential in surface texture testing, a passive self-aligning system of specimen holders was used.

To provide on-line monitoring of the contact response, a multifunctional data acquisition board PCI-6251 and a servo motion controller board PCI-7344 (National Instruments, Austin, TX) installed in a supportive PC station are integrated using a LabVIEW software package. The signals going into and out of the PC boards are amplified using a 4-axes motion I/O interface C-809 (Physik Instrumente, Karlsruhe, Germany) and two strain gage amplifiers AE101 (HBM, Darmstadt, Germany). Before use, the load cells were calibrated with standard weights.
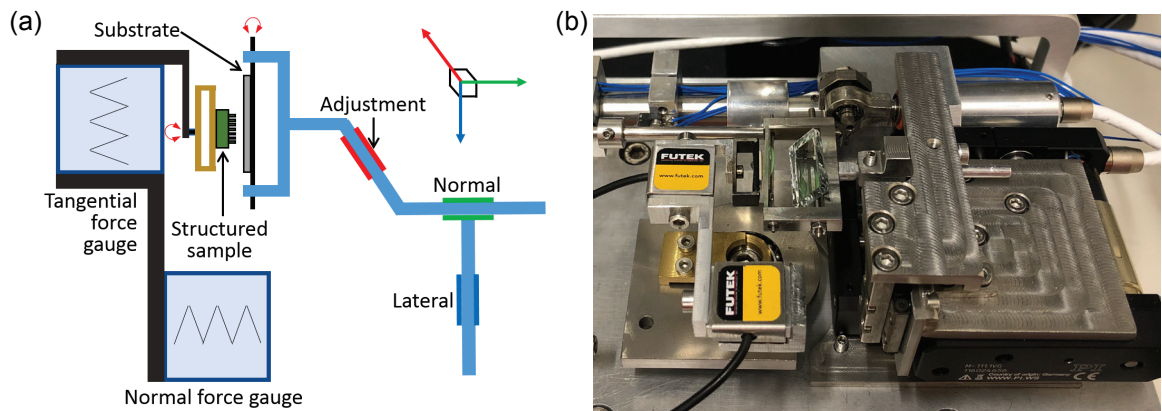
Figure 2-1 – Custom-built tribotester used in this study. (a) Schematic of the tribotester and (b) Image of the tribotester.

2.1.2 Surface Characterization

In addition to force measurements, it is also very important to investigate how the adhesive microstructure behaves when relative motion is generated between the structure and the substrate. Hence, as shown in Figure 2-2, the custom-built tribotester was designed to operate inside a Quanta 250 environmental scanning electron microscope (SEM; FEI, Brno, Czech Republic). The SEM was also used without the tribotester to observe the substrate topography and the adhesive microstructure in high resolution. When the tribometer was operated outside the SEM, a monochrome digital camera DMK 23UP1300 (Imaging Source, Charlotte, NC) mounted on a high-magnification optical lens Zoom-12X (Navitar, Rochester, NY) was used to ensure the alignment of the structured sample and to capture images of the real contact area, which was visualized due to light interference at the interface.
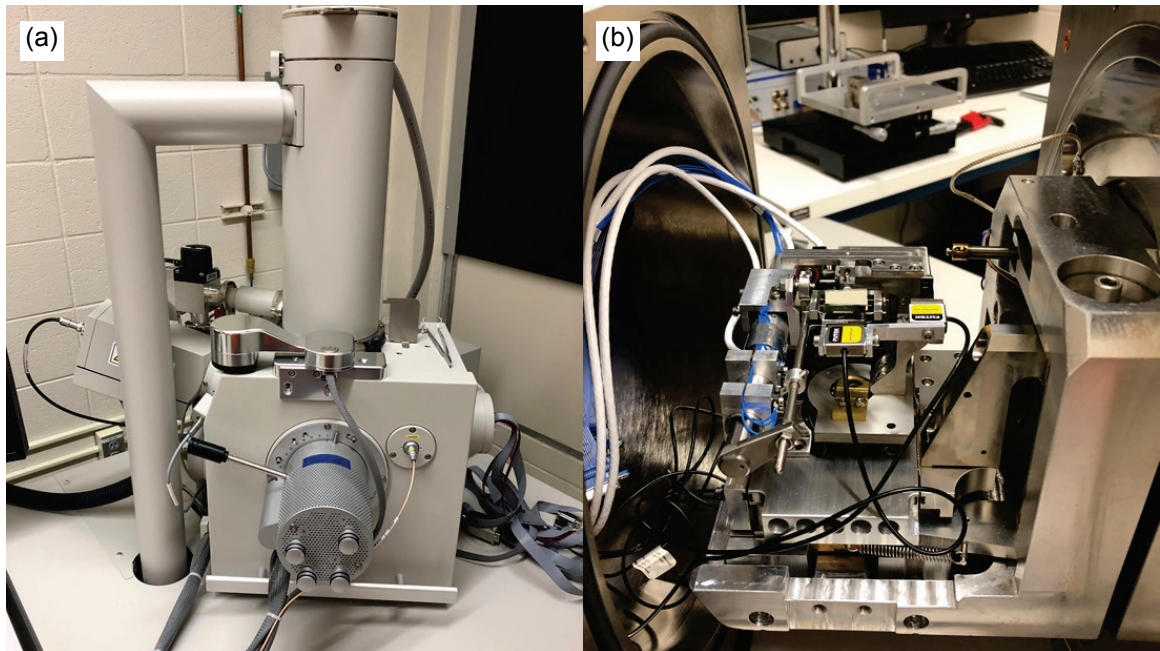
Figure 2-2 – (a) Image of Quanta 250 environmental Scanning Electron Microscope (SEM) and (b) the custom-built tribotester assembled in the SEM.

All tested structured samples and substrates were inspected with an M125 optical stereomicroscope (Leica, Wetzlar, Germany) shown in Figure 2-3a. The surface topography was examined with a vertical resolution of < 1 nm and a lateral resolution of about 0.1 µm using a 3D optical profiler ContourGT-I (Bruker, San Jose, CA) shown in Figure 2-3b. A contact angle measurement system OCA 25 (DataPhysics Instruments, Filderstadt, Germany) shown in Figure 2-3c was used to quantify surface free energy by dosing different test liquids on the substrate placed on a manual stage and studying the droplet shapes with a camera in front of the sample.
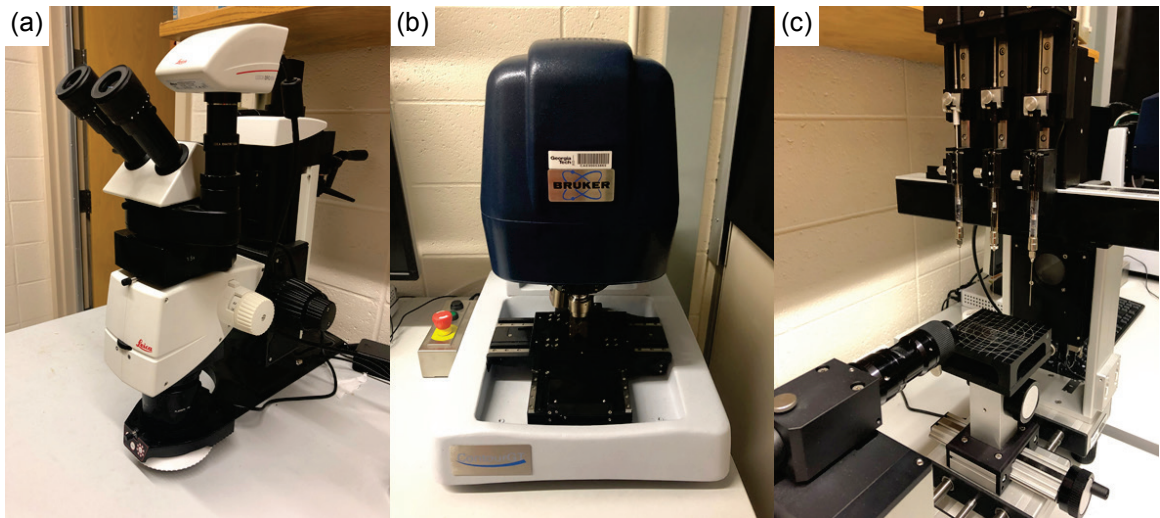
Figure 2-3 – Equipment for surface characterization. (a) M125 optical stereomicroscope, (b) 3D optical profiler ContourGT-I, (c) Contact angle measurement OCA 25.

2.1.3 Auxiliary Equipment
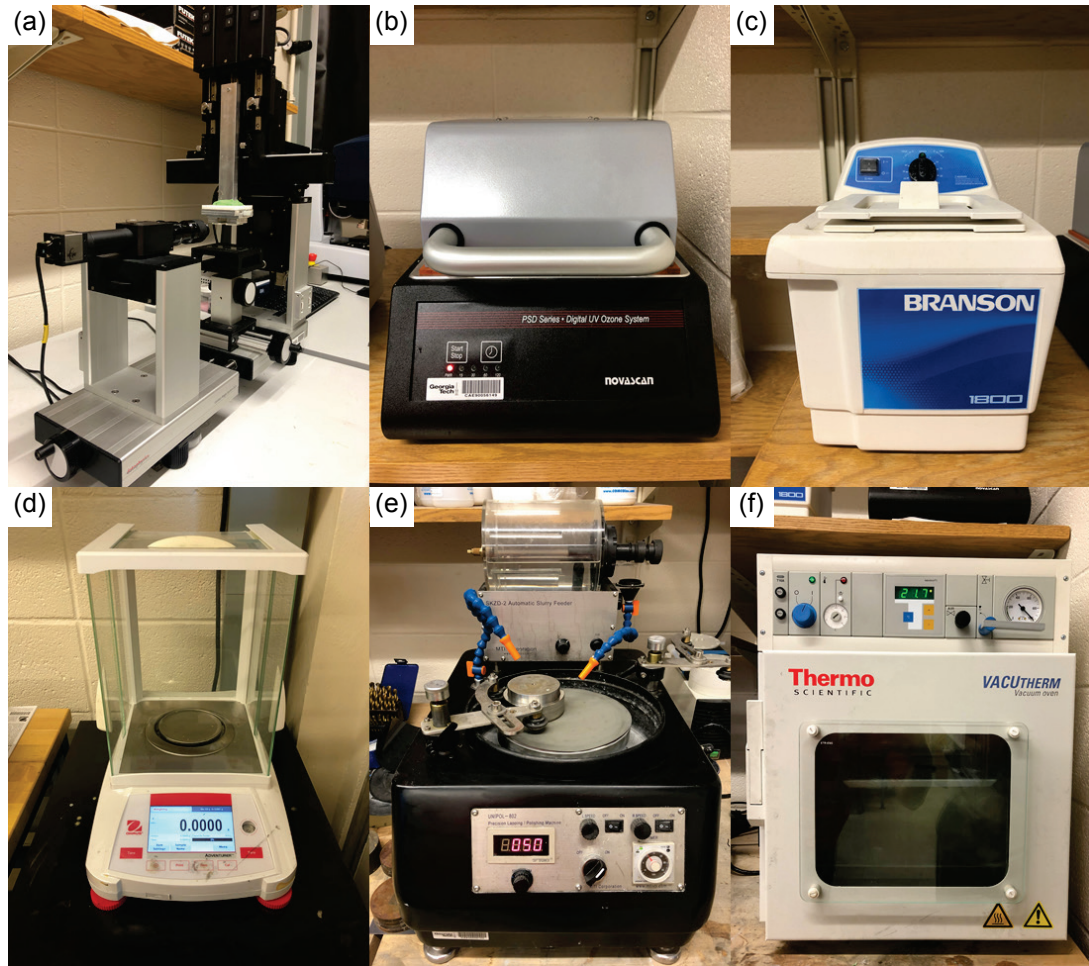
Figure 2-4 – Auxiliary equipment used in this study. (a) Contact angle measurement system modified for drawing-based manufacturing, (b) Ozone cleaner PSD-UV4, (c) Ultrasonic bath M18000H, (d) Analytical balance AX324, (e) Polishing machine Unipol-802, (f) Vacuum oven Vacutherm.

As shown in Figure 2-4a, the dosing unit of the contact angle measurement system was replaced with a drawing array holder to fabricate wall-shaped adhesive microstructures using a drawing-based technique, while the camera was employed to control the process. Several other devices, namely, ozone cleaner PSD-UV4 (Novascan Technologies, Ames,

IA), water-filled ultrasonic bath M1800H (Branson Ultrasonics, Danbury, CT), analytical balance AX324 (OHAUS, Parsippany, NJ), polishing machine Unipol-802 (MTI Corporation, Richmond, CA), and vacuum oven Vacutherm (Thermo Fisher Scientific, Waltham, MA), were used to assist at various stages of this study. In addition, while the temperature in the laboratory was kept at around 25 °C by the air-conditioning system, the relative humidity was adjusted to be within 45-55 % by a humidifier U350 (BONECO, Widnau, Switzerland) and a dehumidifier LG PuriCare 55 Pint (LG, Seoul, South Korea) that were operated depending on the weather outside.

2.2   Molding-Based Manufacturing

2.2.1   Fabrication Steps

As shown in Figure 2-5a, microstructured surfaces were molded from polyvinylsiloxane (PVS; Coltène Whaledent, Altstätten, Switzerland; Young's modulus of about 3 MPa [106]) against a grid of varying cross-section prepared by laser micro-machining (Oxford Lasers, Shirley, MA) from a tungsten sheet of 0.15 mm in thickness (Figure 2-5b). To facilitate the mold release, which was performed in a water bath, the tungsten grid was oxidized in ozone cleaner for 30 min before each molding. Waiting 100, 105 or 110 s between mixing the two-compound PVS and pouring the polymerizing mixture onto the grid allowed us to create wall-shaped projections of three different heights 140, 100 or 70 μm, respectively. This was possible because the curing PVS stopped sinking into the grid after it reached a certain degree of polymerization at a set time of about 3 min. The dwell times were found experimentally, fitting to $H = 116 \cdot 10^3 \cdot 0.935^t$, where H is

19

the height in μm and *t* is the time in s. The mold backing layer was made to have thickness

of 1 mm by using spacers between the grid and a flat cover. The PVS was kept at 4 ℃

before mixing and was polymerized during 10 min at room temperature. The mold was

gently released from the grid after it was held in a water-filled ultrasonic bath for 30 min.

2.2.2 Molded Microstructures
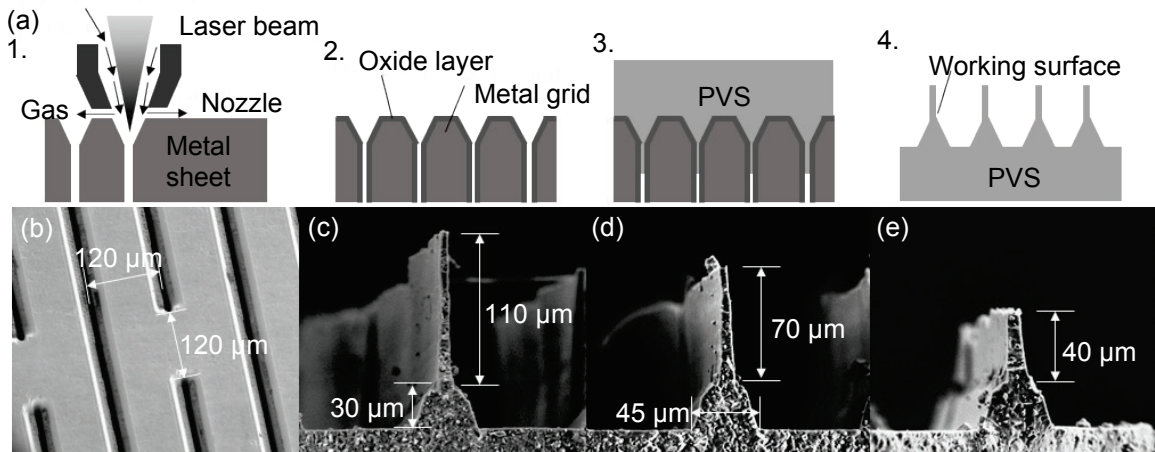
Figure 2-5 – Wall-shaped hierarchic adhesive microstructures. (a) Schematic of the fabrication steps. 1. Laser micro-machining. 2. Plasma treatment. 3. Molding. 4. Release. (b) SEM image of the W grid used as a molding template. (c), (d), (e) SEM images of single wall-shaped projections with the same triangular bases and different flap heights.

Figure 2-5c-e shows SEM images of single wall-shaped adhesive microstructures

manufactured using the molding-based technique. The triangular base in these

microstructures was the same (width: 45 μm, height: 30 μm) while their flap heights

differed as a function of the waiting time before mixing the two compounds of PVS and

pouring the mixture onto the template. The flap heights of 110 μm, 70 μm, and 40 μm were

obtained to examine the effect of the flap height on attachment performance of the wall-shaped adhesive microstructures.

2.3   Drawing-Based Manufacturing

2.3.1   Fabrication Steps

The procedure we developed for drawing thin-film-based microstructures is shown schematically in Figure 2-6 [107]. First, a drawing array was assembled from uniformly spaced and aligned elements, and a uniform polymer layer was smeared on a substrate. We used common thick and thin (marked as K and N, respectively) laboratory razor blades as single drawing elements and office adhesive tape pieces as spacers between blades, while the blades faced the polymer with either sharp (V-shaped) or blunt (U-shaped) edges. The two-component polymer (polyvinylsiloxane, PVS, or polyurethane, PU) was mixed and left to cure partially before being smeared, so the increased polymer viscosity allowed it to stay on the substrate without flowing out. The spacers used to control the polymer layer thickness, which should not be much larger than the gap between drawing elements to prevent capillary rise, were prepared from the same adhesive tape.
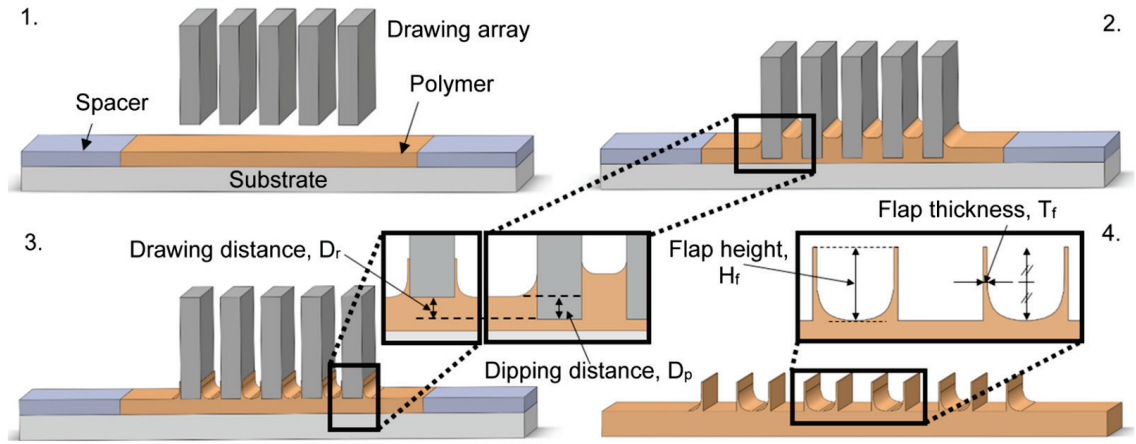
Figure 2-6 – Drawing-based manufacturing process and definitions of characteristic parameters. 1. Preparation of the drawing array and a polymer layer with uniform thickness 2. Dipping the drawing array into the polymer layer. 3. Drawing the tips out of the polymer layer. 4. Release of a cured structured surface.

Second, the drawing array was dipped into the polymer layer to a designated distance at a designated speed and at a designated time, which was also measured from the instant of mixing together the polymer components. Based on discussions in the literature on dip coating processes [108-111], the dipping stage is less important than the drawing stage. However, the dipping distance, speed and time have to be chosen carefully. The dipping distance cannot be much shorter than the drawing distance due to a possible necking and subsequent disconnection between the drawn flaps and the backing polymer layer. The dipping speed has to be as low as possible to minimize formation of wrinkles on the polymer surface [112, 113]. The dipping time has to be chosen close to the drawing time, which is also measured from the instant of mixing, in order to minimize capillary rise of the polymer through the gap between drawing elements, which disrupts the fabrication of high-aspect ratio microstructures.

Third, the drawing array was withdrawn from the polymer, with the drawing distance, speed, and time being the most important parameters determining the geometry of the microstructured surface. We focus on the effects of these three parameters in the following sections.

Last, the drawing array was held motionless with respect to the substrate until the polymer was completely cured and then the ready-to-use microstructured surface was finally released.

Before the actual fabrication could be performed, the effects of main processing parameters were examined to understand how to control the process. To study the drawing distance effect, all fabrication tests were conducted with the dipping distance of 180 µm and the drawing speed of 600 µm/s. To study the drawing speed effect, the dipping and drawing distances were chosen large enough (ranged from 36 to 240 µm) to get a uniform thickness along the flaps. For each test point, the flap height and thickness were measured at 10 different locations using the SEM.

2.3.2 Effect of Drawing Time

To draw high-aspect ratio flaps upwards and have them fully cured before the polymer can sink back down, the polymer should have a certain viscosity. On the other hand, if the polymer is too viscous, the drawn flaps are excessively stressed, which leads to wrinkles or pores on the cured surface that affect detrimentally its adhesive performance.

To this end, working with polymers that cure over time requires knowing time-dependent viscosity before finding the time at which flaps can be drawn.

The viscosities of curing PVS and PU mixtures were evaluated by studying their capillary rise in glass tubes as a function of time. The governing equation for a capillary flow in the vertical direction [114, 115] can be expressed as

$$\frac{8\eta}{r^2} h \frac{dh}{dt} + \rho g h = \frac{2\gamma \cos\theta}{r} \tag{2}$$

where η is the liquid viscosity, r is the capillary tube radius, h is the capillary rise height, t is the time until the liquid reaches the height h, γ is the surface tension of the liquid, θ is the contact angle between the liquid and the capillary tube, ρ is the liquid density and g is the gravitational acceleration. Solving Eq. (2) yields

$$t = \frac{8\eta}{\rho g r^2} \left(\frac{2\gamma \cos\theta}{\rho g r} \ln \frac{2\gamma \cos\theta}{2\gamma \cos\theta - \rho g r h} - h \right) \tag{3}$$

Since the capillary rise height increases monotonically with respect to time, the viscosity of a polymer mixture at a specific curing time can be determined by dipping a capillary tube of radius r into the curing polymer (vertically, at the time of interest), measuring a capillary rise h over an additional (short) time t and then fitting Eq. (3) to find the target viscosity if all other characteristics ($\gamma \cos\theta$ and ρ) are known. To estimate $\gamma \cos\theta$ of PVS and PU, we used the limit that Eq. (2) reaches as the time approaches infinity (the system reaches steady state)

$$h = \frac{2\gamma \cos\theta}{\rho g r} \tag{4}$$

With Eq. (4) at hand, we measured the capillary rise height h of the base materials and curing agents separately, and then averaged the obtained $\gamma \cos \theta$ (Table 1) for the base material and curing agent of each polymer. Last, using Eq. (3) (see Figure 2-7 for illustration), we determined all required viscosities. Glass capillary tubes (CTechGlass, River Edge, NJ) with inner diameters of 0.3 and 1 mm were utilized to estimate the curing polymer viscosity as a function of time. All measurements were repeated 3 times.

Table 2-1 – Characteristics of base materials and curing agents of PVS and PU.

	ρ (kg m^{-3})	h (mm)	$\gamma \cos \theta$ (mN m^{-1})
PVS Green (base material)	1173	4.5	3.82
PVS White (curing agent)	1232	4.5	4.16
PU Part A (base material)	1022	40	35.74
PU Part B (curing agent)	1204	45	33.81

— r = 0.15 mm, 30 sec after mixing (η = 130 Pa·s)
-- r = 0.15 mm, 50 sec after mixing (η = 470 Pa·s)
···· r = 0.15 mm, 70 sec after mixing (η = 1360 Pa·s)
·-· r = 0.5 mm, 80 sec after mixing (η = 3630 Pa·s)
☆ Experimental data points
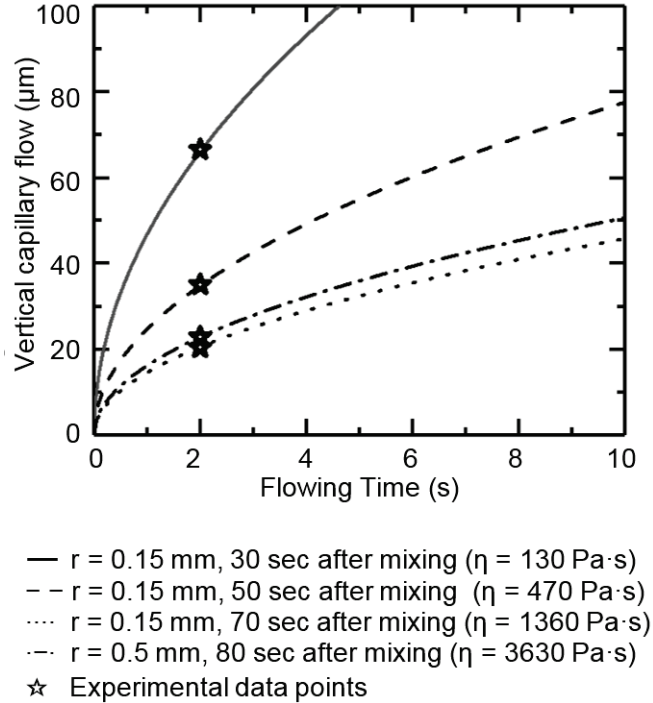
Figure 2-7 – Vertical capillary flow of PVS.

The results are presented in Figure 2-8a, where the viscosities of PVS and PU are shown within the time ranges of 30-80 s and 50-1320 s, respectively. These time ranges were set by the mixing time (25 s for PVS and 45 s for PU) on one hand and by the end of the working time (90 s for PVS and 1380 s for PU) on the other hand, while the working time was defined as the time, beyond which no capillary rise is observed. Obviously, PVS and PU showed different curing behavior, so, to analyze the data properly, we scaled the time and viscosity with respect to the working time and the viscosity measured at the end of the working time, respectively, as shown in Figure 2-8b.
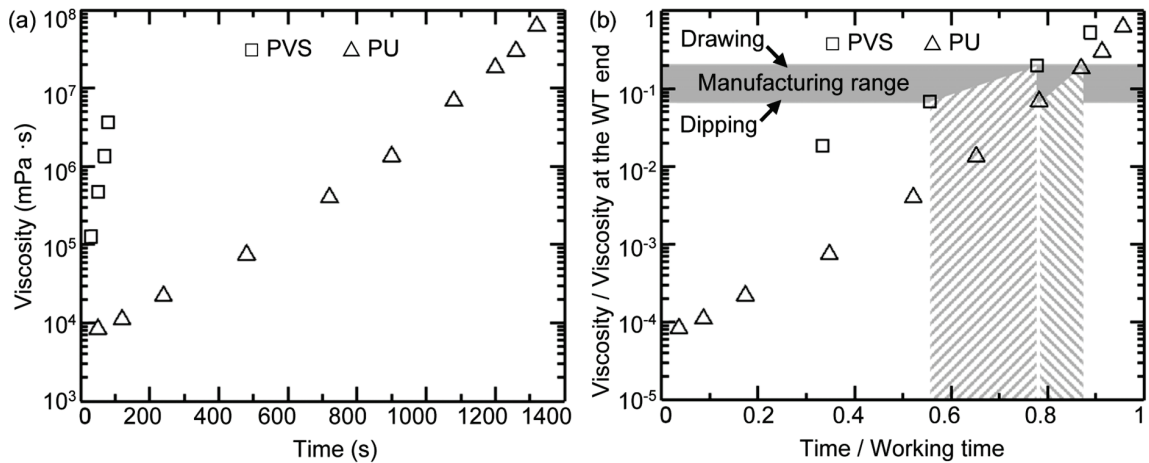
Figure 2-8 – Viscosity of curing PVS and PU with respect to time. (a) Original and (b) normalized data. Working times and viscosities at the end of working times for PVS and PU are 90 s and $6.910 \cdot 10^6$ mPa·s, and 1380 s and $1.007 \cdot 10^8$ mPa·s, respectively. Grey and hatched areas represent the manufacturing range for drawing high-aspect-ratio microstructures.

Experimenting with different drawing times, we found that the best flaps are obtained when the polymer viscosity is about 0.2 of the viscosity at the end of the working time (see Figure 2-8b). Drawing at larger viscosities leads to compromised surface quality

due to unrelaxed surface stresses and to a more pronounced limitation in the achievable flap height due to flap tearing from the backing layer. Drawing at smaller viscosities results in a lower flap height and thickness due to a gravity-driven sinking of the curing polymer and a higher capillary rise between drawing elements. Further, to provide the polymer with the time needed to adjust for the penetration of drawing elements, the polymer viscosity at the time of dipping was chosen to be about 0.07 of the viscosity at the end of the working time.

Having these two viscosity limits allowed us to define the dipping/drawing times for both PVS and PU, which were around 50/70 s and 1080/1200 s, respectively. It should be noted here that although curing times vary with temperature, this effect was negligible for the conditions we worked in. We can also suggest that the same approach may be used for finding operational regimes for other curing polymers once their time-dependent viscosity and working time are known.

2.3.3 Effect of Drawing Distance

Drawing distance defines the microstructure height parameters, of which the flap height is the most important. With the assumptions that (1) the capillary rise between drawing elements is negligible, (2) the flap thickness is negligible, and (3) the drawing array is large enough for the edge effects to be neglected as well, the ratio of the flap height to the drawing distance should be equal to 2 if the gap between the U-shaped drawing elements is equal to the drawing element width. This follows from the principle of volume conservation, while it is clear that working with V-shaped drawing elements leads to a

different slope. However, the flaps have certain small height due to wetting of the drawing element walls by the curing polymer even before drawing is initiated, and the flap thickness is obviously larger than zero, which makes the flaps a little higher than expected due to a volume conservation-driven adjustment.

Another source of deviation from the theoretical flap height of twice the drawing distance is related to a gravity-driven sinking of the curing polymer, as shown in Figure 2-9a. After the polymer is drawn up and left to cure, it sinks down as long as it is not completely cured. This leaves a thin-layer trace (down to a fraction of μm thick, based on the dip coating theory)[111] on the surface of the drawing elements. This trace is torn from the flap tip upon release of the drawing elements, which makes the flaps lower.

To predict the flap height, we have to correct for the torn part, which requires us to estimate its size. Figure 2-9b presents the estimated heights of the torn flap tips, which are obtained by subtracting the total microstructure height H_m from twice the dipping distance D_p measured in PVS and PU surfaces that were obtained by using thick U-shaped (KU) blade edges. Looking at these data, we can suggest that the size of the torn part initially increases linearly with increasing drawing distance, and then it levels off (differently for materials with different viscosity) to become independent of the drawing distance, as demonstrated by the dotted trend lines. Subtracting the estimated size of the torn flap tip (dotted line in Figure 2-9b) from the theoretical flap height (solid line in Figure 2-9c) provides us with the estimation of the flap height (broken line in Figure 2-9c). Notably, the measured flap heights, which are also shown in Figure 2-9c, are a little larger than the estimated values, which results from the volume conservation-driven adjustment

28
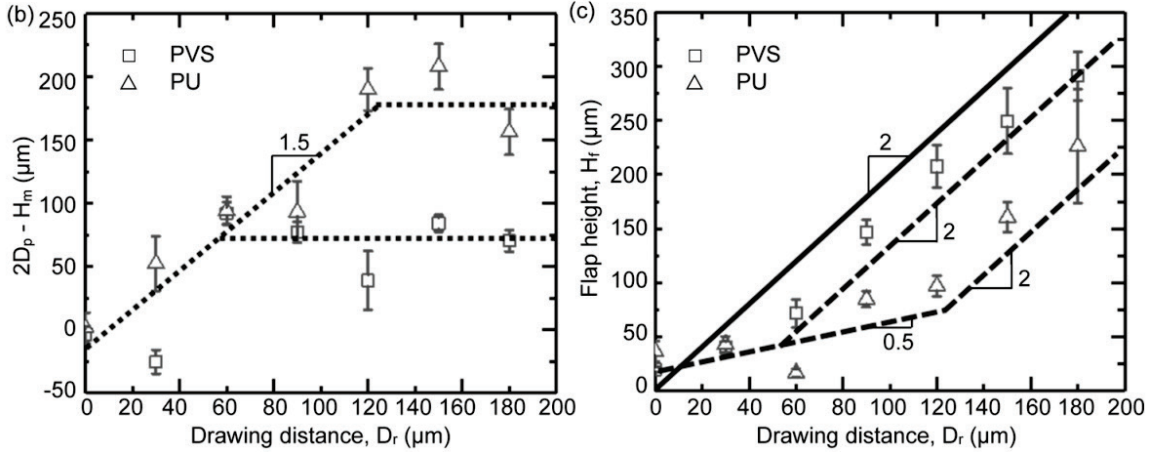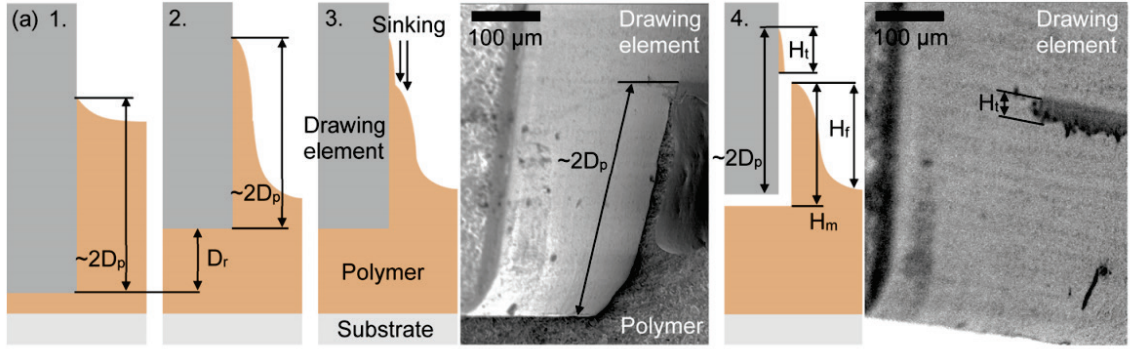
Figure 2-9 – Effect of drawing distance on flap height. (a) Close-up of a flap formation. 1. Drawing element is dipped into the curing polymer for a distance D_p. 2. Drawing element is drawn out of the curing polymer for a distance D_r. 3. Until the polymer is completely cured, it sinks downwards, forming a thin-layer trace on the surface of the drawing element. 4. During release of the drawing element, this thin-layer trace H_t is torn away from the flap tip. (b) Estimated torn flap height $H_t \approx 2D_p - H_m$ as a function of drawing distance D_r for PVS and PU structures made using thick U-shaped (KU) blade edges. H_m is the total microstructure height (see (a)4). Dotted lines represent data fit. (c) Flap height H_f (see (a)4) as a function of drawing distance D_r for PVS and PU structures made using thick U-shaped (KU) blade edges. Solid line represents theoretical flap heights. Broken lines represent theoretical flap heights corrected for the torn flap tip. Error bars represent standard deviation.

mentioned above. Thus, the flap height is found to be proportional to the drawing distance, with several other (less important) factors being responsible for shifting the actual values up or down.

2.3.4 Effect of Drawing Speed

Working with higher drawing speed results in larger viscous forces acting on the polymer solution as the drawing element is pulled out of it, leading to a larger thickness of the drawn layer. If the polymer flow is not constrained by interaction with other elements, the thickness of the drawn layer, h_0, is predicted by the dip coating theory [110, 111] as

$$h_0 = c \left(\frac{\eta U_0}{\rho g} \right)^{\frac{1}{2}}$$

(5)

where c is the constant, η is the viscosity of the polymer solution, U_0 is the speed of the drawing element, ρ is the density of the polymer solution and g is the gravitational acceleration. However, to fabricate wall-shaped adhesive microstructures, a densely packed drawing array is used, where the polymer flow can be affected by the presence of adjacent drawing elements after a certain threshold speed is exceeded, similar to confined dip coating [116, 117].

To see whether the relationship between the flap thickness (measured at a half of the flap height, see Figure 2-6) and the drawing speed agrees with Eq. (5), we studied the effect of drawing speed on the flap thickness with respect to the drawing array gap, as shown in Figure 2-10a. It is evident that when the drawing speed is low and the drawing

array gap is large, the relationship between the flap thickness and the drawing speed shows good agreement with Eq. (5), although the slope is slightly lower than 1/2. On the other hand, when the drawing speed is high and the drawing array gap is small, the flap thickness remains constant regardless of the drawing speed, which differs from the prediction made by the dip coating theory.

These effects are observed much better if both the flap thickness and the drawing speed are normalized by the drawing array gap, as shown in Figure 2-10b. Presented in this way, all data fall on a general curve having two distinct zones, one dominated by the drawing speed and the other dominated by the drawing array gap. In the first zone, viscous forces define the polymer behavior in accord with the dip coating theory. In the second zone, the effect of volume conservation plays the most important role because some minimum amount of the polymer solution is required to fill the gap formed between the substrate and the drawing array as the latter is withdrawn from the former, limiting the maximum achievable flap thickness. Obviously, the existence of this limit (0.1 of the drawing array gap) makes the process control easier.

Another interesting result seen in Figure 2-10b is that PVS and PU show good agreement despite large differences in their viscosities and working times. This can be attributed to a proper choice of the drawing time (see Section 2.3.2 for details), and it also suggests that the same approach may be used for working with other curing polymers.
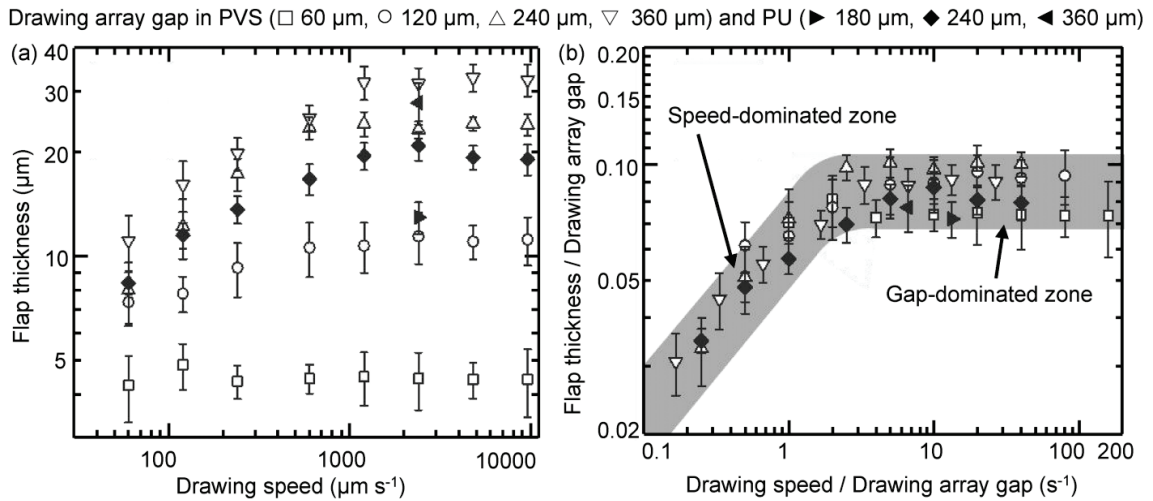
Figure 2-10 – Effects of drawing speed and drawing array gap on flap thickness for PVS and PU structures made using U-shaped blade edges: (a) data as measured, (b) normalized data. Slanted region represents the power of ½ relationship between thickness and speed, obtained according to the dip coating theory. Horizontal region corresponds to the sole effect of the drawing array gap, where speed changes make no difference. Error bars represent standard deviation.

2.3.5 Drawn Microstructures

By controlling the manufacturing parameters such as dipping and drawing distance and time, as well as the drawing array characteristics, we could fabricate various wall-shaped adhesive microstructures from PVS and PU as shown in Figure 2-11.
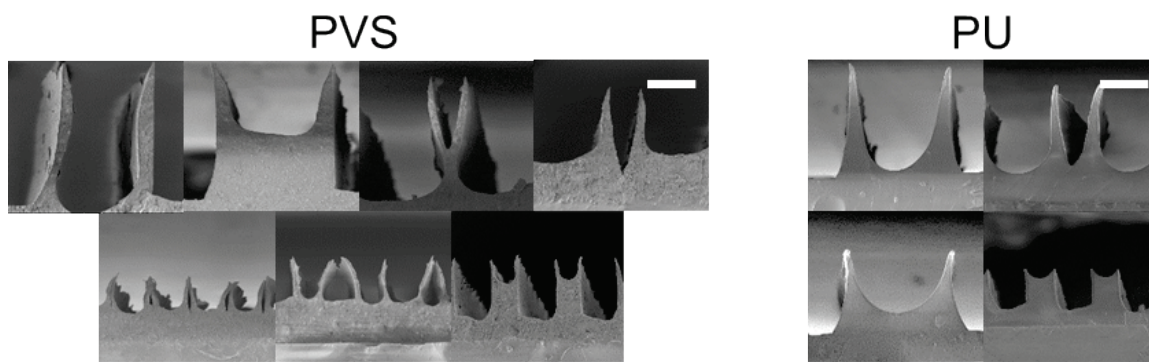
Figure 2-11 – Various wall-shaped adhesive microstructure made out of PVS and PU using the drawing. Scale bars: 100 μm.

2.4 Concluding Remarks

For the first time, drawing-based manufacturing has been successfully implemented to fabricate dry shear-activated adhesives, which is potentially able to revolutionize the field due to the high flexibility, cost-efficiency, simplicity and scalability of the method. The environmentally friendly fabrication process can be robustly controlled by such processing parameters as the tool speed, time and displacement during the dipping and drawing stages, making it suitable for mass production. Though being manufactured by a simpler technique, the drawn adhesive microstructures perform similarly to or better than those fabricated by the conventional molding, as will become clear from the following chapters. Based on this study, we may expect that the reported drawing technique will change the paradigm in manufacturing dry adhesives and will open new paths for their commercialization for industrial and domestic use.

CHAPTER 3.   LOADING CONDITIONS

In this chapter, the effects of two main loading parameters, pulling angle and preliminary tangential displacement, are covered. The pulling angles of 10-170º and preliminary displacements of 1-500 µm were used in order to find loading conditions at which the best adhesive performance of the wall-shaped microstructures is achieved. In addition, the effect of preload was also examined.

3.1   Experimental Details

3.1.1   Sample Preparation

Molded PVS samples of 140, 100, and 70 µm in height (Young's modulus of 3 MPa) and drawn PU samples of 250 µm in height (Young's modulus of 2 MPa) were fabricated to study the effect of loading conditions. The PVS samples were used to test the effect of preload on static friction as well as the effects of preliminary displacement and pulling angle on adhesive and frictional performance. The PU samples were used to test the effect of preload on the maximum pull-off force. Samples of 2 mm in diameter were cut out of the original structured polymer sheets using a disposable biopsy Uni-Punch (Premier Products, Plymouth Meeting, PA), so the wall-shaped projections had a total peeling line length of 22 mm in molded samples and 11 mm in drawn samples. Then the samples were cleansed with deionized water with soap and dried in blowing nitrogen. A glass slide of 30×5×1 mm in size having roughness average R_a of 5 nm was cleansed with ethanol, deionized water and blowing nitrogen and then used as a counterface. In testing

the effect of preload on static friction, epoxy substrates with various roughness were used (see chapter 4.1.1). Tested surfaces were inspected with an M125 optical stereomicroscope and imaged in a Quanta 250 environmental scanning electron microscope. The SEM was operated in a low-vacuum mode at 130 Pa and 5 kV to enable charge-free imaging of non-conductive samples in their natural state.

3.1.2 Testing Procedure

All tests were carried out in the custom-built tribometer [105] that was introduced in chapter 2.1.1. The tribometer was operated inside a Quanta 250 environmental scanning electron microscope in order to allow visualization of the studied surfaces while measuring contact forces. The SEM was run in a low-vacuum mode at 130 Pa and 5 kV. Some samples, however, to be imaged in the SEM, were coated with a 5-nm-thick-layer of Au/Pd using the Desk V sputter (Denton Vacuum, Moorestown, NJ, USA) operated for 180 seconds at 18 mA current and about 5×10^{-2} Pa Ar pressure.

In order to measure the peeling performance of the wall-shaped adhesive microstructures under various loading conditions, after mounting a structured sample on the tribometer in such a way that the wall-shaped projections were perpendicular to the sliding/pulling direction, the sequence shown in Figure 3-1 was run while recording the generated normal ($F_\perp$) and tangential ($F_\parallel$) forces.
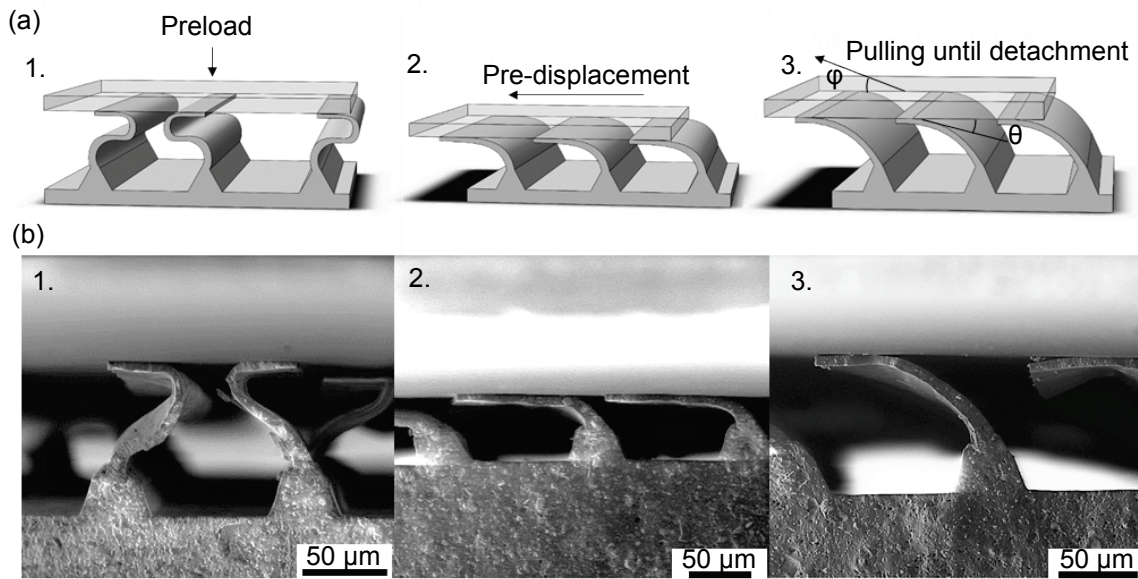
Figure 3-1 – Schematic (a) and SEM images (b) of the test sequence. 1. Preload is applied. 2. Pre-displacement is applied while maintaining the same preload. 3. The glass slide is pulled at a certain pulling angle, φ, while the peeling angle, θ, adjusts itself according to the contact conditions.

First, the counterface was moved in perpendicular to the contact plane until a designated normal load was achieved. Then, the counterface was moved in parallel to the contact plane under the same normal load and at a speed of 100 μm s⁻¹ for a designated preliminary distance that was changed between 0 and 500 μm. Next, the counterface was withdrawn from the contact at the speed of 100 μm s⁻¹ and at a designated pulling angle φ (Figure 3-1). The test stopped at a complete detachment of the counterface from the structured sample. This sequence was used to measure the pull-off force in a shear-activated mode. Eliminating the stage of tangential preliminary displacement allowed to

36

measure the pull-off force in a deactivated mode. The temperature and relative humidity in the laboratory were 25-27 °C and 45-55 %, respectively. All tests were repeated at least four times.

3.2 Results and Discussion

3.2.1 Effect of Pre-Load
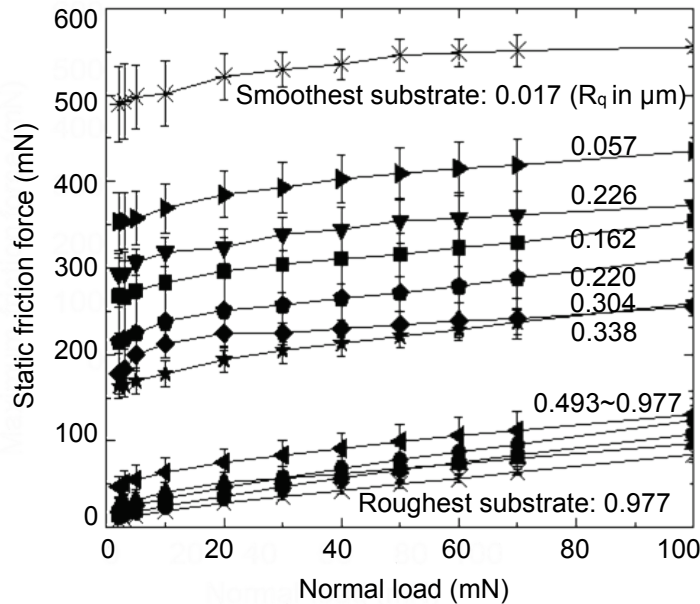
Figure 3-2 – Mean static friction force measured with original wall-shaped microstructures as a function of normal load on counter surfaces with different topography. Error bars represent standard deviation.

The friction force measured at the point of sliding inception on epoxy substrates with various roughness is presented in Figure 3-2 as a function of the normal load. Similar to previous results [33] obtained on a smooth counterface, we see extremely high friction

starting from the very low normal loads (less than one hundredth of the measured friction), and it grows with increase in the load. In line with the performance of thin-film-covered surface architectures [118], deterioration of the surface finish results in the friction curves shifting towards lower values, while the effect of load is preserved. Obviously, this is explained by changes in the real contact area, which decreases with increasing roughness and increases with increasing load.
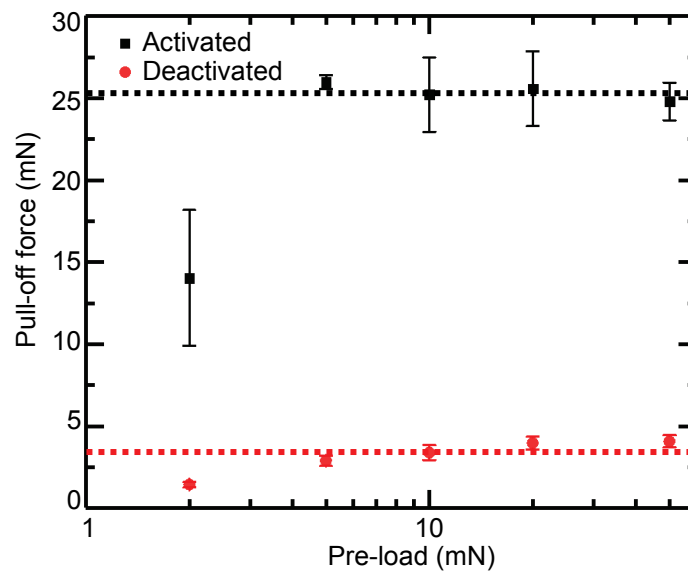
Figure 3-3 – Mean activated and deactivated pull-off force measured at preliminary displacement of 300 μm and pulling angle of 90º with PU microstructures as a function of pre-load against smooth glass substrates. Dashed lines represent the mean values calculated from 5, 10, 20, and 50 mN pre-load cases. Error bars represent standard deviation.

In contrast to the static friction results shown in Figure 3-2, it is clearly seen in Figure 3-3 that pre-load does not affect the adhesive performance in both shear-activated

and deactivated modes unless the pull-off force is smaller than a certain threshold pre-load (5 mN for the PU microstructured sample). It is postulated that the pull-off force is constant because the peeling process is independent of the real contact area while being dependent on the total peeling line length. As a higher pre-load does not increase the total peeling line length, it is clear that the pre-load should not affect the attachment performance. However, lower pull-off force values were observed at 2 mN pre-load. This is possibly attributed to the fact that there can be a small misalignment between the structured sample and the substrate that shows at small loads only. Thus, we can conclude that the pre-load does not affect the attachment performance if it is high enough to bring all surface projections into contact with the substrate.

3.2.2   Effect of Preliminary Displacement

Several examples of normal ($F_\perp$) and tangential ($F_\parallel$) forces recorded during the tests are shown in Figures 3.4 and 3.5 as a function of tangential displacement. The topmost grey and black curves represent normal and tangential force envelopes obtained during a simple sliding test, in which the normal force is kept constant, and the tangential force increases until the inception of sliding and then levels off after a small decrease, in a fashion similar to the behavior of real gecko foot hairs [7]. A sudden drop in the tangential contact stiffness at the initial stage of the sliding test corresponds to the overturning of those wall-shaped projections that initially buckled in the non-preferred direction (Figure 3-1). A decrease in the tangential force after the sliding inception point corresponds to the start of the stick-slip motion of the individual projections, which move asynchronously, leading to

a uniform global sliding characterized by average (between static and kinetic) friction [119].

The curves that split from the normal and tangential force envelopes in Figure 3-4 correspond to the forces measured during the withdrawal stage after three characteristic preliminary displacements. The normal force curves look similar in all three cases, with initial change from compression due to pre-load to tension due to adhesion, then reaching maximum at the pull-off point, and eventually dropping to zero after the detachment process starts. The tangential force curves have different appearances depending on the preliminary displacement, which allows identification of several modes of contact behavior.
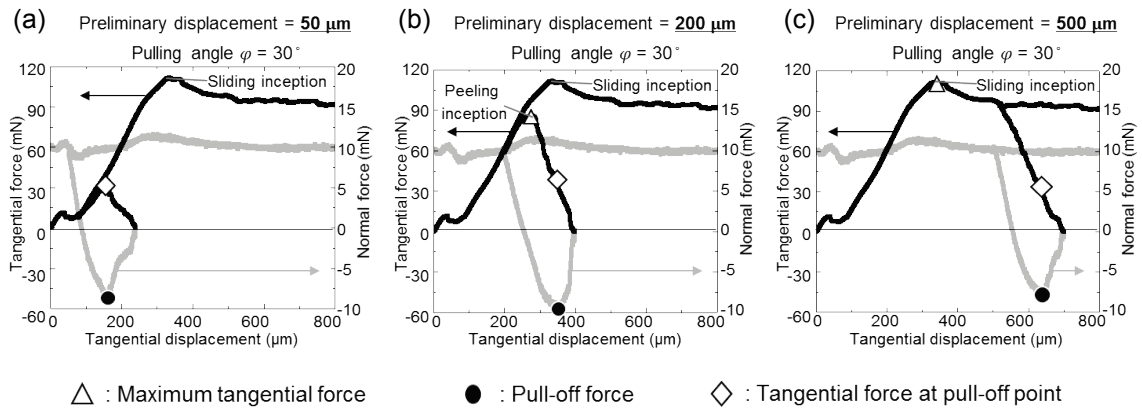
Figure 3-4 – Characteristic examples of normal (in grey) and tangential (in black) forces recorded during the tests. (a), (b), (c) Preliminary displacement, *d*, of 50, 200, 500 μm, pulling angle, φ, of 30º.

If withdrawal starts at small preliminary displacement when the wall-shaped projections are not yet aligned and stretched (Figure 3-4a), the additional tangential

40

displacement during withdrawal results in more stretching of the projections and a corresponding increase in the tangential force. The tangential force grows until the pull-off point, at which the wall-shaped projections start detaching, resulting in the force decreasing to zero at the point of complete detachment. In this case, some of the surface projections are peeled at very high angles because they are not yet overturned, so their contributions to the total pull-off force are small and the structured surface does not perform at its best.

At intermediate preliminary displacement when the projections are already aligned but are not yet stretched to their maximum ability (Figure 3-4b), the additional tangential displacement during withdrawal also results in more stretching and a corresponding increase in the tangential force. However, since the peeling angle θ (Figure 3-1) increases constantly as a result of the flap stretching, the wall-shaped projections start to peel off the counterface before the inception of sliding. While in the peeling mode of operation, the wall-shaped projections seem to obey the prediction of the Kendall model [55], so the tangential force decreases with increasing tensile normal force until the pull-off point, at which the projections start to detach. In this case, the microstructured surface performs at its best and a maximum attachment ability can be expected.

If withdrawal starts after sliding inception (Figure 3-4c), the wall-shaped projections are stretched non-uniformly due to their asynchronous stick-slip motion. To this end, they start peeling and pulling off at much more widely distributed tangential displacements. This non-uniformity results in a smaller total pull-off force, leading to a non-optimal overall performance of the microstructured surface.

3.2.3   Effect of Pulling Angle

After the structured sample was preloaded and a designated preliminary displacement was applied, the glass slide was withdrawn at a designated pulling angle that was changed between 10° and 170° at intervals of 10°. At low pulling angles (Figure 3-5a), the microstructured surface starts sliding after a critical tangential displacement is reached, and the stick-slip disturbances undermine the adhesive performance of the wall-shaped projections. At high pulling angles (Figure 3-5c), the direction of tangential motion is inverted, and the wall-shaped projections are actually unloaded, which also results in a non-optimal performance. At intermediate pulling angles (Figure 3-5b), the wall-shaped projections perform at their best, as they are properly loaded, and no detrimental side effects come into force.
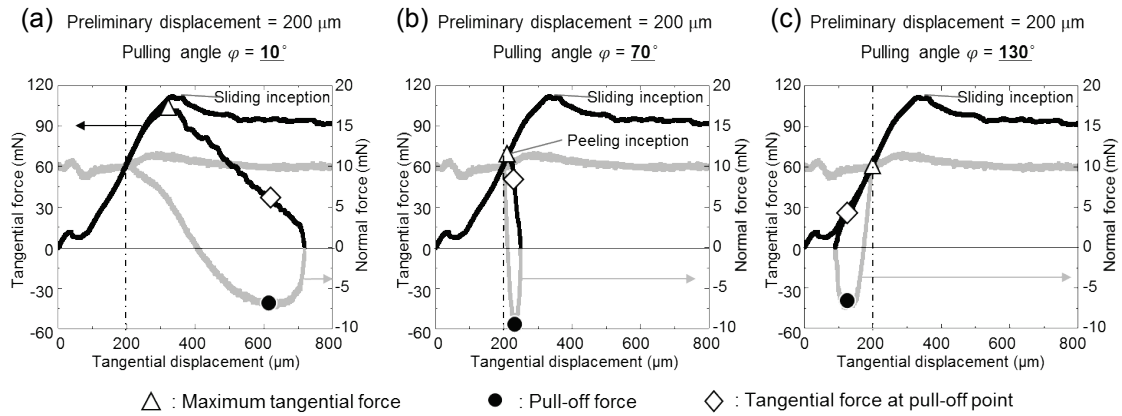
Figure 3-5 – Characteristic examples of normal (in grey) and tangential (in black) forces recorded during the tests. (a), (b), (c) Preliminary displacement, *d*, of 200 μm, pulling angle, φ, of 10°, 70°, 130°.

The curves shown in Figures 3-4 and 3-5 represent the raw data, from which we extracted several characteristic force values for each combination of the preliminary

42

displacement and the pulling (withdrawal) angle, and for all three types (heights) of the tested surfaces. These force values are the maximum tangential force and the maximum tensile normal (pull-off) force that the microstructured surfaces could generate during each experiment. To analyze the maximum load carrying capacity, we have also determined the tangential force that corresponds to the pull-off point. The results are discussed below.

The maximum tangential ($F_\parallel$) force values obtained in different test conditions for three types of the microstructured surfaces are shown in Figure 3-6. As explained above, there are two competing processes that allow for stress relaxation when the surface is loaded – sliding and peeling. When sliding starts first, which happens with smaller preliminary displacements at low pulling angles, and with larger preliminary displacements at high pulling angles, the maximum tangential force is defined by static friction. In this case, the higher the flaps, the larger the real contact area and, hence, the friction. When peeling starts first, which happens with smaller preliminary displacements and higher pulling angles, the maximum tangential force depends on how close the contact is to the verge of the sliding inception. In this case, increasing the preliminary displacement results in increasing the maximum tangential force, and increasing the pulling angle leads to decreasing the maximum tangential force. At pulling angles of more than 90º, as expected, the maximum tangential force depends only on the preliminary displacement. This is because the direction of the tangential motion is inverted in relation to the preliminary displacement, and the microstructured surface is actually unloaded in this direction during withdrawing. Hence, the tangential force decreases with respect to the force generated at the completion of the preliminary displacement.
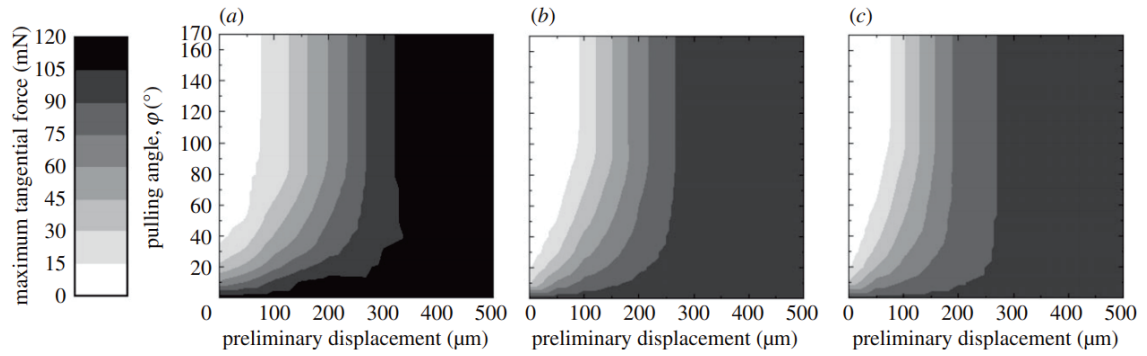
Figure 3-6 – Maximum tangential ($F_\parallel$) force obtained under different combinations of preliminary displacements and pulling angle. (a) High flaps. (b) Medium flaps. (c) Low flaps.

Figure 3-7 presents the normal ($F_\perp$) and tangential ($F_\parallel$) forces obtained at the pull-off point under different combinations of preliminary displacements, pulling angle and flap height. In line with what is expected based on Figures 3-4 and 3-5, the normal (pull-off) force (Figure 3-7a,b,c) demonstrates optimum values at the regime of about half the preliminary displacement needed to start sliding.
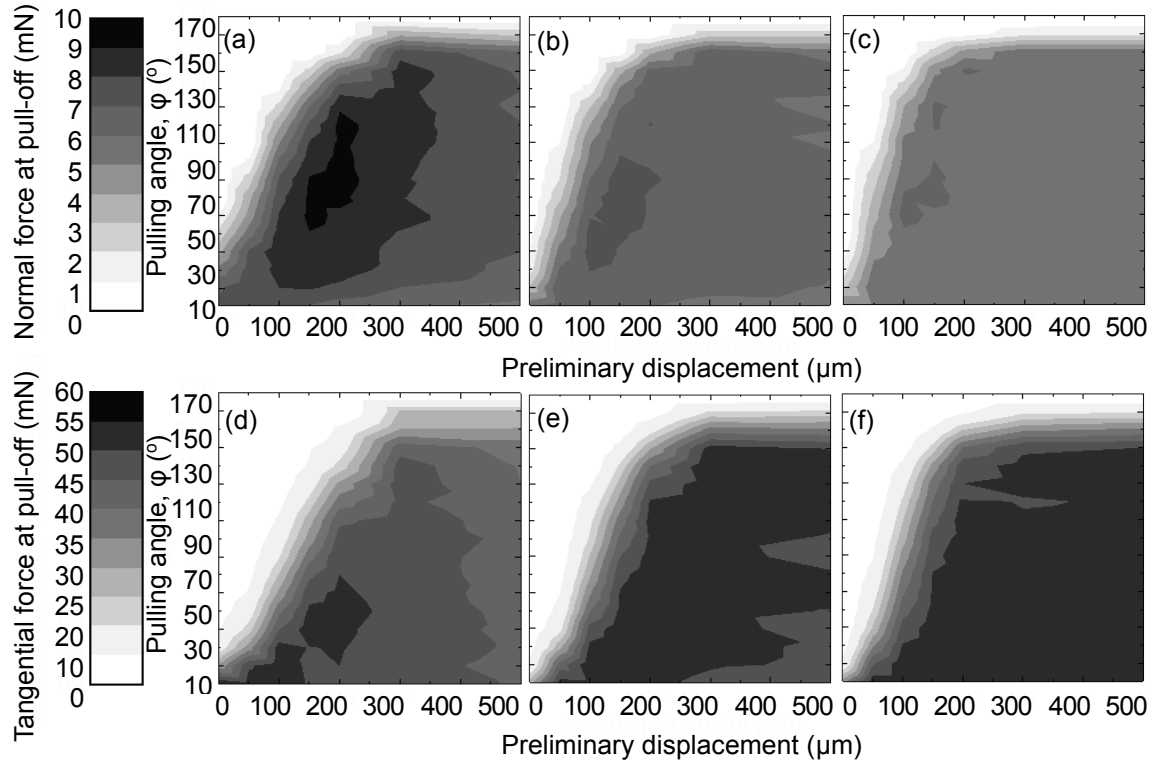
Figure 3-7 – Normal ($F_\perp$) and tangential ($F_\parallel$) forces obtained at the pull-off point under different combinations of preliminary displacements and pulling angle. (a), (d) High flaps. (b), (e) Medium flaps. (c), (f) Low flaps.

At smaller preliminary displacement, the wall-shaped projections are not yet properly aligned after establishing initial contact and random buckling (Figure 3-1). At larger preliminary displacement, the inception of sliding prevents the wall-shaped projections from acting optimally due to a non-uniform tangential load associated with the stick-slip motion.

The withdrawal angles that determine the optimum pull-off force vary within 60º-90º, which initially seems to be inconsistent with the previous works, which give a narrow range of optimum peeling angles (e.g. [102, 120]). However, this apparent contradiction is

resolved if we recall that the withdrawal (pulling) angle does not necessarily correspond to the peeling angle (Figure 3-1). This is because the direction of displacement (input in our case) does not correspond to the direction of force (output in our case) when a slender structure is loaded not in the plane of symmetry.

Assuming that the peeling angle should comply with the direction of the peeling force, we can refer to the tangential force map shown in Figure 3-7d,e,f. It becomes evident that the region of the optimum normal force coincides well with the contour lines of the tangential force, which gives a constant ratio of the normal over tangential force and results in similar peeling angles for the whole optimum range. This corresponds to the behavior of real gecko foot hairs, which are known to detach at a narrow range of angles [7, 102]. It is worth noting that the wide range of the optimum pulling angles reflects a robustness of the wall-shaped microstructure that can tolerate relatively large inaccuracies in loading direction when in the attachment state and can still detach at zero force when the pulling angles reach 140°-160°. This ability to switch between adhesive and non-adhesive states is similar to the performance of real gecko foot hairs [7, 102, 121], although the critical attachment/detachment angles are different due to differences in the geometries of our artificial attachment structure and the gecko's natural attachment structures.

The difference in the optimum performance of the wall-shaped projections of different heights is not very significant in either the normal and tangential forces, the preliminary displacement, or the pulling angles, although all parameters tend to decrease with decreasing height. This can be explained by the fact that shorter flaps both align and start sliding at smaller preliminary displacement, which moves the window of optimum

performance towards the origin, which is characterized by lower forces, displacements and angles.

The effects of the preliminary displacement and the pulling angles can also be observed in several characteristic examples of the real contact area and the microstructure profiles demonstrated in Figure 3-8 at different stages of the experiment. When the preload is applied, the wall-shaped projections buckle randomly, resulting in the folded flaps forming a uniform but small contact area (Figure 3-8a). Shearing the contact leads to all flaps unfolding and aligning to form a much larger contact area (Figure 3-8b) able to carry higher tangential and normal forces. When the tangential displacement is sufficiently large to initiate sliding, stick-slip instabilities lead to random (in time and space) motion of the flaps, so the contact area becomes small and uneven, and as a result the surface cannot support high loads. Such behavior takes place when the glass counterface is withdrawn at low pulling angles (Figure 3-8c). If, however, the pulling angle is sufficiently large to not allow the system to reach the sliding inception (Figure 3-8d), the wall-shaped projections peel uniformly and steadily, resulting in the best possible adhesive performance.
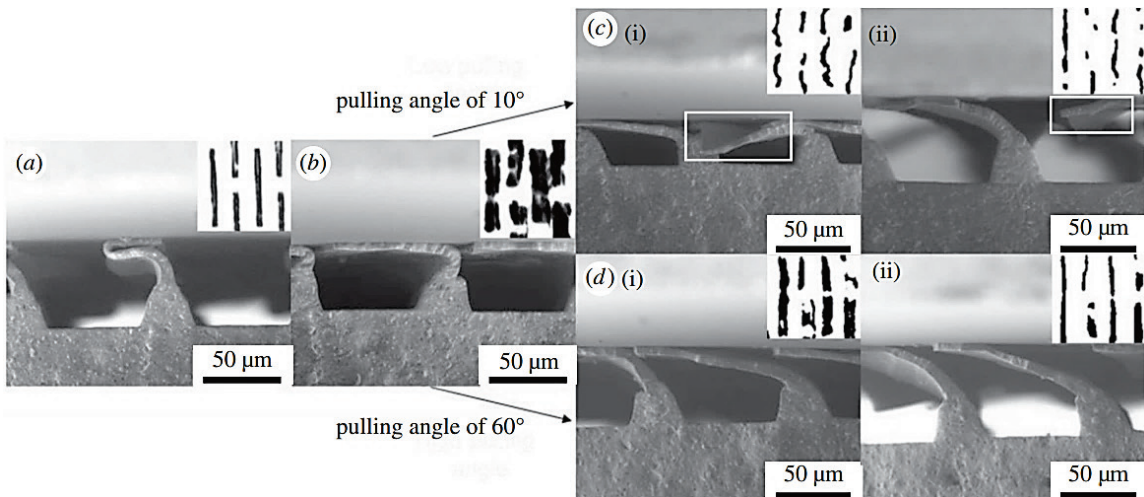
Figure 3-8 – Characteristic examples of the real contact area (insets) and the microstructure profiles obtained at different stages of the experiment. (a) Preload is applied. (b) Preliminary displacement of 150 μm is applied. (c) Glass slide is pulled at angle of 10°. (d) Glass slide is pulled at angle of 60°. White rectangles highlight the regions of detachment formed due to stick-slip motion.

It is also interesting to note that when the point of the pull-off instability is eventually reached, the contact area (peeling line length times contact width, w) appears to be very similar for the wall-shaped projections of all three heights (Figure 3-9). To this end, since this area is obviously adjacent to the flap edge, the active film is thinner in the higher flaps due to some gradient in thickness, as shown in Figure 2-5. According to the Kendall model, this should result in a higher pull-off force, which is indeed observed for the higher wall-shaped projections tested in our experiments.
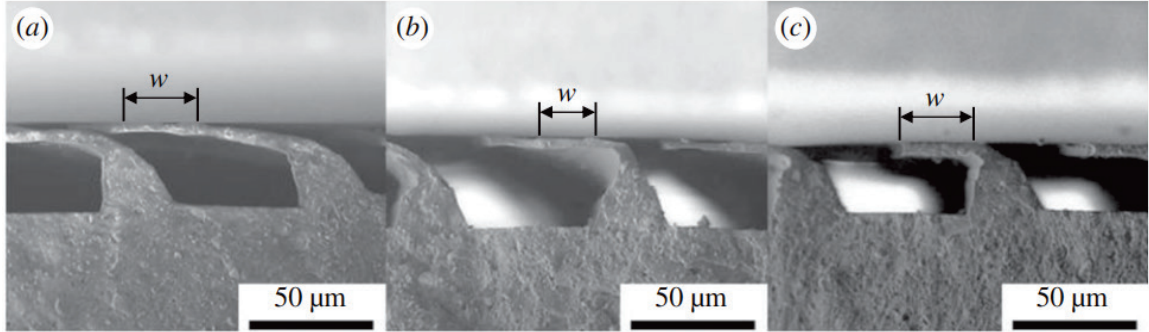
Figure 3-9 – Wall-shaped microstructures with (a) high flaps, (b) medium flaps, and (c) low flaps imaged close to the pull-off instability at preliminary displacement of 150 μm and pulling angle of 60º.

3.2.4   Comparison with Existing Models

Having at hand the data presented in Figure 3-10, we were also interested to see whether these data are better described using the Kendall model of thin-film peeling [55], or by using the Autumn model stipulating the constant ratio of the normal over the tangential force as an attachment limit [102]. To represent our data correctly, we used only the data subsets corresponding to the optimum preliminary displacements, so neither the initial not-aligned state, nor the final stick-slip-affected state of the wall-shaped projections were taken into account. The results are shown in Figure 3-10, where all force values are measured, and the peeling angles are calculated as $\theta = A \cdot \tan^{-1}\frac{F_\perp}{F_\parallel} + B$, where A = 3, 4.5, 4.5 and B = 15, 23, 17 are the coefficients of the high, medium and low flaps, respectively, adjusted for a better match with the Kendall model.
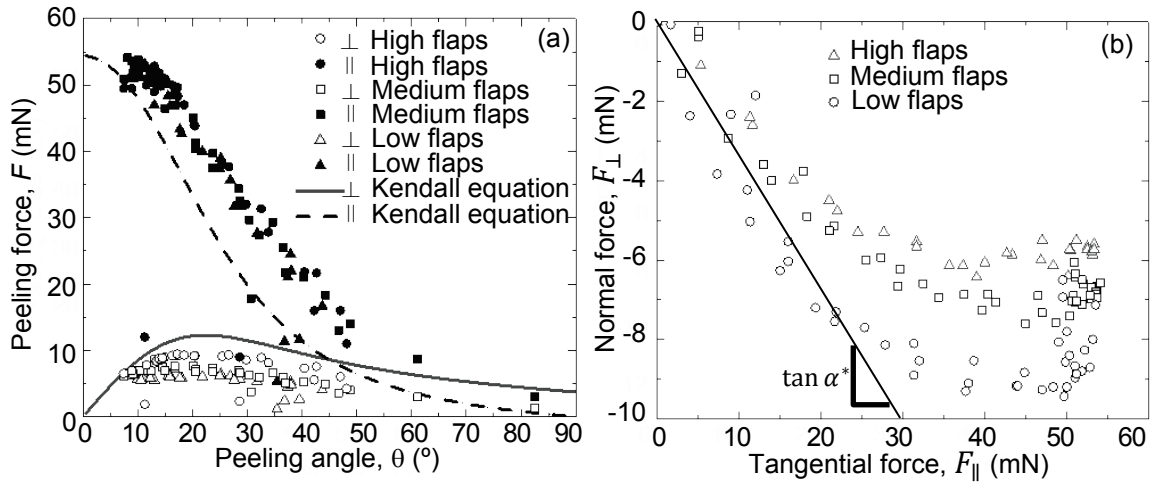
Figure 3-10 – Normal (F⊥) and tangential (F∥) forces obtained at the pull-off point at optimal preliminary displacements (150, 200 μm for high flaps; 100, 150, 200 μm for medium flaps; 100, 150 μm for low flaps) and all pulling angles. (a) Represented according to the Kendall model [55]. (b) Represented according to the Autumn model [102].

The theoretical normal and tangential components of the model's peeling force were computed based on the Kendall equation [55]

$$\left(\frac{F}{b}\right)^2 \frac{1}{2dE} + \frac{F}{b}(1 - \cos\theta) - R = 0, \tag{6}$$

where F is the total peeling force, b = 22 mm is the total peeling line length, d = 6 μm is the average flap thickness, E = 3 MPa is the elastic modulus of the PVS, θ is the peeling angle and R = 0.17 N m⁻¹ is the fracture energy per unit area chosen to fit the experimental data. This equation has only one positive solution for the total peeling force, and this solution was used to calculate its normal and tangential components. The line representing the Autumn model has been drawn based on the best visual fit of the linear portion of the

data and has a slope $\tan \alpha^* = 0.33$, which corresponds to a detachment angle α^* of 18°. It is evident that the Kendall approach yields a better fit, while the observed deviations can be associated with the presence of triangular bases and a non-uniform thickness of flaps in the wall-shaped projections.

Interestingly, a similar non-linear relationship between the normal and tangential forces (Figure 3-10b) is also observed with wedge-shaped gecko-inspired attachment structures [32, 102], which throws doubt on the applicability of the Autumn model [102] to current artificial systems. The observed discrepancy may be related to a large difference between the high elastic modulus of the keratinous setae used to devise the Autumn model and the low elastic moduli of the silicon-based elastomers employed in current bio-inspired adhesives. This explanation is consistent with Kendall's analysis [55], which can represent the Autumn model as a particular "no extension" case of a more general solution.

3.3   Concluding Remarks

Testing the wall-shaped adhesive microstructures of three different heights at several preliminary tangential displacements and pulling angles allowed us to draw the following conclusions. In accordance with the prediction of the Kendall model for the normal component of peeling force (Figure 3-10a), there is an optimal normal force that is required to detach the wall-shaped adhesive microstructure. The optimum is obtained at about half the distance needed to initiate sliding, as at smaller preliminary displacement the contact flaps are not properly aligned, while at larger preliminary displacements the stick-slip instabilities undermine the uniformity of the load. In terms of the pulling direction, the optimum is obtained within the range of 60–90°, which points to the difference between

pulling and peeling angles and suggests that the wall-shaped microstructure can tolerate relatively large inaccuracies in the loading direction. The increase in the attachment force with increasing flap height is found to be weak but measurable and is thought to correlate with the flap thickness, which decreased with increasing flap height.

The study of pre-load showed that the adhesive performance of wall-shaped microstructures does not depend on this parameter unless it is too low to generate good alignment between the structures and counterface or too high to avoid damage. The static friction force grows with increasing pre-load while much higher friction values are obtained against smoother surfaces as a result from the associated increase in the real contact area.

CHAPTER 4.   SURFACE CONDITIONS

Given that the objects to be gripped may be different, it is essential to examine our adhesive systematically against various surfaces to find out how surface conditions affect its attachment performance. To this end, in this chapter, we cover the effects of counterface topography and surface chemistry.

4.1   Experimental Details

4.1.1   Sample Preparation

To study the effect of topography, microstructured surfaces with 140-μm-high flaps (Figure 4-1a,b) were molded from PVS against a laser micro-machined grid using the procedure described above [122]. Rectangular samples of $2.5 \times 5 \times 1$ mm in size were cut out of the mold, so the wall-shaped projections on each sample had a total peeling line length [15] of about 76 mm.

Counterface samples (Figure 4-1c-h) of $20 \times 5 \times 1$ mm in size were prepared from Spurr Epoxy resin EM0300 (Sigma-Aldrich, St. Louis, MO, USA) by replicating topography of twelve different surfaces using two-step molding method [123] and then cutting the samples to size. The surface topography was examined using a 3D optical profiler ContourGT-I. To obtain data on a large area without sacrificing resolution, all surface profiles were stitched from 24 regions of 1000×64 μm scanned at a magnification $\times 100$ with a lateral resolution of about 0.1 μm.

To study the effect of surface chemistry, adhesive microstructures were drawn from curing F-150 REV1 Polyurethane (PU; BJB Enterprises, Tustin, CA) using laboratory razor blades (Pacific Handy Cutter, Costa Mesa, CA) of 229 μm in thickness, which faced the polymer with their blunt edges. The blades were assembled into an array of 2.5 mm in width, with the inter-blade gaps of about 240 μm formed by 4 sheets of the tape Scotch Magic 810 (3M, Maplewood, MN). First, the curing polymer was smeared onto a glass slide (at 720 s after mixing) using a razor blade and spacers to have a uniform thickness of about 300 μm. Second, the drawing array was dipped into the curing polymer to a distance of 180 μm at 1080 s after mixing and then withdrawn to a distance of 150 μm at 1110 s after mixing, with a contact angle measurement system OCA 25 being used for the fabrication process. After 2 hours, when the drawn microstructures were fully cured, the drawing array and the microstructured PU sample were disassembled together from the drawing setup and placed into a water-filled M1800H ultrasonic bath for an hour before the sample was released.

7525M Glass (7525M Plain Microscope Slides, J. Melvin Freed, Perkasie, PA), Sylgard 184 PDMS (Dow Corning, Midland, MI), Epoxy (Sigma-Aldrich, St. Louis, MO), Alumina (Al_2O_3), 6061Al, SUS304, PTFE, Acrylic, Titanium, PVC, PP (McMaster-Carr, Elmhurst, IL), 2950 Glass (2950-001 Plain Microscope Slides, Thermo Fisher Scientific, Waltham, MA), Tempered Glass (OtterBox Alpha Glass Tempered Glass Screen Protector, OtterBox, Fort Collins, CO), and PU were used as counterface materials. A polishing machine Unipol-802 with different types of sandpapers (Struers, Cleveland, OH) was utilized to polish all samples to have a desired roughness average R_a of less than 50 nm. Sandpapers were also used to roughen some of the surfaces. Contact angles were measured

with droplets of 2 µl using the sessile drop technique in a contact angle measurement system OCA 25. Surface roughness was measured using a 3D optical profiler ContourGT-I, with the area of 230.8 µm × 173.1 µm scanned with a lateral sampling of about 0.36 µm. All measurements were conducted at 5 different locations.

All samples were cleansed with soap, deionized water and blowing nitrogen before use, and they were inspected with an M125 optical stereomicroscope. The SEM operated in a low-vacuum mode at 120 Pa and 10 kV to enable charge-free imaging of non-conductive PVS samples in their natural state. The Epoxy samples, however, to be imaged in the SEM, were coated with Au/Pd using the Desk V sputter for 180 seconds at 18 mA current and about 5×10^{-2} Pa due to their high tendency to charge. All tests were repeated at least 4 times.

4.1.2   Testing Procedure

The tests for the effects of surface roughness were carried out in the custom-built tribometer, [105] able to measure pull-off and friction forces inside the SEM. Microstructured samples were mounted on the tribometer such that the wall-shaped projections were oriented in perpendicular to the sliding/pulling direction and the following test sequence was run to measure the pull-off force. First, a counterface sample was moved in perpendicular to the contact plane until the normal load of 20 mN was achieved. Then, the sample was moved in parallel to the contact plane under the same normal load using a speed of 100 µm/s for the preliminary displacement of 300 µm needed for the flap alignment [122]. Next, the counterface sample was withdrawn from the contact at the speed

of 100 μm/s at the pulling angle of 90º until it detached from the structured sample, and the detachment (pull-off) force was measured. The maximum friction force was measured at the instant of sliding inception, while the counterface sample was slid against the microstructured sample under the constant normal load of 20 mN.

To test the effect of surface chemistry, samples of 2 mm in diameter were cut out of the microstructured sample using a disposable biopsy Uni-Punch. The samples were cleansed with deionized water, dried in blowing Nitrogen and then fixed in place using a carbon tape (Nisshin EM Corporation, Tokyo, Japan). Counterface substrates had the size of 10×5×1 mm. After fixing the samples such that the microstructure projections were perpendicular to the sliding/pulling direction, the load-drag-pull tests were run while recording generated normal and tangential forces. First, the counterface sample was moved in perpendicular to the contact plane until a normal load of 10 mN was achieved. Then, the counterface was moved in parallel to the contact plane under the same normal load at a speed of 100 $\mu m\ s^{-1}$ for a designated preliminary distance (chosen to maximize the pull-off force). Next, the counterface was withdrawn from the contact at the speed of 100 $\mu m\ s^{-1}$ at the pulling angle of 90º. The test stopped at a complete detachment of the substrate from the structured sample. Each combination was tested 5 times. The temperature and relative humidity in the laboratory were 23-25 ºC and 45-50 %, respectively.

4.2   Results and Discussion

4.2.1   Effect of Topography

The effect of surface topography on the attachment performance of the wall-shaped adhesive microstructure was studied using several carefully prepared counter surfaces under the preload of 20 mN, preliminary displacement of 300 μm and pulling angle of 90°. The pull-off forces measured against different rough surfaces (Table 4-1, Figure 4-1c-h) are shown in Figure 4-2. The surfaces are represented using the traditional root-mean-square deviation of the primary (P_q) and roughness (R_q) profiles, and using the new adhesion-oriented integrative characteristic of the primary (P_i) and roughness (R_i) profiles [67] developed recently to take into account the spatial information of contact asperities based on the Greenwood-Williamson approach [124]. It is clear that the more contact points and the larger asperity radius the surface has, the larger the adhesion will be. On the other hand, adhesion will decrease as the distribution of asperity heights increases. Thus, the integrative roughness parameter can better represent the correlation between roughness and adhesion, as was shown on the example of mushroom-shaped adhesive microstructures in a previous study [67]. Hence, both the root-mean-square roughness parameters (P_q, R_q) and the new integrative roughness parameters (P_i, R_i) were calculated and compared. The surface density of asperities ζ, the mean radius of asperity summits β, and the standard deviation of asperity height distribution σ_s needed for calculation of the new integrative characteristic P_i, $R_i = \sigma_s/\beta\zeta$ were obtained by analyzing asperity peaks identified in a 3D surface profile with a deterministic method based on 8 nearest neighboring points [125]. The P_q, R_q, P_i, and R_i values are summarized in Table 4-1.

Table 4-1 – Mean surface profile characteristics obtained at five different locations on Epoxy replicas of different objects.

	Table desktop #1	12 μm FibrMet disc	3 μm FibrMet disc	1 μm FibrMet disc	0.3 μm FibrMet disc	Print paper	Refri-gerator	Wood block	Table desktop #2	Sputter coater	P150 abrasive paper	Glass slide
P_q (μm)	3.288	4.207	2.239	0.981	0.478	4.004	0.215	8.161	7.545	4.043	17.628	0.220
P_i (μm²)	2.344	3.417	3.505	1.282	0.580	5.696	0.036	7.726	9.072	4.744	49.033	0.025
R_q (μm)	0.162	0.493	0.600	0.304	0.226	0.581	0.057	0.977	0.338	0.220	0.867	0.017
R_i (μm²)	0.135	0.608	1.085	0.389	0.266	0.818	0.011	1.188	0.318	0.214	4.720	0.002
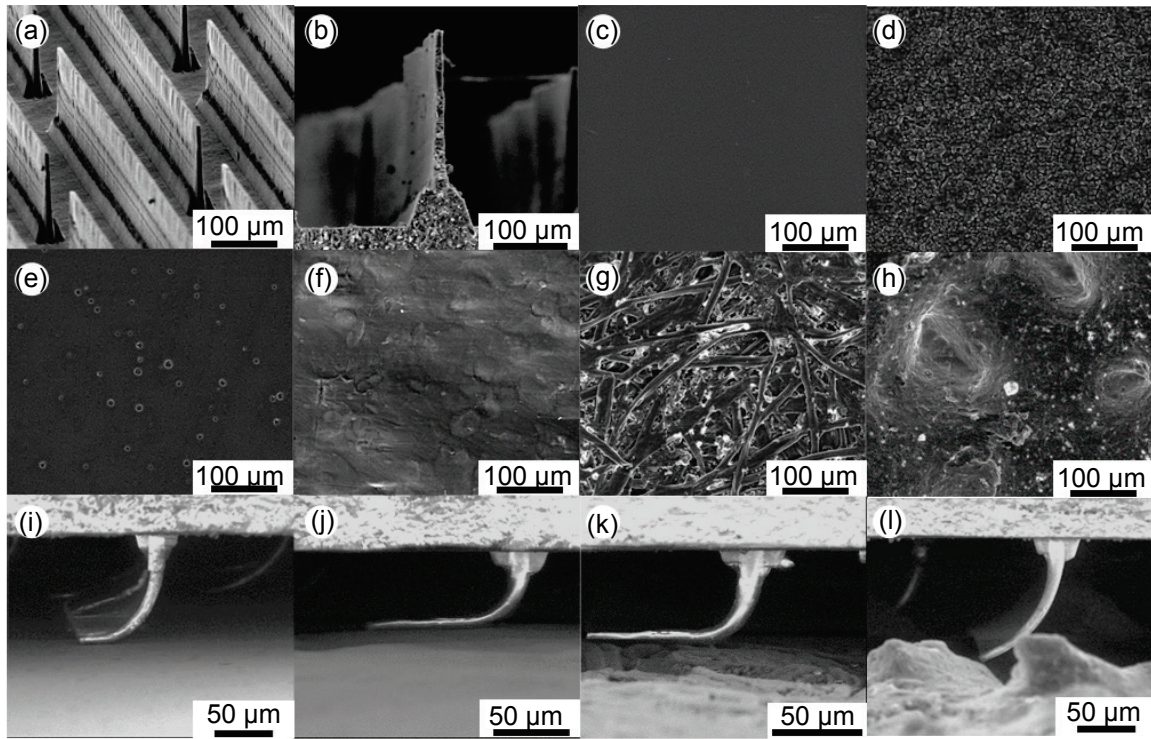
Figure 4-1 – Characteristic images of tested polyvinylsiloxane (PVS) adhesive microstructures in (a) as-cast original and (b) the cross-sectional view, the Epoxy replicas of (c) glass slide, (d) 3 μm FibrMet disc, (e) refrigerator, (f) table desktop, (g) print paper, and (h) P150 abrasive paper used as counter-face surfaces, and the wall-shaped microstructures in contact with the surfaces replicating the topography of (i) refrigerator, (j) table desktop #1, (k) print paper, and (l) P150 abrasive paper.
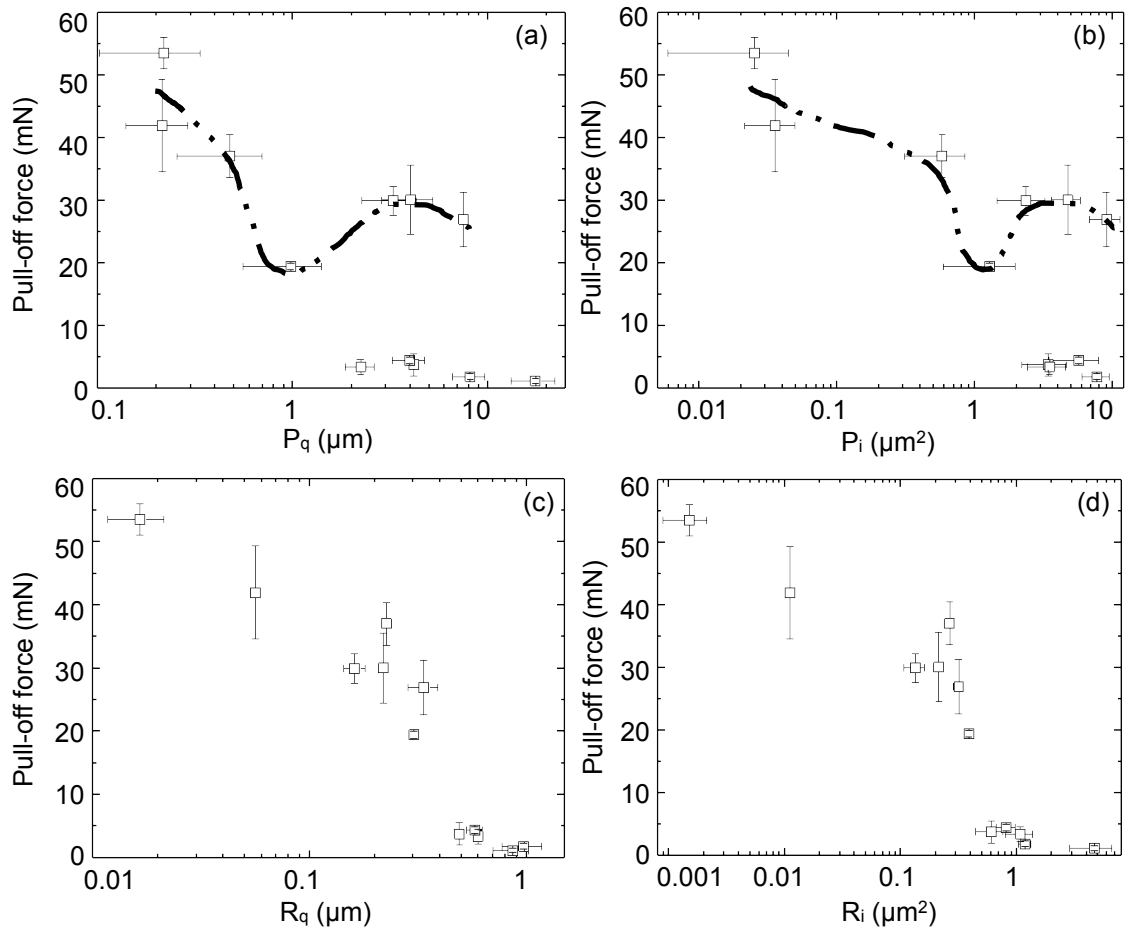
Figure 4-2 – Pull-off force measured after preload of 20 mN on different rough surfaces and represented as a function of (a) P_q and (b) P_i calculated based on primary (unprocessed) counterface profiles, and (c) R_q and (d) R_i calculated based on roughness profiles obtained after Gaussian high-pass filtering with the cut-off wavelength of 10 μm. Open marker represents mean value measured with original microstructure. Error bars represent standard deviation. Dotted lines represent hand-drawn fits of the highest pull-off force values measured with the original microstructure over the whole range of profiles.

Studying the relationship between the pull-off force and either the height (Figure 4-2a) or the hybrid height-spacing (Figure 4-2b) parameters of the primary (as measured)

profiles (root-mean-square deviation (P_q) and new integrative characteristic ($P_i = \sigma_s/\beta\eta$), respectively, Table 4-1), we do not see much correlation. This is because the measured primary profile characteristics are dominated by the low-frequency, long-wavelength components, aka waviness, and the high-frequency, short-wavelength components, aka roughness, do not contribute much. To this end, wavy and smooth profiles may have approximately the same geometric characteristics as wavy and rough profiles, while their adhesive properties may differ greatly. This effect is evident in Figure 4-2a,b, where several surfaces having similar profile characteristics demonstrate very different pull-off forces. The lack of correlation between waviness-dominated characteristics and adhesion suggests that filtering the waviness out may result in a better correlation between the adhesive and geometrical properties of the studied counter surfaces.

Looking at the highest pull-off forces measured over the whole range of profiles in Figure 4-2a,b, we can recognize the curves (dotted lines) associated with the idea of "critical roughness", which was used to explain the drop in the animal's ability to attach to certain surfaces [59, 126, 127]. However, in light of the discussed lack of correlation between adhesion and waviness, and given that among the studied substrates we employed those used in [126, 127], it may also be instructional to see how filtering out the waviness would reflect on the critical roughness.

The important question is how to find the division between roughness and waviness. Because the definition of the critical point at which roughness becomes waviness depends on the application, we have to account for the system's performance with respect to its characteristic size. Given that the adhesive performance is determined by the system's ability to form a large contact area while storing little elastic energy, we can define the

above critical point as the point at which the adhesive flap bending needed for adaptation to surface irregularities becomes too energy-consuming. To this end, the bending stiffness of the adhesive flaps is the decisive property and, hence, the flap thickness is the most important characteristic size. Assuming that flaps of 5 μm in thickness are not able to adapt to surface irregularities having a wavelength of less than 10 μm, we used this latter value as a cut-off length to filter out the waviness information from the primary profiles with the Gaussian high pass filter [128].

The pull-off force, represented as a function of the parameters calculated based on the filtered roughness profiles, is shown in Figure 4c,d (root-mean-square deviation (R_q) and new integrative characteristic ($R_i = \sigma_s/\beta\zeta$), respectively, Table 4-1). In line with the performance of thin-film-covered surface architectures [118, 129], we can now see a clear negative correlation between the pull-off force and the roughness, with the integrative roughness R_i having better resolving power (4 vs. 2 orders of magnitude in range) and higher Spearman's rank correlation coefficient (-0.97 vs. -0.95) than the root-mean-square roughness R_q. This correlation supports our analysis of the relationships between adhesion, roughness and waviness, and it proves that the adhesive performance of the wall-shaped microstructure depends on the micro-scale roughness of the counterface, most likely because it can adapt to a wavy but not to a rough surface. This finding implies that the profile measurements have to be properly conditioned to represent the adhesion data correctly.

It is also evident that, after filtering the waviness out, the idea of "critical roughness" does not work anymore, as we do not see a single most problematic roughness. Instead, the adhesive performance gradually degrades with increasing roughness, showing a range of roughness values that can be termed anti-adhesive for the studied adhesive microstructures.
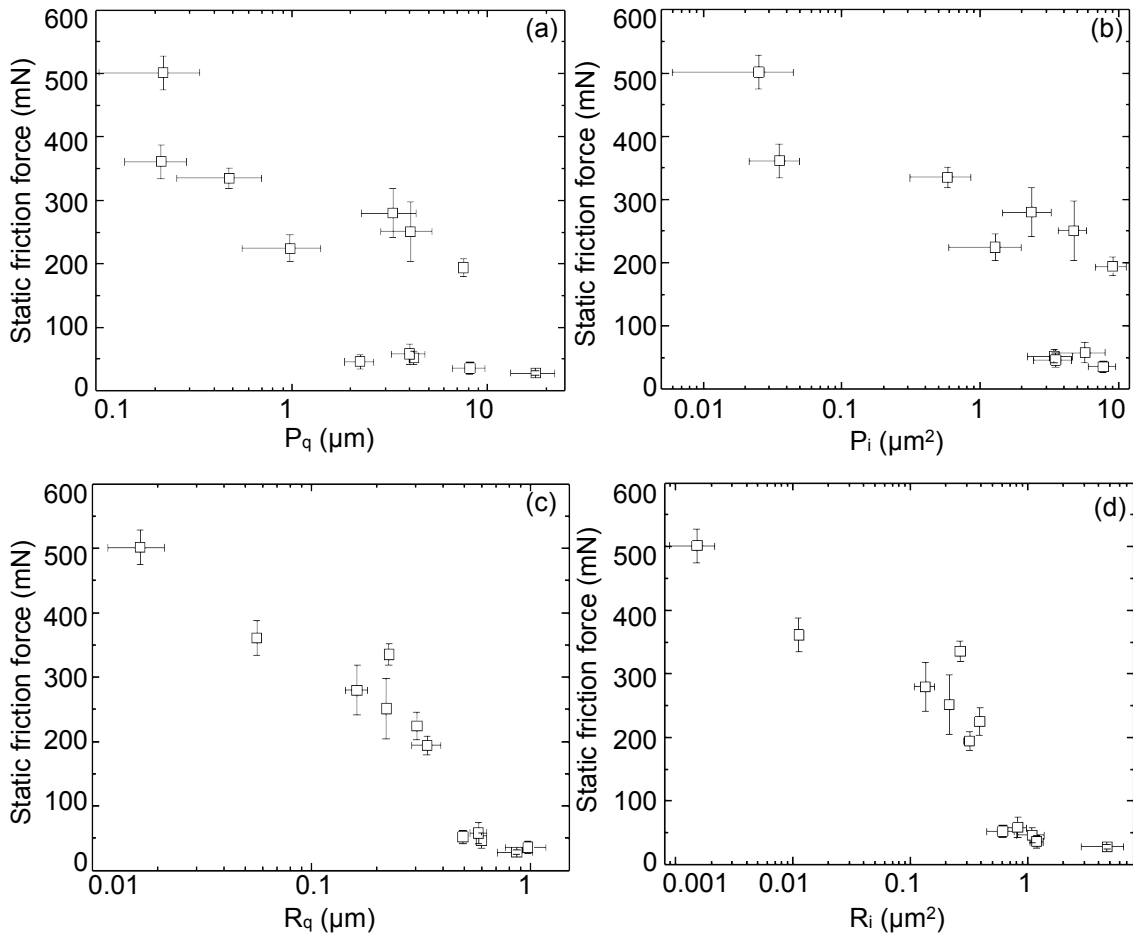
Figure 4-3 – Static friction force measured under normal load of 20 mN on different rough surfaces and represented as a function of (a) P_q and (b) P_i calculated based on primary (unprocessed) counterface profiles, and (c) R_q and (d) R_i calculated based on roughness profiles obtained after Gaussian high-pass filtering with the cut-off wavelength of 10 µm. Open marker represents mean value measured with original microstructure. Error bars represent standard deviation.

Representing the friction data as a function of parameters characterizing surface topography yields the results shown in Figure 4-3. Here, in line with the data on pull-off force, we see that changes in friction correlate well with the changes in surface roughness, whereas having the data on waviness included in the analysis undermines the clarity of this effect.

4.2.2   Effect of Surface Chemistry

The shear-activated dry adhesive drawn from PU [107] and examined in this study is shown in Figure 4-4. To test the effect of counterface chemistry on the attachment ability of this adhesive while excluding the effect of surface roughness, which can otherwise be very significant [130], we prepared samples having the roughness average (R_a) of less than 50 nm from 14 different materials. The surface free energy of these counterface samples was determined by the sessile drop method based on the Owens-Wendt model [131], with water, glycerol and dodecane being used as test liquids. The results are presented in Figure 4-5 and in Table 4-2.
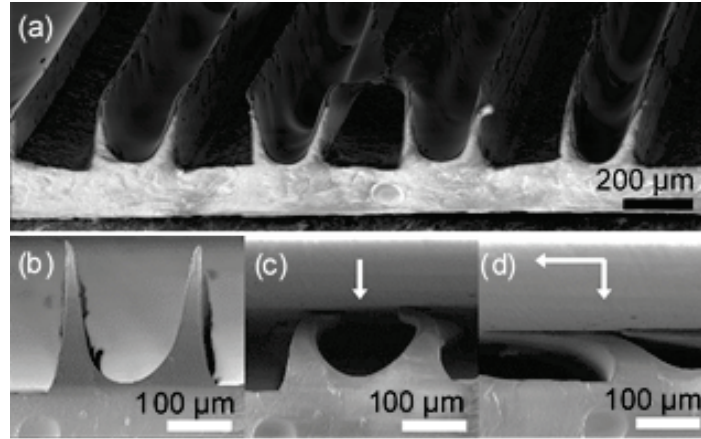
Figure 4-4 – (a, b) Scanning electron microscopy images of the PU wall-shaped adhesive microstructure. (c, d) Images of the microstructure loaded in normal and tangential directions. Arrows in the direction of loading.
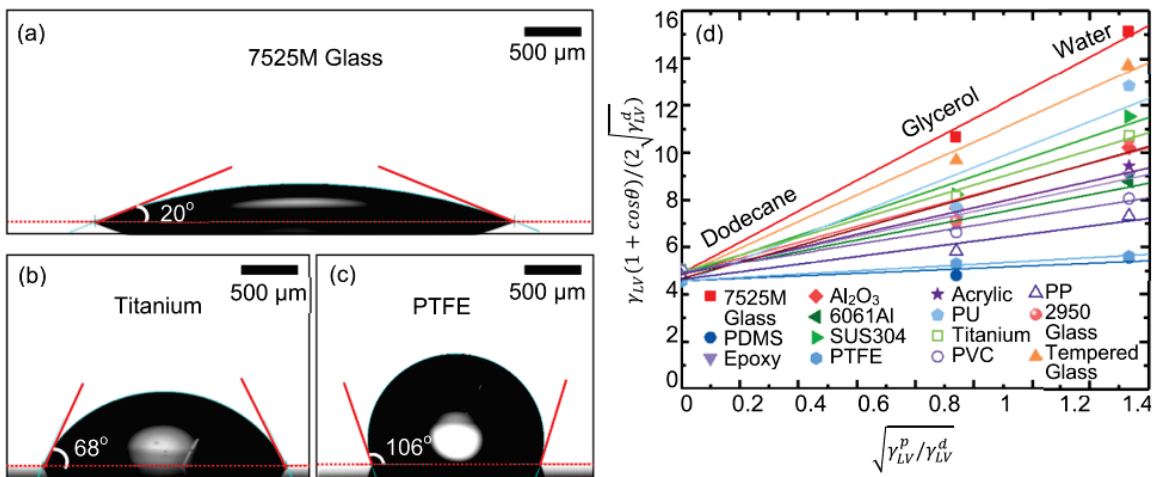
Figure 4-5 – (a-c) Water contact angle, θ_w, obtained on 7525M Glass, Titanium, and PTFE substrates. (d) Surface free energy of the studied substrates calculated based on the Owens-Wendt method. γ_{LV}^{d} and γ_{LV}^{p} are the dispersive and polar components of the surface free energy of the test liquids (γ_{LV}). The lines represent linear fits, with their y-intercept and slope being the square roots of dispersive ($\sqrt{\gamma^d}$) and polar ($\sqrt{\gamma^p}$) components of the substrate surface free energy, respectively.

64

Table 4-2 – Counterface materials, their roughness average (R_a), the contact angles (C.A.) of water, glycerol and dodecane obtained on their surfaces, and the dispersive (γ^d) and polar (γ^p) components of their surface free energy ($\gamma = \gamma^d + \gamma^p$) calculated using the Owens-Wendt method.

Substrate		R_a (nm)	Water C.A. (°)	Glycerol C.A. (°)	Dodecane C.A. (°)	γ^d (mN/m)	γ^p (mN/m)	γ (mN/m)
Metals	6061Al	31.2 ± 5.8	82.7 ± 4.6	77.0 ± 1.6	7.8 ± 2.7	23.6 ± 1.3	5.8 ± 0.6	29.4 ± 1.5
	SUS304	21.2 ± 2.9	61.4 ± 1.8	60.1 ± 2.1	0	23.4 ± 1.2	17.4 ± 1.0	40.7 ± 1.6
	Titanium	35.2 ± 1.8	67.8 ± 3.4	60.8 ± 1.4	0	24.4 ± 0.9	13.6 ± 0.7	38.0 ± 1.1
Polymers	PDMS	20.2 ± 1.7	106.7 ± 1.5	97.2 ± 0.6	31.0 ± 2.3	20.9 ± 0.6	0.3 ± 0.1	21.2 ± 0.6
	Epoxy	11.2 ± 2.6	81.0 ± 2.3	72.3 ± 1.4	13.5 ± 1.6	23.9 ± 0.7	6.9 ± 0.4	30.8 ± 0.8
	PTFE	34.6 ± 2.9	106.3 ± 4.0	92.0 ± 6.1	36.1 ± 3.1	20.9 ± 1.2	0.5 ± 0.2	21.4 ± 1.2
	Acrylic	5.8 ± 0.9	77.8 ± 3.1	73.5 ± 4.4	5.2 ± 2.5	23.5 ± 1.4	8.0 ± 0.8	31.5 ± 1.6
	PU	30.4 ± 7.3	49.8 ± 4.0	66.4 ± 2.2	7.9 ± 2.5	20.0 ± 2.8	24.0 ± 3.0	44.0 ± 4.1
	PVC	41.2 ± 2.6	88.1 ± 5.7	78.1 ± 2.5	7.7 ± 0.4	24.5 ± 1.4	3.9 ± 0.5	28.3 ± 1.5
	PP	40.1 ± 11.0	93.6 ± 0.8	86.5 ± 2.7	27.0 ± 2.1	21.4 ± 0.8	2.6 ± 0.3	24.1 ± 0.9
Ceramics	Al_2O_3	41.7 ± 1.5	72.0 ± 2.1	66.8 ± 5.1	8.0 ± 2.1	23.7 ± 1.2	11.2 ± 0.8	34.9 ± 1.4
	7525M Glass	5.6 ± 0.7	19.5 ± 3.0	18.6 ± 1.5	0	24.0 ± 0.8	42.9 ± 1.0	66.9 ± 1.3
	2950 Glass	6.6 ± 1.7	69.2 ± 3.8	73.1 ± 6.5	9.0 ± 1.6	21.8 ± 2.2	12.3 ± 1.6	34.0 ± 2.7
	Tempered Glass	5.0 ± 0.3	40.5 ± 2.2	40.3 ± 2.4	10.0 ± 2.0	23.3 ± 1.0	31.8 ± 1.2	55.1 ± 1.6

Analyzing the data shown in Figure 4-5d, from which the surface free energy values presented in Table 4-2 were calculated [132], we see that the y-intercept values of the linear fits (square root of the dispersive part of the surface free energy values, $\sqrt{\gamma^d}$) [132] are very similar. This result was also observed in other surface free energy studies [133, 134],

and it suggests that the polar component of the surface free energy is dominant in defining the differences between the surface free energy values of different substrates. To this end, one can estimate which substrate has higher surface free energy by simply checking the contact angles of some highly polar liquid, such as water, which can be readily obtained and is environmentally friendly. However, several test liquids should be used to determine the surface free energy values accurately.

Based on the above, the attachment ability of our PU-based shear-activated adhesive was studied as a function of the work of adhesion and, alternatively, as a function of the water contact angle, the most accurate and the most primitive descriptors of adhesive interaction, respectively. In doing so, the work of adhesion, W_a, between the shear-activated adhesive and each of the 14 substrates was calculated [131] as

$$W_a = 2\left(\sqrt{\gamma_{PU}^d \gamma_S^d} + \sqrt{\gamma_{PU}^p \gamma_S^p}\right) \tag{7}$$

where γ_{PU}^d and γ_S^d are the dispersive, and γ_{PU}^p and γ_S^p are the polar components of the surface free energy of PU and the substrates.

The measured pull-off and static friction forces are shown in Figure 4-6. It is obvious, that these characteristics are affected by the counterface chemistry, be it represented by either the work of adhesion or the water contact angle. Interestingly, both types of representation look very similar, which suggests that the use of the simplistic approach based on the water contact angle only can also yield valuable data. This is explained by the fact that, to a first approximation, the only parameter that varies in Eq. (7) is γ_S^p, and, as explained above, it can be conveniently represented by the water contact angle.
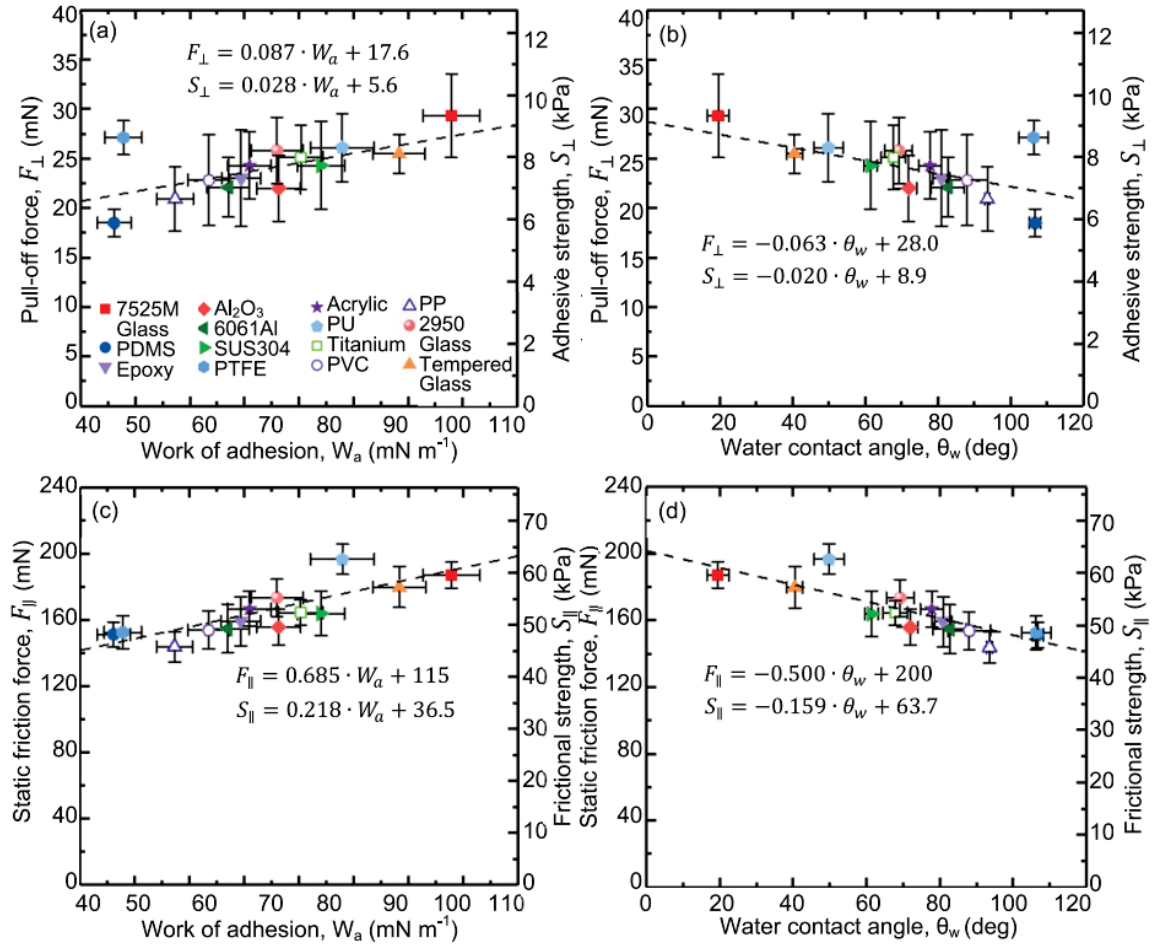
Figure 4-6 – (a, b) Pull-off force/adhesive strength and (c, d) static friction force/frictional strength obtained with the shear-activated adhesive on various substrates and shown as a function of the work of adhesion, W_a, and the water contact angle, θ_w. Dashed lines represent linear fits, and error bars represent standard deviation.

The maximum (for PU) over minimum (for PP) static friction force ratio representing the effect of counterface chemistry on friction is equal to about 1.4 (including anti-adhesive PTFE, see Figure 4-6). Interestingly, the effect of counterface chemistry on static friction obtained for geckos is equal to about 16.5 (on PMMA vs. PTFE) [79]. This

suggests that the PU-based artificial adhesive discussed here is about one order of magnitude less sensitive to the counterface chemistry than the β-keratin-based biological adhesive evolved in geckos. Thus, PU has high potential as a material of choice for versatile shear-activated adhesives.

It was also instructional to examine the combined effect of surface chemistry and roughness on both the pull-off and static friction forces measured with our bio-inspired adhesive. To do so, we took the 7525M Glass, Tempered Glass, SUS304, Epoxy, and PP samples utilized for gathering the data shown in Figure 4-6, and gradually roughened them with different sandpapers while measuring their adhesive and frictional responses using the same shear-activated adhesive. The results are presented in Figure 4-7 as a function of the water contact angle.
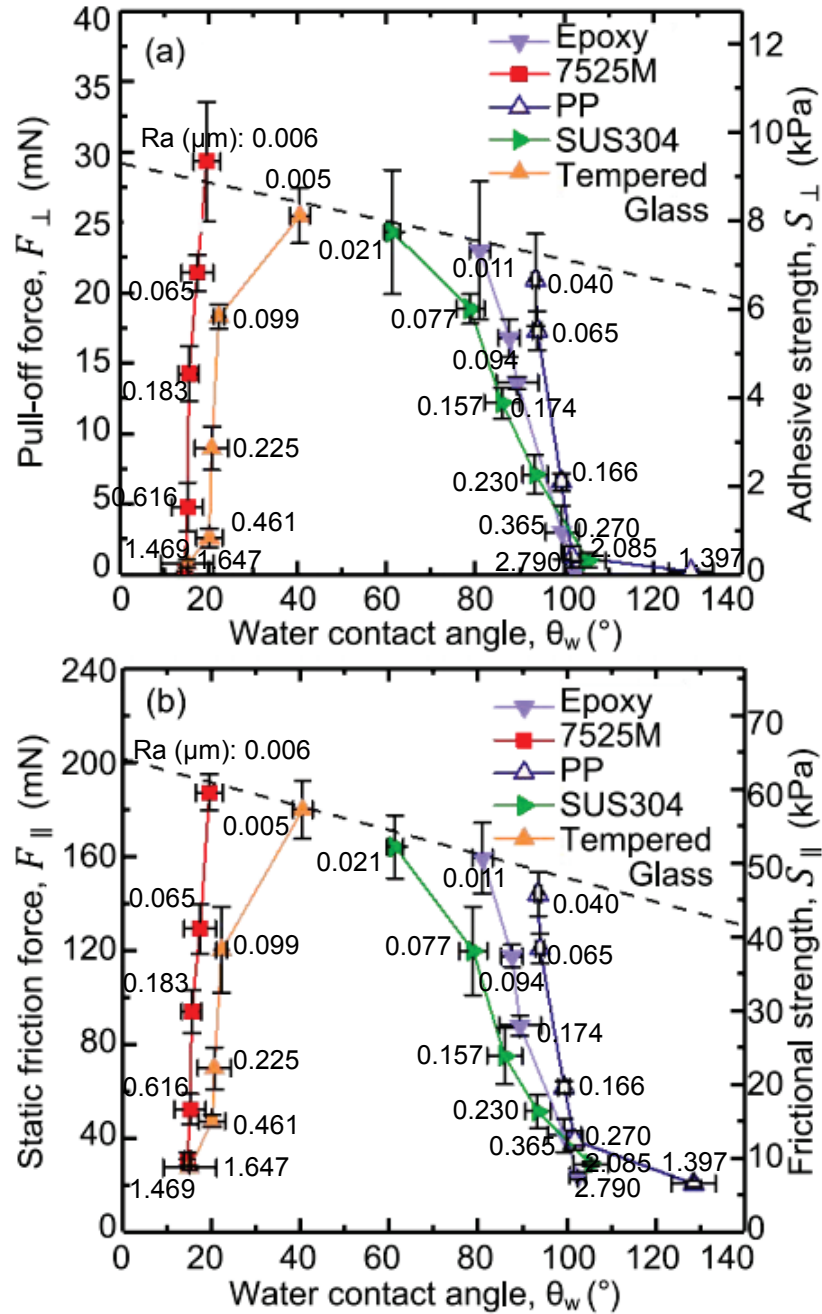
Figure 4-7 – (a) Pull-off force/adhesive strength and (b) static friction force/frictional strength obtained with the shear-activated adhesive on several gradually roughened substrates and shown as a function of the water contact angle. Dashed lines represent the linear fits from Figure 4-6, solid lines represent changes in material properties due to roughness variation and error bars represent standard deviation.

First, as can be easily seen, surface roughening of SUS304, Epoxy, and PP made them more hydrophobic, while surface roughening of 7525M Glass and Tempered Glass made them more hydrophilic. This is consistent with the Wenzel model describing the homogenous wetting regime and suggesting that the water contact angle either increases or decreases with increasing surface roughness, depending on the hydrophilicity of the substrate [135]. However, in contrast to the Wenzel model, the point at which the effect of roughening is inverted is located not at the contact angle of 90°, but somewhere between 40° and 60°. This shift can be explained by the heterogenous wetting regime established due to entrapment of air inside the sharp-ended scratches formed by abrasive material removal, as described by the Cassie-Baxter equation [135].

The second, and most important, observation is that the effect of counterface roughness is much more significant to the adhesive and frictional performance of the studied adhesive than the effect of surface chemistry. Our most hydrophobic surfaces showed only moderate decrease in surface forces compared to the most hydrophilic surfaces. However, even slight increase in surface roughness affects the contact performance tremendously, similar to earlier studies [62, 64, 66, 67, 130]. To this end, the water contact angle (or another metric of the surface chemistry effect, such as the work of adhesion) can be used to predict the performance of reversible dry adhesives only if the counterface is smooth. Otherwise, as can be seen in Figure 4-7, different materials can exhibit similar water contact angles/work of adhesion while having varying adhesive and frictional performance. Consequently, to design adhesives for operation against unpredictable substrates, after choosing a material that is least sensitive to counterface chemistry, such as PU, the main focus should be made on contact splitting, which can help

in reducing the surface roughness effects, as suggested in Refs. [15, 74, 130, 136] and will be demonstrated in the next chapter.

4.2.3 Comparison with Existing Models

The relationship between peeling force and surface roughness can be explained by classical asperity contact models [124, 137]. In the Greenwood and Williamson (GW) asperity contact model [124], when a smooth rigid surface is in contact with a reference rough surface, the real contact area A_r can be described as

$$A_r = \pi \beta N \int_d^\infty (z - d) \times \frac{1}{\sigma_s \sqrt{2\pi}} e^{-\frac{z^2}{2\sigma_s^2}} dz \tag{8}$$

where β is the mean radius of asperity summits, N is the number of asperities, d is the distance between two contacting surfaces, and σ_s is the standard deviation of the asperity heights with the assumption that the asperity height distribution is Gaussian. In addition, based on the GW model, Fuller and Tabor (FT) developed a contact model [137] that further considers adhesion. In the FT model, the total contact force per unit area between contacting surfaces can be described as shown in Eq. (9)

$$P = \frac{N(\frac{3}{2}\pi\beta\Delta\gamma)}{\sigma_s \sqrt{2\pi}} \int_d^\infty F\left(\frac{\delta}{\delta_c}\right) e^{-\frac{z^2}{2\sigma_s^2}} dz \tag{9}$$

$$\frac{\delta}{\delta_c} = \left(3\sqrt{F\left(\frac{\delta}{\delta_c}\right) + 1} - 1\right)\left\{\frac{1}{9}\left(\sqrt{F\left(\frac{\delta}{\delta_c}\right) + 1} + 1\right)\right\}^{\frac{1}{3}} \tag{10}$$

where $\Delta\gamma$ is the work of adhesion, δ is the indentation depth, and δ_c is the maximum extension of an asperity tip above its undeformed height before separation occurs. Using Eq. (8), it is easily seen that when all other parameters are fixed, the real contact area decreases as the standard deviation of the asperity heights increases, which corresponds to increase in surface roughness. Similar to Eq. (8), from Eq. (9), it can be seen that the normal force is proportional to N, β, and $1/\sigma_s$. This also reflects on adhesion, as was shown in a recent study of adhesive contact between rough rubber surfaces and a smooth glass lens [138]. Since the peeling force of wall-shaped microstructures also showed a good correlation with the integrative roughness parameter ($R_i = \frac{\sigma_s}{N\beta}$) in this study (Fig. 4-2d), it can be concluded that the relationship between peeling force and roughness agrees well with classical contact models.

Looking at the effects of the counterface chemistry on the pull-off and static friction forces, we conclude that, despite a wide range of tested materials, both are well pronounced but rather weak (see trendline equations in Figure 4-6). This implies that, to a first approximation, the effect of surface chemistry can be neglected when working with a PU-based adhesive, but if a more accurate estimation is needed, the work of adhesion (or the water contact angle) can help to predict its adhesive and frictional performances. It is worth noting, though, that contact interactions may also vary depending on the mechanical and geometric properties of the adhesive microstructure. To this end, in order to check how the surface chemistry effect changes with respect to the thickness and elastic modulus of adhesive thin-film-based flaps, we utilized the Kendall peeling model [55]. According to this model, the normal component of the maximum peeling force, $F_\perp$, can be described as

$$F_\perp = F sin\theta^* = bdE sin\theta^* \left(cos\theta^* - 1 + \sqrt{(cos\theta^* - 1)^2 + \frac{2R}{dE}} \right) \qquad (11)$$

where F is the total peeling force, b is the total peeling line length, E is the Young's modulus of the thin film material, d is the thin film thickness, θ^* is the optimal peeling angle found by solving

$$\frac{dF_\perp}{d\theta^*} = cos\theta^*(cos\theta^* - 1 + \sqrt{(cos\theta^* - 1)^2 + \frac{2R}{dE}}) + sin\theta^*(-sin\theta^* + \frac{(1 - cos\theta^*)sin\theta^*}{\sqrt{(cos\theta^* - 1)^2 + \frac{2R}{dE}}}) = 0 (12)$$

and R is the fracture energy per unit area that can be obtained using experimental data.

Substituting the measured maximum and minimum pull-off force values, the Young's modulus of 2 MPa, the film thickness of 20 μm, and the peeling line length of 11 mm into Eqs. (9) and (10), we found the fracture energy values of 1.07 and 0.57 N m^{-1} for 7525M Glass and PDMS, respectively. Using these fracture energy values, we solved Eqs. (9) and (10) for the corresponding pull-off forces, $F_\perp$, as a function of the Young's modulus and the film thickness, and calculated the maximum (for 7525M Glass) over minimum (for PDMS) pull-off force ratio, λ. This ratio, which represents the effect of counterface chemistry on pull-off force, is shown in Figure 4-8 as a function of the product of the Young's modulus (changed from 1 kPa to 1 GPa) and the film thickness (changed from 1 nm to 100 μm). It is obvious that the effect of counterface chemistry becomes more pronounced with increasing Young's modulus and flap thickness of the adhesive microstructure, but, for simplicity, we can conclude that it reaches 1.6 at largest for PU.
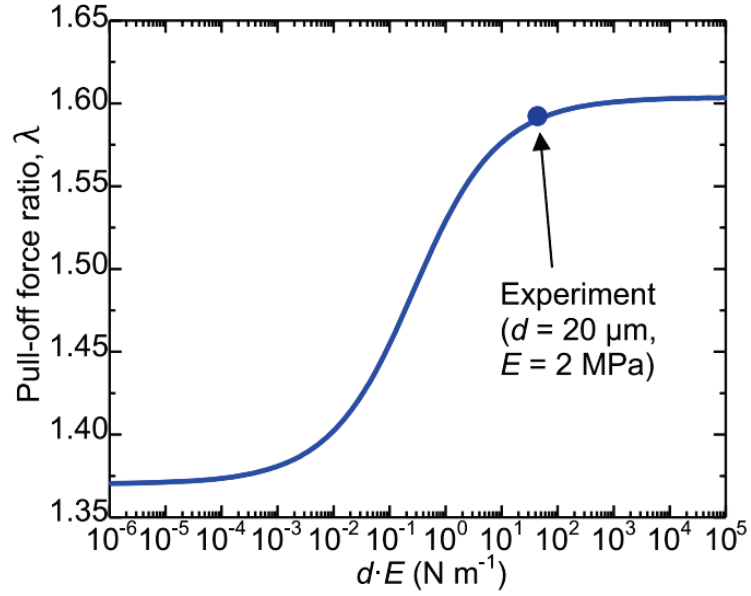
Figure 4-8 – The maximum over minimum pull-off force ratio, λ, with respect to the product of the Young's modulus, *E*, and the flap thickness, *d*.

4.3 Concluding Remarks

Based on the results presented in this chapter, we can conclude that because thin films can adapt to wavy, but not to rough surfaces, the adhesion- and friction-driven attachment of the wall-shaped microstructures degrades, regardless of the surface waviness, when the surface roughness increases.

Studying the effects of counterface chemistry on the attachment abilities of the PU-based shear-activated adhesive allowed us to draw the following conclusions. First, the pull-off and static friction forces we measured are found to be only moderately sensitive to the counterface chemistry, which makes PU a good material of choice for dry adhesives. Second, if the effect of counterface chemistry is to be considered, both types of contact

forces grow monotonically with increase in the work of adhesion. Third, when substrates are smooth (R_a < 50 nm), one can rank them with respect to their surface free energy by simply checking the contact angles of water. Last, when PU is used as the adhesive material, its attachment abilities are dominated by the effect of counterface roughness rather than counterface chemistry.

CHAPTER 5.   SHAPE AND MATERIAL PROPERTIES

In this chapter, the effects of the microstructure geometry, contact splitting, and elasticity on the adhesive performance are covered. Various microstructure geometries are manufactured by the drawing technique developed in this study. The contact splitting effect is examined by evenly splitting the original wall-shaped microstructure using razor blades. The effect of elasticity is examined by using several PU materials with different Young's modulus.

5.1   Experimental Details

5.1.1   *Sample Preparation*

To study the effect of microstructure geometry, two types of laboratory razor blades were used as drawing elements – thick Carbon Steel blades with thickness of 229 μm and the tip angle of 18º, and thin Stainless Steel blades with thickness of 76 μm and the tip angle of 22º. Both the sharp (V-shaped) and the blunt (U-shaped) edges of the blades were used for drawing. The average roughness, R_a, of the sharp and blunt sides of the thick blades were 0.28 μm and 0.14 μm, respectively, and R_a of the sharp and blunt sides of the thin blades were 0.15 μm and 0.14 μm, respectively. 3M Scotch Magic 810 double-side adhesive tape was used as a spacer for even separation of adjacent U-shaped drawing elements, whereas the V-shaped drawing elements were assembled without spacers. The blades were aligned and assembled to make microstructures on an area of at least 2.5 mm in width, while the gaps between thick and thin U-shaped drawing elements were about

240 and 60 μm (4 and 1 sheet of the spacer tape), respectively, and the gaps between the tips of thick and thin V-shaped drawing elements were 229 and 76 μm (blade thicknesses), respectively. With the U-shaped and V-shaped drawing elements, 11 different geometries were fabricated by using the drawing-based manufacturing. The two types of soft polymer composed of base material and curing agent were used to draw the adhesive microstructures: PVS and PU, with Young's moduli of 3 and 2 MPa, respectively. To fabricate the microstructures, the curing polymer mixture was first smeared onto the glass slide (after dwell times of 30 s for PVS and 720 s for PU) using a razor blade and spacers to have a uniform thickness of about 300 and 180 μm for thick U-shaped and V-shaped drawing elements, respectively, and of about 120 μm for thin drawing elements of both types. The specific manufacturing parameters are presented in Table 5-1.

Table 5-1 – Manufacturing parameters used to prepare PVS and PU microstructures shown in Figure 5-1.

Material	Type	Backing layer thickness (μm)	Smearing Time (s)	Dipping Time (s)	Drawing Time (s)	Dipping distance (μm)	Drawing distance (μm)	Dipping speed (μm s⁻¹)	Drawing speed (μm s⁻¹)
PVS	KU1	300	30	50	70	180	168	12	600
	KU2	300	30	50	70	180	96	12	600
	KV1	180	30	50	70	168	120	12	600
	KV2	180	30	50	70	96	144	12	600
	NV1	120	30	60	70	84	72	12	600
	NU1	120	30	60	70	36	36	12	600
	NU2	120	30	60	70	72	36	12	600
PU	KU1	300	720	1080	1110	144	120	12	600
	KU2	300	720	1080	1110	144	96	12	600
	KV1	180	720	1080	1110	144	120	12	600
	NU2	120	720	1140	1170	96	48	12	600

To examine the effect of contact splitting, the original wall-shaped projections (Figure 5-1a) were split at 100-µm intervals (Figure 5-1b) using a razor blade fixed to an LP150 Low Profile X-Y Stage (Reliant Systems, Zimmerman, MN, USA). The epoxy substrates with various roughness shown in Figure 4-1 were fabricated by using a two-step replication (see chapter 4.1.1) in order to use them as counterface.
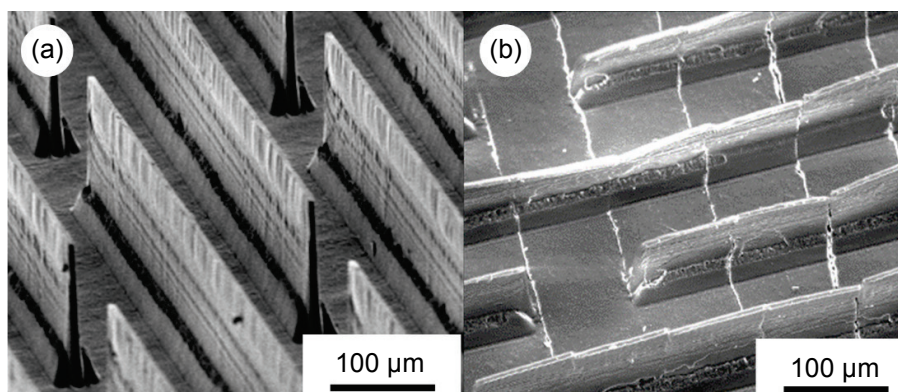
Figure 5-1 – SEM images of PVS wall-shaped adhesive microstructures in (a) original state and (b) split state at 100 µm intervals.

In order to work with different Young's moduli, four different PUs (PU; F-130 REV1, F-150 REV1, F-161 REV1, and F-180 REV1; BJB Enterprises, Tustin, CA) were used to draw adhesive microstructures. A set of stainless steel razor blades of 229 µm in thickness was used as a drawing array. First, eight razor blades were arrayed with an inter-blade gap of about 240 µm formed by 4 sheets of the tape Scotch Magic 810 and the drawing array was assembled to a linear actuator built in a contact angle measurement system OCA 25. The drawing array was assembled such that their blunt edges faced the polymer. Second, the curing polymer was smeared onto a glass slide (after a designated

dwell time measured from mixing two compounds of PU) using a razor blade and spacers to have a uniform thickness of about 300 µm. Third, the drawing array was dipped into the curing polymer mixture to a dipping distance of 144 µm at a designated dipping time and then withdrawn to a drawing distance of 120 µm at a designated drawing time, with the help of the linear actuator in the contact angle measurement system OCA 25. After 6 hours, when the drawn microstructures were cured enough to be released, the drawing array and the PU microstructured sample were disassembled from the drawing setup, and placed into a water-filled M1800H ultrasonic bath for an hour before the sample was released. Table 5-2 shows the smearing time, dipping time, and drawing time measured from the beginning of mixing two PU compounds.

Table 5-2 – Manufacturing parameters used to fabricate PU microstructures having different Young's modulus.

PU type	Young's modulus (MPa)	Backing layer thickness (µm)	Smearing Time (s)	Dipping Time (s)	Drawing Time (s)	Dipping distance (µm)	Drawing distance (µm)	Dipping speed (µm s^{-1})	Drawing speed (µm s^{-1})
F-130	1.14		720	1200	1230				
F-150	2.07	300	720	960	990	144	120	12	2400
F-161	4.48		300	400	430				
F-180	14.48		720	1080	1110				

5.1.2   Testing Procedure

Samples of 2 mm in diameter were cut out of the microstructured polymer sheets using a disposable biopsy Uni-Punch. The samples were cleansed with deionized water, dried in blowing Nitrogen and then fixed in place. To study the effect of the microstructure

geometry and elasticity, a glass slide having size of 30×5×1 mm and roughness average, R_a, of 5 nm was used as a counterface. To study the effect of contact splitting, the epoxy substrates with various roughness shown in Figure 4-1 were used as counterface. Tested surfaces were inspected with an M125 optical stereomicroscope and imaged in the SEM, which was operated in a high-vacuum mode at 1.5 kV to enable charge-free imaging of non-conductive samples in their natural state.

After fixing the samples so that the microstructure projections were perpendicular to the sliding/pulling direction, the load-drag-pull test was run while recording generated normal and tangential forces. First, the counterface was moved in perpendicular to the contact plane until a designated normal load (10 mN for all the cases except the PU sample with Young's modulus of 14.5 MPa, which was tested under the load of 50 mN) was achieved. Then, the counterface was moved in parallel to the contact plane under the same normal load and at a speed of 100 μm s^{-1} for a designated preliminary distance ranging from 200 to 400 μm with intervals of 50 μm in order to achieve maximum pull-off force. Next, the counterface was withdrawn from the contact at the speed of 100 μm s^{-1} at the pulling angle of 90°. The test stopped at a complete detachment of the glass slide from the structured sample. Four samples of each case were tested, and because testing one sample repeatedly gave exactly the same result, test variance was calculated based on 4 repetitions of each measurement point (one repetition for each sample). The testing was conducted at the temperature and relative humidity of 23-25 °C and 45-50 %, respectively.

5.2 Results and Discussion

5.2.1 Effect of Microstructure Geometry

The microstructures shown in Figure 5-2 have been drawn from PVS and PU using the parameters presented in Table 5-1. Figure 5-2 demonstrates that a large variety of hierarchical microstructures can be fabricated by making subtle changes in processing parameters and by using drawing elements as simple as common laboratory blades. It is worth noting though that we could not fabricate some of the microstructures from PU, supposedly due to a high adhesion between the polymer and the blades that led to problems during release stage (we assume that the release process and the performance of the resulting microstructures can be improved by using drawing elements having lower surface free energy and roughness than those of the steel blades we used in this work). Images of normally and tangentially loaded microstructures are also shown in Figure 5-2 (2nd and 3rd column in each material), which helps to shed light on differences in their adhesive and frictional performance discussed below.
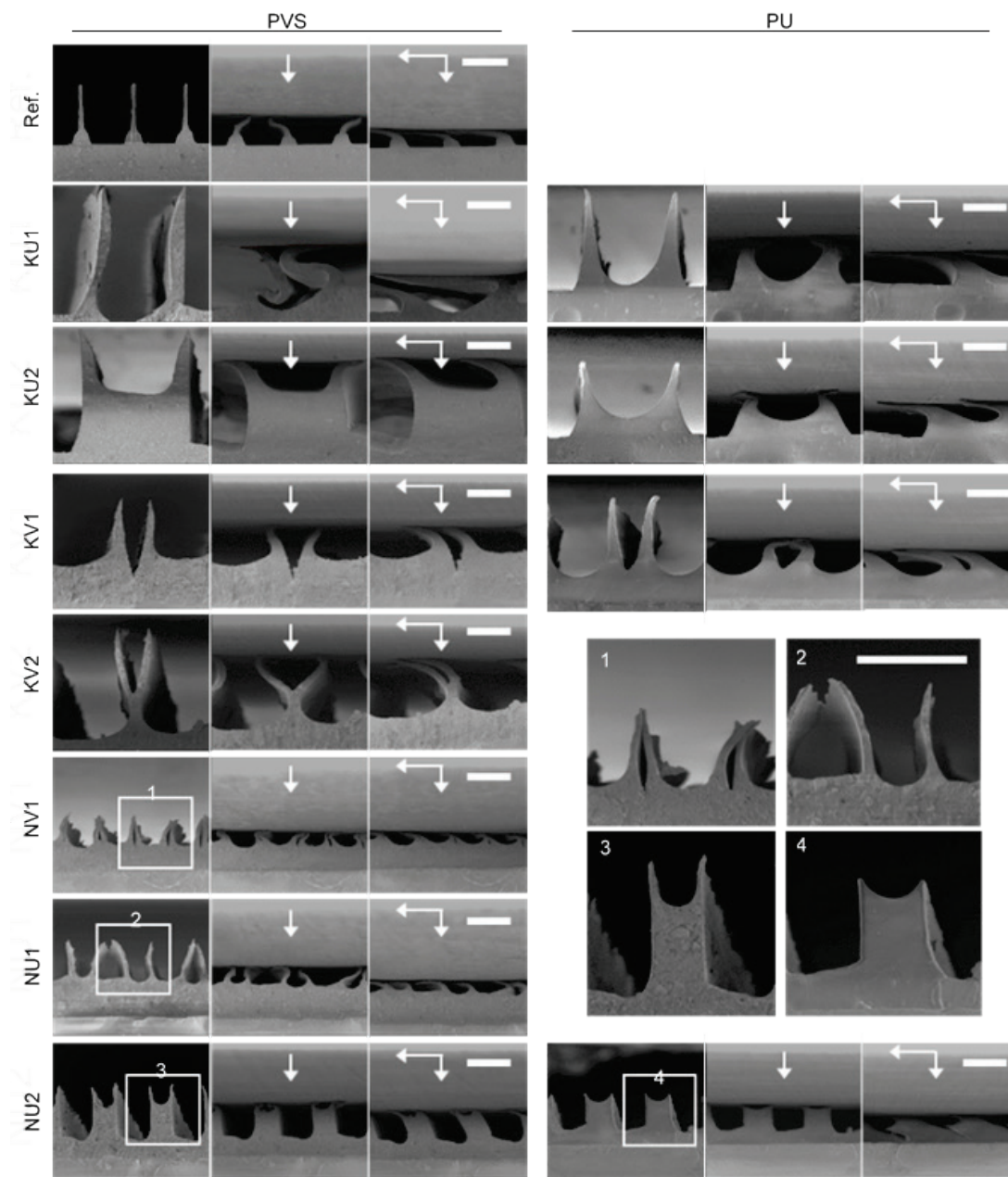
Figure 5-2 – PVS and PU structures fabricated and loaded differently. Ref.: molded against laser-machined template. KU1, KU2: drawn by thick (marked as K) U-shaped blade edges. KV1, KV2: drawn by thick V-shaped blade edges. NV1: drawn by thin (marked as N) V-shaped blade edges. NU1, NU2: drawn by thin U-shaped blade edges. 1-4: Close-up of the structures drawn by thin blades. Arrows in the direction of loading (by glass counterface). Scale bars: 100 μm.

82

To study how differently drawn microstructures compare to each other and to the original molded surface (Ref. sample, Figure 5-2) [122], we have measured pull-off force in both non-activated and shear-activated states, and friction force at the sliding inception. As seen in Figure 5-3, the studied structures showed adhesion strength of up to 10 kPa and frictional strength of up to 60 kPa, which are comparable to those of other shear-activated adhesives [26, 30, 87, 100]. In addition, as seen in Figure 5-3a, the PU microstructures show higher pull-off force in both the non-activated and shear-activated states (up to 32.4 mN) than the PVS microstructures (up to 15.5 mN), which can be attributed to higher tackiness of PU. On the other hand, thinking in terms of amplification factor (the ratio of active- over passive-state pull-off force), the PVS microstructures seem to be more useful than their PU counterparts because the best amplification factor of PU (NU2 sample) is about 15, while the best amplification factor of PVS (also NU2) is at least 40 (if instead of the passive pull-off force, which was found to be lower than the measured noise level of ±0.2 mN, we use the force value of 0.4 mN). This is most likely because PVS is stiffer than PU, so the former stores more reactive elastic energy in the non-activated state, leading to a much lower pull-off force (a difference between elastic reaction and adhesion). It is also evident that the majority of the drawn microstructures show comparable or higher shear-activated pull-off force than the molded reference. This is probably the most important finding shown in this chapter demonstrating the superiority of inexpensive and simple drawing over expensive and complicated molding in the manufacture of shear-activated dry adhesives. Interestingly, the above amplification factor of 40 is much greater than that of about 15 demonstrated recently by a molded wedge-shaped adhesive [40], or those of about 2 and 4 demonstrated earlier by molded pillar-based adhesives [139, 140].
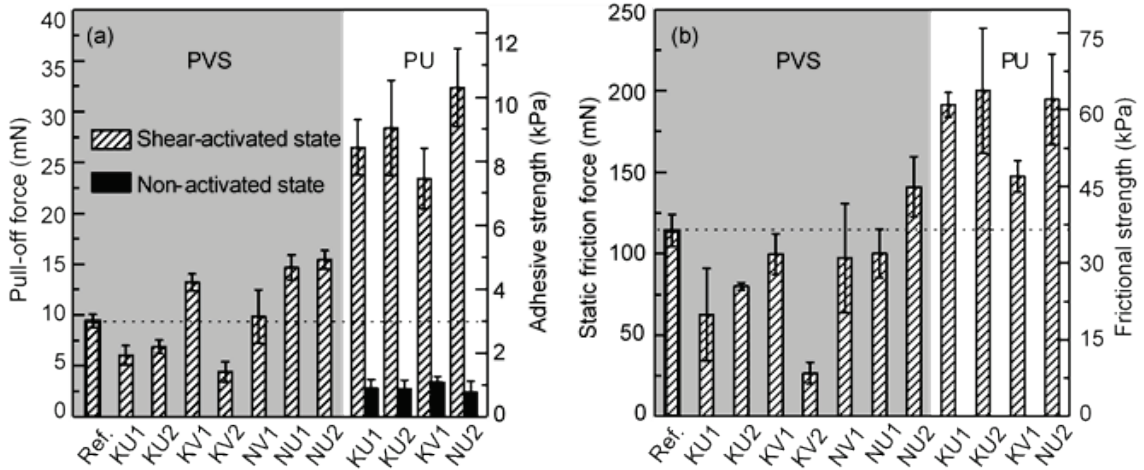
Figure 5-3 – (a) Pull-off force/adhesive strength in shear-activated and non-activated states, and (b) static friction force/frictional strength of PVS and PU surfaces shown in Figure 5-2. Error bars represent standard deviation.

Comparing adhesive performance of different PVS microstructures to each other (Figure 5-3a), we see that KU1 and KU2 samples show similar pull-off force of about 0.7 of the Ref. sample because similar reductions in the microstructure density lead to a shorter total peeling line length (the sum of lengths of all wall-shaped projections) [15]. The KV1 sample, which shows the best adhesive performance among the microstructures drawn using thick blades, demonstrates a pull-off force of about 1.4 of the Ref. sample due to about the same increase in the total peeling line length. It is worth adding that the twofold increase in pull-off force associated with replacing U-shaped drawing elements with V-shaped drawing elements is obtained because the drawing array assembled from V-shaped elements does not require spacers, so a higher density of adhesive flaps can be achieved. However, if the adhesive flaps drawn by V-shaped elements are too compliant, as in the

KV2 and NV1 samples, they tend to stick pairwise, effectively reducing the total peeling line length by a factor of two and leading to a corresponding reduction in pull-off force. NU1 and NU2 samples have a total peeling line that is three times as long as that of the KU1 and KU2 samples, which makes them the best PVS microstructures, with pull-off force of about 1.5 of the Ref. sample.

Comparing the adhesive performance of different PU microstructures, we see that, similar to PVS, the KU1 sample shows a slightly lower pull-off force than the KU2 sample. However, in contrast to PVS, the KV1 sample shows lower pull-off force than the KU1 and KU2 samples, which happens because paired PU flaps can easily stick to each other, eventually working as just one flap. Interestingly, though the NU2 sample has only rudimentary flaps, it shows the best adhesive performance among all microstructures, which suggests that the total peeling line length is one of the most important factors affecting shear-induced attachment.

The frictional performance of the studied microstructures is shown in Figure 5-3b and it is clear that their relative positions are generally similar to those obtained in measuring pull-off force, although the Ref. sample stands a little higher with respect to other samples. All but one of the samples drawn from PVS exhibit lower friction than the Ref. sample, although their frictional performance is far from being poor, with the friction to load ratio ranging from about 3 to 14 (12 for the Ref. sample). The friction to load ratio for PU ranges from about 14 to 20.

The reasons for the differences in frictional performance of the drawn samples are thought to be similar to those mentioned with respect to their adhesive performance, while

the reason for a general downshift of all drawn samples with respect to their molded reference is most likely related to surface quality. The drawn microstructures undergo high stresses during forming, which results in the appearance of wrinkles and bumps on their surfaces that reduce the real contact area, while the surfaces of the molded reference are much more uniform. To this end, since the frictional sliding is much more sensitive to the real contact area than the adhesive peeling, the surface quality impacts frictional performance to a somewhat greater extent.

It is also important to evaluate the durability of the drawn adhesives. We do not have formal data on the number of attachment/detachment cycles our microstructures can withstand, however, given that this property is a function of material rather than geometry and that there are several reports on high durability of mushroom-shaped adhesive microstructures made of PVS and PU [141-144], the drawn wall-shaped microstructures are expected to last a long time if made from these materials. This assumption, however, has to be verified in the future.

Another question is related to the reproducibility of the fabrication method, and associated variance in performance. Although the drawn microstructures obviously cannot be as precise as those prepared by molding, since the main issue leading to dimensional inaccuracy is the polymer sinking during curing, the reproducibility can be significantly improved if the polymer is cured right after drawing by UV light or heat. In any event, even the current microstructures have reasonable variance in pull-off and static friction forces since the performance is averaged over large contact area.

5.2.2   Effect of Contact Splitting

Analyzing the effect of contact splitting, we can undoubtedly see that, in agreement with the common belief, it can effectively mitigate the roughness-driven reduction of the pull-off force as shown in Figure 5-4. This observation is supported by a paired t-test (one-tailed P-value=0.00152), according to which the mean pull-off force measured with the split microstructure exceeds that measured with the original microstructure by an amount that is greater than would be expected by chance. This key finding is demonstrated by the observation that increased roughness leads to a less pronounced reduction of the pull-off force if the micro-structured surface is split, with this effect being more notable at the intermediate roughness, and vanishingly small at the very smooth and very rough surfaces. We can associate this effect with the changes in the real contact area. If the counterface is smooth, splitting the microstructure does not affect the real contact area. If the counterface is highly uneven, the real contact area is so small that its increase due to the improved adaptability of the split microstructure (to wavy surfaces) cannot cause an increase in the pull-off force to exceed the measurement error. On the other hand, the improved adaptability of the split microstructure to wavy surfaces allows it to form a larger contact area (Figure 5-5) on the surfaces with intermediate roughness, thus leading to a better attachment.
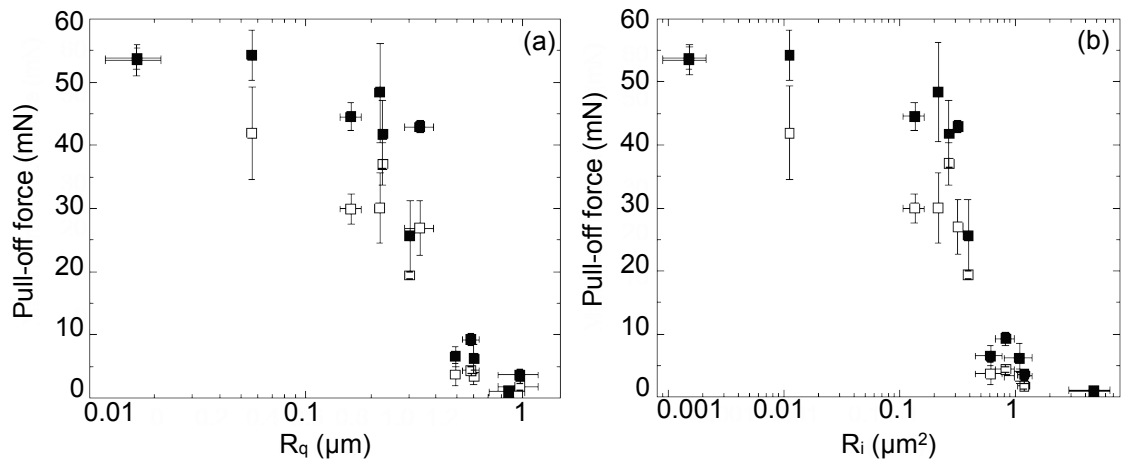
Figure 5-4 – Pull-off force measured after preload of 20 mN on different rough surfaces and represented as a function of (a) Rq and (b) Ri calculated based on roughness profiles obtained after Gaussian high-pass filtering with the cut-off wavelength of 10 μm. Open and filled markers represent mean values measured with original and split microstructures, respectively. Error bars represent standard deviation.
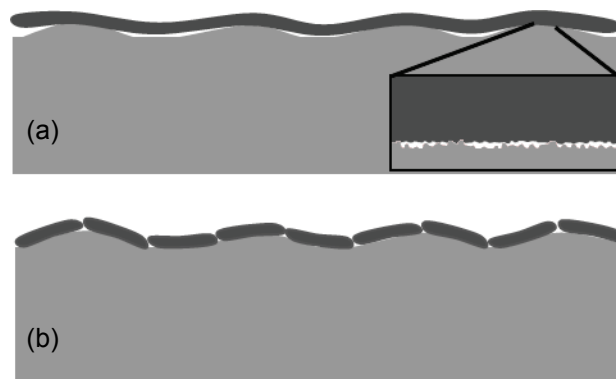
Figure 5-5 – Schematic of the terminal parts of an (a) original as-cast and (b) split at 100 μm intervals wall-shaped microstructure in contact with a counter surface.
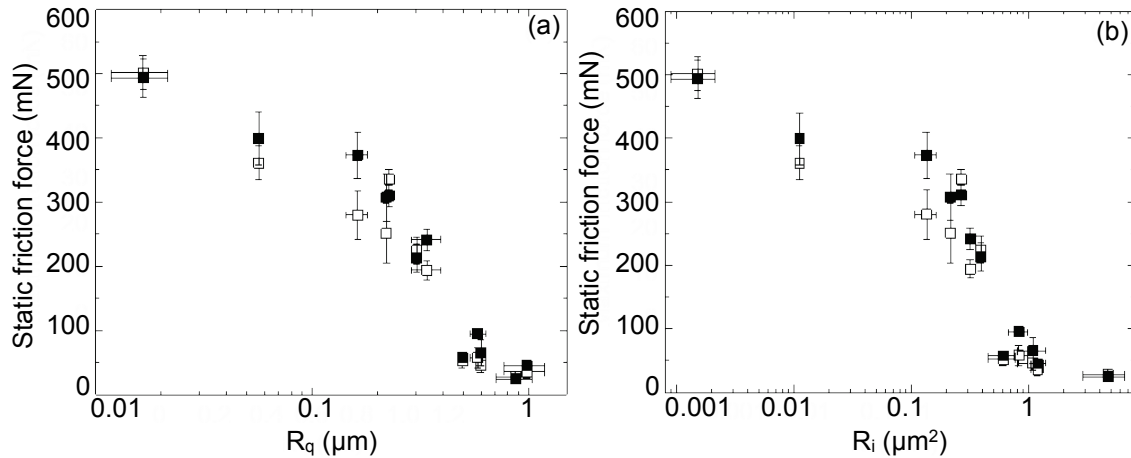
Figure 5-6 – Static friction force measured under normal load of 20 mN on different rough surfaces and represented as a function of (a) Rq and (b) Ri calculated based on roughness profiles obtained after Gaussian high-pass filtering with the cut-off wavelength of 10 μm. Open and filled markers represent mean values measured with original and split microstructures, respectively. Error bars represent standard deviation.

Splitting the wall-shaped microstructures also seems to increase the resistance to sliding, with this effect being more pronounced at intermediate roughness as shown in Figure 5-6. As with the effects observed with the pull-off force, this may happen due to a more efficient use of the available surface area by the split wall-shaped microstructures. On the very smooth and very rough substrates, this effect disappears because the real contact area is not affected by the contact splitting in the first case, and because the real contact area is so small in the second case that its growth due to contact splitting is comparable to the measurement error. Interestingly, a paired t-test gives a one-tailed p-value of 0.0256, which means that the mean friction force measured with the split

microstructure exceeds that measured with the original microstructure by an amount that is greater than would be expected by chance. This figure is more than one order of magnitude larger than that obtained for the pull-off force, which suggests that the contact splitting may be more useful in mitigating the roughness-driven reduction of the pull-off force, while the force needed to start sliding is affected less.

5.2.3   Effect of Elasticity

The attachment force to be overcome to separate two surfaces in adhesive contact, i.e. the pull-off force, is defined by the sum of attractive forces associated with surface interactions and repulsive forces associated with the elastic reaction of a deformed bulk material [145]. Obviously, in case of a shear-activated adhesive, attractive and repulsive forces should be maximized and minimized alternatively depending on whether an activated or disactivated mode of operation is required. Given that surface forces are known to change within a relatively limited range [146], this suggests that having proper material elasticity is critical to obtain a desired balance between the attachment abilities of a certain contact element geometry in its "on" and "off" states.

To this end, four types of PU microstructured samples with different Young's modulus of 1.14, 2.07, 4.48, and 14.48 MPa were tested to see the effect of elasticity on the activated (shear-induced) and deactivated (no shear applied) pull-off forces. As shown in Figure 5-7, the activated and deactivated pull-off forces decrease as the Young's modulus of the adhesive microstructure increases. The most compliant sample (Young's modulus of 1.14 MPa) showed the highest activated pull-off force of ~35 mN and the highest deactivated pull-off force of ~12 mN. This implies that while the softest sample can generate the highest pull-off force when shear-activated, it cannot be easily detached

due to the high deactivated pull-off force. Hence, it is less suitable for situations where the ability to control adhesion is strongly required. The stiffest sample (Young's modulus of 14.48 MPa) showed the lowest activated pull-off force of ~13 mN and deactivated pull-off force of below the sensitivity level of the tribotester. Compared to the sample with the Young's modulus of 1.14 MPa, the controllability of its attachment/detachment performance is much higher. This controllability can be conveniently represented using the amplification factor (the ratio of activated pull-off force over deactivated pull-off force).
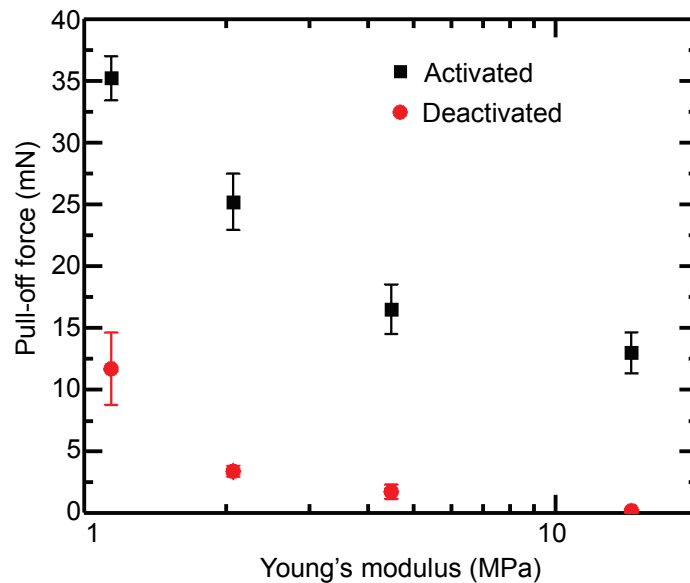
Figure 5-7 – Activated and deactivated pull-off force of PU microstructured adhesive as a function of Young's modulus. Error bars represent standard deviation.

As can be seen in Figure 5-8, the amplification factor of the PU wall-shaped microstructured samples calculated using the data presented in Figure 5-7 increases as the Young's modulus increases. This is attributed to the fact that the adhesive abilities of disactivated flaps (see Figure 3-1 for illustration of "on" and "off" states of adhesive flaps) reach zero much faster than those of activated flaps, so the force ratio increases. However, it should be noted that not only the amplification but also the activated pull-off force is

important because the activated pull-off force represents the attachment performance, while the amplification factor represents the ability to switch between "on" and "off" states. Therefore, the Young's modulus of the microstructured adhesive should be carefully chosen when designing for specific applications.
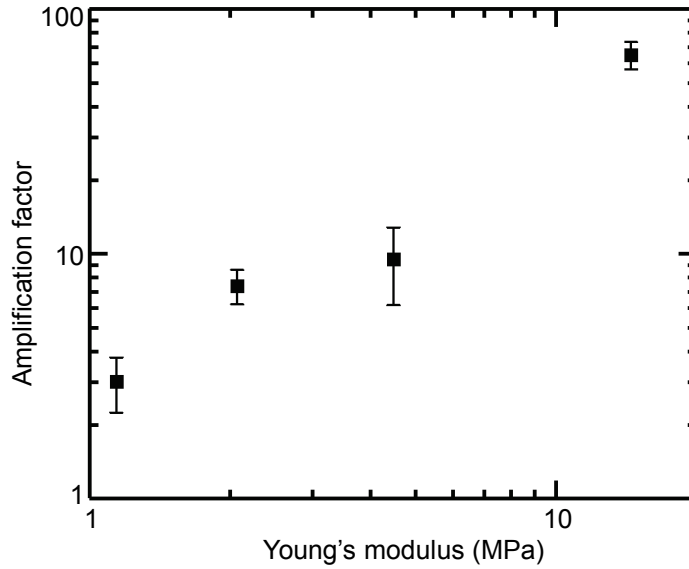
Figure 5-8 – Amplification factor of the PU microstructured adhesive as a function of Young's modulus. Error bars represent standard deviation.

5.2.4   Comparison with Existing Models

As expected from the Kendall model of thin-film peeling [55], Eq. (1), longer total peeling line length generated higher peeling force in testing different wall-shaped adhesive microstructures. However, the effect of the flap thickness, which is expected to correlate to the peeling force according to Eq. (1), could not be reliably verified because the tested

flaps are not uniform (see Figure 5-2), while the Kendall model describes peeling of a film with a uniform thickness.

Considering the effect of contact splitting, in addition to its better ability to adapt to uneven surface topography, a split microstructure may also demonstrate another effect that facilitates attachment. This effect is based on a non-linear relationship between the peeling force and the peeling angle, as follows from the Kendall model of thin-film peeling [55]. It is evident that the Kendall model cannot be directly applied to interpret our results due to different boundary conditions. However, it provides a useful example that qualitatively illustrates the effect we may expect to see.

Shearing an original and a split flap against an uneven substrate, we may expect that they will form contacts similar to those shown in Figure 5-9a, with the original flap being peeled at the same angle along all its width and the split (independent) flap being peeled at slightly different angles associated with the local surface slopes. Now, we can simplify and transpose this 3D model into a 2D space, as shown in Figure 5-9b, so the original flap peels at angle θ, while the two statistically equal fractions of the split flap peel at angles θ-α and θ+α, respectively, with α being a small perturbation angle defined by the surface topography. In this case, solving the Kendall equation ((2) in [55]) yields

$$\frac{F}{b} = dE \left\{ (cos\theta cos\alpha - 1) + \frac{1}{2} \left[\sqrt{(\cos(\theta + \alpha) - 1)^2 + \frac{2R}{dE}} + \sqrt{(\cos(\theta - \alpha) - 1)^2 + \frac{2R}{dE}} \right] \right\} \tag{13}$$

where F is the peeling force, b is the film width, d is the film thickness, E is the Young's

modulus, and R is the fracture energy.
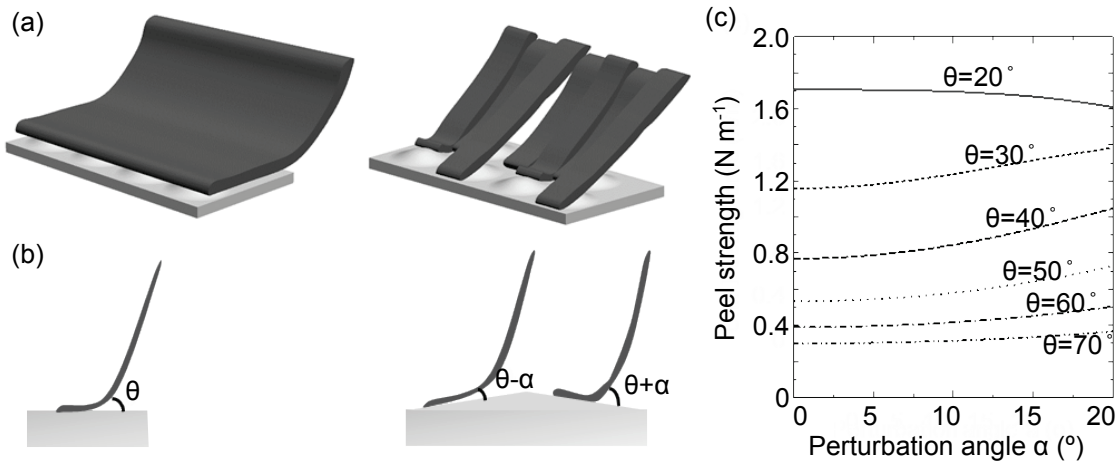
Figure 5-9 – The effect of flap splitting on the contact geometry in (a) 3D representation and (b) 2D representation. (c) Peel strength of a split adhesive flap as a function of the peeling angle θ and the perturbation angle α.

Plotting the peel strength, which is the peeling force normalized by the film (flap) width, gives the curves shown in Figure 5-9c when the film (flap) thickness is 5 μm, the Young's modulus is 3 MPa, the fracture energy is 0.2 N m^{-1}, the peeling angle θ ranges from 20° to 70° and the perturbation angle α ranges from 0° to 20°. Studying these curves, we see that the peel strength can either increase or decrease with increasing perturbation angle α at different peeling angles θ. At peeling angles below ~25°, the increase in perturbation angle (increase in surface unevenness) results in a decrease in the peel

strength, while at peeling angles above ~25°, the increase in perturbation angle results in an increase in the peel strength. Thus, given that the tested adhesive microstructure is loaded at high peeling angles in this work, we can conclude that splitting the adhesive microstructure in parallel to the peeling force may improve the attachment ability not only thanks to better adaptation to surface topography, but also thanks to the effective decrease of the peeling angle.

The effect of elasticity on peeling performance cannot be readily explained using classical thin-film peeling models such as Kendall model [55] because the Young's modulus affects the peeling angle and possibly the real total peeling line length. In addition, the peeling angle to be expected for our microstructures of rather complex geometry cannot be obtained using theoretical models dealing with much simpler geometries. Thus, the effect of Young's modulus needs to be verified using numerical simulation studies in the future.

5.3   Concluding Remarks

Several different types of adhesive microstructures were fabricated using the drawing technique developed in this work, and the studied microstructures showed adhesion strength of up to 10 kPa and frictional strength of up to 60 kPa, which are comparable to those of other shear-activated adhesives. The best of our adhesives demonstrated shear-driven amplification of pull-off force by a factor of 40, which significantly outperforms known molded analogues.

Splitting the wall-shaped microstructure in parallel to the shear direction helps to mitigate the negative effect of the increasing surface unevenness by allowing the split microstructure to adapt easier to the surface waviness as well as by allowing it to reduce the effective average peeling angle. These findings can guide the development of biomimetic shear-actuated adhesives that are suitable for operation not only on smooth but also on rough surfaces.

Studying the effect of elasticity, we found that the wall-shaped microstructured adhesive can exhibit higher amplification factor with increasing Young's modulus. However, it should be noted that not only the amplification but also the maximum pull-off force is important to represent the attachment abilities comprehensively. Therefore, the Young's modulus, or, in other words, the material, should be carefully chosen when designing shear-activated adhesives for a specific application.

CHAPTER 6.   CONCLUSION

6.1   Summary

The objective of this work was to study the attachment performance of the wall-shaped adhesive microstructures, and to explore the possibility to manufacture them in a different way. This goal was successfully achieved by studying the effects of various parameters on the adhesive and frictional performances, and by developing a working drawing-based technique for manufacturing thin-film-based surface projections. The following conclusions can be drawn from this study.

1. In accord with the prediction of the Kendall model for the normal component of peeling force, there is an optimal normal force that is required to detach the wall-shaped adhesive microstructure. The optimum is obtained at about half the distance needed to initiate sliding and at pulling angles that range within 60–90°, which suggests that the wall-shaped microstructure can tolerate relatively large inaccuracies in the loading direction. The increase of the attachment force with increasing flap height is found to correlate with the flap thickness, which decreased with increasing flap height.

2. The adhesion- and friction-driven attachment of the wall-shaped microstructure degrades, regardless of the surface waviness, when the surface roughness increases. In addition, splitting the wall-shaped microstructure indeed helps to mitigate the negative effect of the increasing surface unevenness by allowing the split microstructure to adapt more easily to the surface waviness and by reducing the effective average peeling angle.

97

3. From the tests of the attachment properties of polyurethane (PU) in contact with several substrates of different chemical composition, it was found that the pull-off and static friction forces measured with our PU-based adhesive are only moderately sensitive to the counterface chemistry, which makes PU a good material of choice for dry attachment systems. In addition, the effect of counterface roughness was clearly demonstrated to dominate over the effect of counterface chemical composition.

4. Unlike conventional mold-based manufacturing techniques, a novel cost-effective, simple, and flexible drawing-based technique for manufacturing the soft elastomeric thin-film-based microstructures has been newly developed for successful implementation of the principles of biological shear-activated adhesion. Several different types of adhesive microstructures were fabricated by changing manufacturing parameters such as dipping and drawing distances and the drawing tip shape. The best of them demonstrated a shear-driven amplification of the pull-off force by a factor of 40, which significantly outperforms known molded analogues, while this amplification factor was shown to grow with increasing Young's modulus of the microstructure.

As shown in Table 6-1, the wall-shaped adhesive microstructures showed a superior ability to switch between the activated and deactivated states and comparable maximum adhesive and frictional strengths to other switchable dry adhesives.

Table 6-1 – Comparison of adhesive and frictional performance for various switchable dry adhesives. The first two rows (shaded gray) represent this study.

Structure	Material (Young's modulus in MPa or mixing ratio)	Activated adhesive strength (kPa)	Deactivated adhesive strength (kPa)	Max. shear strength (kPa)	Ref.
Wall	PVS (3)	5	~0	45	[107]
Wall	PU (2)	10	0.7	62	[107]
Wall	PVS (3)	N/A	~0	76	[33]
Flap	PU (25)	12.5	3	28	[147]
Flap	PU (2)	14	N/A	54	[31]
Wedge	PDMS (10:1)	10.5	2.5	50	[40]
Wedge	PDMS (1.8)	9.4	N/A	78	[87]
Wedge	PDMS (1.75)	5	~0	17	[30]
Hierarchical wedge	PDMS (0.7)	2.8	N/A	N/A	[152]
Wedge + micropillar	PDMS (8:1)	23.5	N/A	60	[151]
Anisotropic mushroom	PDMS (10:1)	80	17	N/A	[148]
Micropillars on slanted lamella flaps	HDPE (900)	N/A	N/A	2.5	[149]
Tilted micropillar	PP (1500)	N/A	N/A	45	[150]

6.2 Research Contributions

1. Understanding of the attachment mechanism and limitations of the wall-shaped adhesive microstructures with various material and geometric properties, tested under different loading and surface conditions:

   a. Significant and negligible pull-off forces can be achieved by controlling the preliminary tangential displacement and pulling angle.

b. Contact splitting can reduce the negative effect of the counterface topography by improving adaptability of the contact elements.

c. PU can be chosen as a suitable material for shear-activated adhesives due its low sensitivity to the counterface chemistry.

d. Unlike the effect of counterface chemistry, the counterface roughness effect cannot be neglected.

e. The amplification factor in shear-activated adhesives can be maximized by adjusting the Young's modulus.

2. Highlighting of a path to an easy, potentially scalable cost-effective technique for manufacturing bio-inspired thin-film-based dry adhesives using a drawing method:

a. The wall-shaped adhesive microstructures can be fabricated using common laboratory razor blades.

b. Drawn shear-activated adhesives can perform better than their molded analogues.

3. Guidance for a possible re-design of the current transfer tools, as well as for the design of future cost-effective, efficient, clean, easily detachable and simple grippers for industrial and domestic use:

a. Attachment/detachment of shear-activated adhesives can be efficiently controlled by assessing tangential resistance in loading system.

b. Grippers based on shear-activated adhesives can be designed based on just two opposingly actuated jaws, such as in a centering vise.

c. The need in auxiliary equipment and counterface-related limitations can be significantly reduced.

6.3 Possible Applications

Because the wall-shaped adhesive microstructures attach and detach using shearing, their operation can be tested on a macro scale with a simple manually controlled tool. To demonstrate the feasibility of such a gecko-inspired gripping tool, two types of simple devices were made based on a center-clamping vise as shown in Figure 6-1. The center-clamping vise was used to generate the required tangential motion by rotating a knob in the vise. Doing so in counterclockwise or clockwise direction, the gripper could generate relative motion in the proximal or distal direction. The gripper for flat objects used a rigid material as the substrate for the adhesives. However, the gripper for curved objects used a soft material for the backing substrate to grip various curved objects by making conformal contact.

To demonstrate the wall-shaped adhesive microstructures in actual operation, we chose the KV1 drawn PVS sample. This choice was made to have a larger adhesive amplification factor (PVS) and a better robustness (bigger size of KV1 microstructure allows it to tolerate larger loading inaccuracies). A small manual center-clamping vise (Mitutoyo, Kawasaki, Japan) was fitted with the chosen adhesive to handle flat and curved objects. Two sets of KV1 PVS samples with a total area of about 1760 mm^2 were attached to two glass slides fixed to the vise jaws, which allowed the pick-and-release of a 150 g iPhone 8 (Apple, Cupertino, California) by rotating the vise knob to tighten or loosen the

grip (Figure 6-2a). To grip curved objects, the microstructured samples were attached to two flexible vinyl sheets backed by common soft packaging foam connected to the vise to enable conformal contact with curved objects (Figure 6-2b). As shown in Figure 6-2, the gripper could successfully assist in lifting/releasing such everyday objects as smartphones, eggs, tomatoes, lemons, etc. when in a shear-activated/disactivated mode. It is also important to note that the gripping process was robust and did not require high precision in controlling the vise jaws, making it easy to implement in industrial and domestic environment.
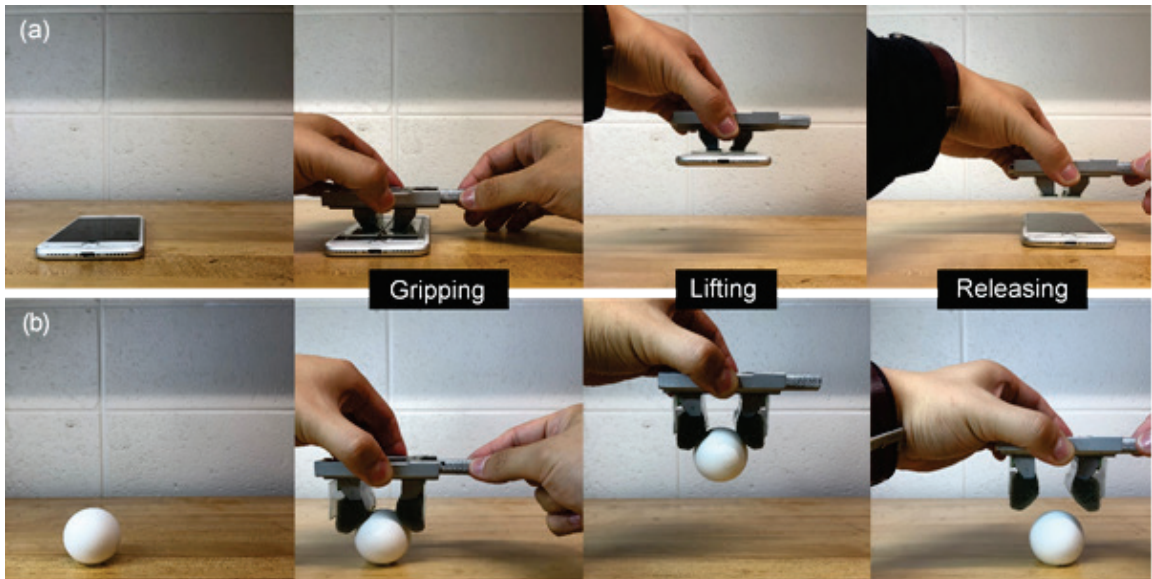
Figure 6-1 – Schematic of the grippers for flat and curved objects based on the wall-shaped microstructured adhesive, and the working principle for gripping and releasing states.

	Schematic	Gripping	Releasing
For flat objects	Tangential displacement / Dry adhesive / Glass slide (hard backing) / Centering vise		
For curved objects	Sponge (soft backing) / Dry adhesive / Glass slide		
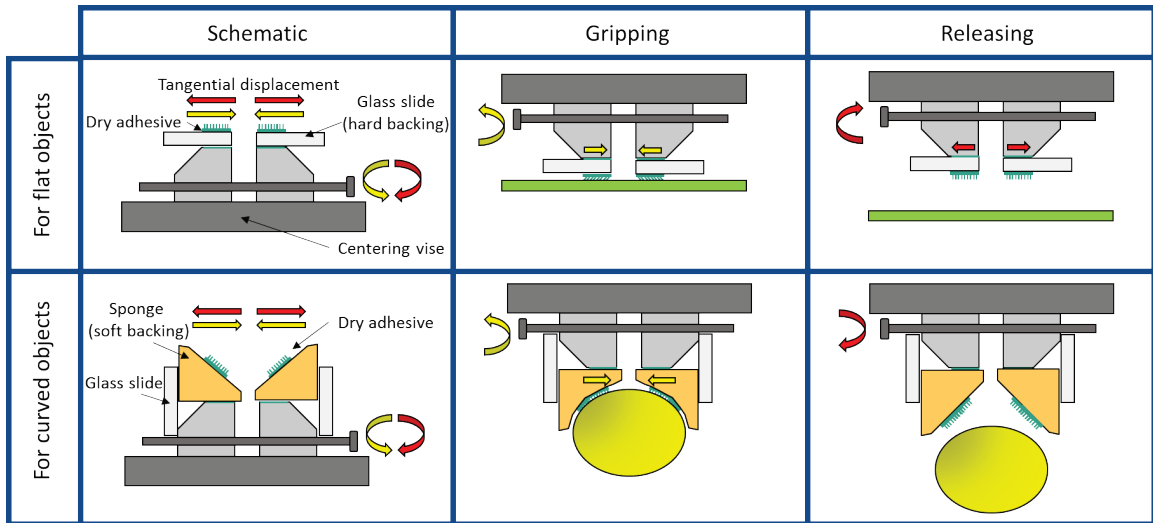
Figure 6-2 – Manipulating (a) iPhone 8 and (b) regular chicken egg with KV1 PVS microstructures assembled on a center-clamping vise fitted to handle flat and curved objects, respectively.

Thinking about future applications, it is also interesting to discuss possible limitations of the proposed technique. One important question is whether this method is scalable. The razor blades used in this study are about 5 cm long, which limits one dimension of the drawing array, while the other dimension is built up by stacking the blades together. However, if we keep using blades, they can be stacked in a two-dimensional matrix, and if other drawing elements are employed, they can be made to have much greater length. Thus, if the drawing elements are properly aligned with the substrate, on top of which the curing polymer is spread, the drawn adhesive microstructure can easily reach the scale of meters, while the process time depends on the curing time of the polymer.

6.4 Future Directions

The ultimate goal in studying dry adhesion is to make a versatile bioinspired adhesive that has the following features: (a) significant attachment force but negligible detachment force, (b) insensitivity to the counterface chemistry and roughness, (c) high repeatability with self-cleaning effect, and (d) capability of being manufactured easily and cost-efficiently. Towards this ultimate goal, the followings directions can be explored further.

1. Environmental effects: although dry adhesives will be mostly used in ambient conditions, it is also important to understand how the surrounding atmosphere changes will affect the attachment performance of our shear-activated adhesive. When used outdoor during Winter or Summer, the temperature and humidity can play critical roles. In addition, adhesive surfaces can be contaminated by dust. Hence, it will be interesting to see how the temperature, humidity, and contamination affect the attachment performance. This can help making dry adhesives more robust, or guiding corrective measures to reduce negative environmental effects.

2. Contact splitting: because it was found that the counterface roughness has a serious negative effect but can be mitigated by contact splitting, the latter should be studied more extensively. While contact splitting improves adaptivity to rough surfaces, it can also lead to self-stickiness. Geckos avoid this issue by using a material with high Young's modulus of above 1 GPa, and insects sometimes possess special surface bumps on a back side of their adhesive hairs.

However, these solutions are currently hardly technically possible, so other directions have to be investigated.

3. New designs: given that the mushroom- and wedge/flap-shaped adhesive microstructures have been extensively studied over the past decade, most of the future commercial dry adhesive will be based on these two geometries. However, while these structures can revolutionize the field of temporary attachment, their performance will eventually reach the inherent limit associated with these geometries. In this regard, new structural shapes can be architected to introduce next generations of dry adhesives. These future designs can be developed using assistance of other new research fields such as machine learning.

REFERENCES

1.   Dai, Z., J. Tong, and L. Ren, *Researches and developments of biomimetics in tribology.* Chinese Science Bulletin, 2006. **51**(22): p. 2681-2689.

2.   Eadie, L. and T.K. Ghosh, *Biomimicry in textiles: past, present and potential. An overview.* Journal of the royal society interface, 2011. **8**(59): p. 761-775.

3.   Trask, R. and I. Bond, *Biomimetic self-healing of advanced composite structures using hollow glass fibres.* Smart Materials and Structures, 2006. **15**(3): p. 704.

4.   Menon, C., M. Murphy, and M. Sitti. *Gecko inspired surface climbing robots.* in *Robotics and Biomimetics, 2004. ROBIO 2004. IEEE International Conference on.* 2004. IEEE.

5.   Bhushan, B., K. Koch, and Y.C. Jung, *Biomimetic hierarchical structure for self-cleaning.* Applied Physics Letters, 2008. **93**(9): p. 093101.

6.   Yang, S., et al., *Functional biomimetic microlens arrays with integrated pores.* Advanced Materials, 2005. **17**(4): p. 435-438.

7.   Autumn, K., et al., *Adhesive force of a single gecko foot-hair.* Nature, 2000. **405**: p. 681-685.

8.   Arzt, E., S. Gorb, and R. Spolenak, *From micro to nano contacts in biological attachment devices.* Proceedings of the National Academy of Sciences, 2003. **100**(19): p. 10603-10606.

9.   Autumn, K., et al., *Evidence for van der Waals adhesion in gecko setae.* Proceedings of the National Academy of Sciences, 2002. **99**(19): p. 12252-12256.

10.   Mengüç, Y., et al., *Gecko-inspired controllable adhesive structures applied to micromanipulation.* Advanced Functional Materials, 2012. **22**(6): p. 1246-1254.

11.   Liu, Y., M. Xu, and Y. Cao, *Research, design and experiment of end effector for wafer transfer robot.* Industrial Robot: An International Journal, 2012. **39**(1): p. 79-91.

12.   Varenberg, M., et al., *Elastomer vs. ceramic in cyclically loaded contact: What wears less?* Tribology International, 2016. **103**: p. 641-646.

13.   Korczynski, E., *Design challenges in vacuum robotics.* Solid State Technology, 1996. **39**(10): p. 62-68.

14.   Scherge, M., S.N. Gorb, and S. Gorb, *Biological micro-and nanotribology.* 2001: Springer Science & Business Media.

15. Varenberg, M., N.M. Pugno, and S.N. Gorb, *Spatulate structures in biological fibrillar adhesion.* Soft Matter, 2010. **6**(14): p. 3269-3272.

16. Hansen, W.R. and K. Autumn, *Evidence for self-cleaning in gecko setae.* Proceedings of the National Academy of Sciences, 2005. **102**(2): p. 385-389.

17. Gao, H., et al., *Mechanics of hierarchical adhesion structures of geckos.* Mechanics of Materials, 2005. **37**(2-3): p. 275-285.

18. Autumn, K., et al., *Dynamics of geckos running vertically.* Journal of experimental biology, 2006. **209**(2): p. 260-272.

19. Bullock, J.M., P. Drechsler, and W. Federle, *Comparison of smooth and hairy attachment pads in insects: friction, adhesion and mechanisms for direction-dependence.* Journal of Experimental Biology, 2008. **211**(20): p. 3333-3343.

20. Spolenak, R., S. Gorb, and E. Arzt, *Adhesion design maps for bio-inspired attachment systems.* Acta biomaterialia, 2005. **1**(1): p. 5-13.

21. Gorb, E. and S. Gorb, *Effects of surface topography and chemistry of Rumex obtusifolius leaves on the attachment of the beetle Gastrophysa viridula.* Entomologia Experimentalis et Applicata, 2009. **130**(3): p. 222-228.

22. Gamble, T., et al., *Repeated origin and loss of adhesive toepads in geckos.* PLoS One, 2012. **7**(6): p. e39429.

23. Pattantyus-Abraham, A., J. Krahn, and C. Menon, *Recent advances in nanostructured biomimetic dry adhesives.* Frontiers in bioengineering and biotechnology, 2013. **1**: p. 22.

24. Gluckman, P.D., et al., *Environmental influences during development and their later consequences for health and disease: implications for the interpretation of empirical studies.* Proceedings of the Royal Society B: Biological Sciences, 2005. **272**(1564): p. 671-677.

25. Kreft, H. and W. Jetz, *Global patterns and determinants of vascular plant diversity.* Proceedings of the National Academy of Sciences, 2007. **104**(14): p. 5925-5930.

26. Zhou, M., et al., *Recent advances in gecko adhesion and friction mechanisms and development of gecko-inspired dry adhesive surfaces.* Friction, 2013. **1**(2): p. 114-129.

27. O'Rorke, R.D., T.W. SteelE, and H. Taylor, *Bioinspired fibrillar adhesives: a review of analytical models and experimental evidence for adhesion enhancement by surface patterns.* Journal of Adhesion Science and Technology, 2016. **30**(4): p. 362-391.

28. Gorb, S., et al., *Biomimetic mushroom-shaped fibrillar adhesive microstructure.* Journal of The Royal Society Interface, 2006. **4**(13): p. 271-275.

29. Glassmaker, N.J., et al., *Biologically inspired crack trapping for enhanced adhesion.* Proceedings of the National Academy of Sciences, 2007. **104**(26): p. 10786-10791.

30. Parness, A., et al., *A microfabricated wedge-shaped adhesive array displaying gecko-like dynamic adhesion, directionality and long lifetime.* Journal of the Royal Society Interface, 2009. **6**(41): p. 1223-1232.

31. Jin, K., et al., *Design and fabrication of gecko-inspired adhesives.* Langmuir, 2012. **28**(13): p. 5737-5742.

32. Day, P., et al., *Microwedge machining for the manufacture of directional dry adhesives.* Journal of Micro and Nano-Manufacturing, 2013. **1**(1): p. 011001.

33. Kasem, H., A. Tsipenyuk, and M. Varenberg, *Biomimetic wall-shaped hierarchical microstructure for gecko-like attachment.* Soft matter, 2015. **11**(15): p. 2909-2915.

34. Geim, A.K., et al., *Microfabricated adhesive mimicking gecko foot-hair.* Nature materials, 2003. **2**(7): p. 461.

35. Sitti, M. and R.S. Fearing. *Nanomolding based fabrication of synthetic gecko foot-hairs.* in *Proceedings of the 2nd IEEE Conference on Nanotechnology.* 2002. IEEE.

36. Greiner, C., A. del Campo, and E. Arzt, *Adhesion of bioinspired micropatterned surfaces: effects of pillar radius, aspect ratio, and preload.* Langmuir, 2007. **23**(7): p. 3495-3502.

37. Kim, S. and M. Sitti, *Biologically inspired polymer microfibers with spatulate tips as repeatable fibrillar adhesives.* Applied physics letters, 2006. **89**(26): p. 261911.

38. Zhou, M., et al., *Controllable interfacial adhesion applied to transfer light and fragile objects by using gecko inspired mushroom-shaped pillar surface.* ACS applied materials & interfaces, 2013. **5**(20): p. 10137-10144.

39. Yi, H., et al., *Bio-inspired adhesive systems for next-generation green manufacturing.* International Journal of Precision Engineering and Manufacturing-Green Technology, 2014. **1**(4): p. 347-351.

40. Tao, D., et al., *Controllable anisotropic dry adhesion in vacuum: gecko inspired wedged surface fabricated with ultraprecision diamond cutting.* Advanced Functional Materials, 2017. **27**(22): p. 1606576.

41. Kim, S., et al. *Whole body adhesion: hierarchical, directional and distributed control of adhesive forces for a climbing robot.* in *Robotics and Automation, 2007 IEEE International Conference on.* 2007. IEEE.

42. Hawkes, E.W., et al., *Human climbing with efficiently scaled gecko-inspired dry adhesives.* Journal of The Royal Society Interface, 2015. **12**(102): p. 20140675.

43. Jiang, H., et al., *A robotic device using gecko-inspired adhesives can grasp and manipulate large objects in microgravity.* Science Robotics, 2017. **2**(7): p. eaan4545.

44. Ronzhin, A. *Connecting Gripping Mechanism Based on Iris Diaphragm for Modular Autonomous Robots*. in *Interactive Collaborative Robotics: 4th International Conference, ICR 2019, Istanbul, Turkey, August 20–25, 2019, Proceedings*. 2019. Springer.

45. Sameoto, D. and C. Menon, *Recent advances in the fabrication and adhesion testing of biomimetic dry adhesives.* Smart Materials and Structures, 2010. **19**(10): p. 103001.

46. Brodoceanu, D., et al., *Hierarchical bioinspired adhesive surfaces—a review.* Bioinspiration & biomimetics, 2016. **11**(5): p. 051001.

47. Sahay, R., et al., *A state-of-the-art review and analysis on the design of dry adhesion materials for applications such as climbing micro-robots.* Rsc Advances, 2015. **5**(63): p. 50821-50832.

48. Kaneko, A., H. Kobayashi, and N. Moronuki. *Surface Micro-Structuring Using Polymer Elongation*. in *Key Engineering Materials*. 2010. Trans Tech Publ.

49. Hwang, I., et al., *Fabrication of bioinspired dry adhesives by CNC machining and replica molding.* International Journal of Precision Engineering and Manufacturing, 2017. **18**(9): p. 1239-1244.

50. Nain, A.S. and M. Sitti. *3-D nano-fiber manufacturing by controlled pulling of liquid polymers using nano-probes*. in *2003 Third IEEE Conference on Nanotechnology, 2003. IEEE-NANO 2003*. 2003. IEEE.

51. Nain, A.S., C. Amon, and M. Sitti, *Proximal probes based nanorobotic drawing of polymer micro/nanofibers.* IEEE Transactions on Nanotechnology, 2006. **5**(5): p. 499-510.

52. Jeong, H.E., et al., *Stretched polymer nanohairs by nanodrawing.* Nano letters, 2006. **6**(7): p. 1508-1513.

53. Berry, S.M., et al., *Characterization of micromanipulator-controlled dry spinning of micro- and sub-microscale polymer fibers.* Journal of Micromechanics and Microengineering, 2006. **16**(9): p. 1825-1832.

54. Harfenist, S.A., et al., *Direct drawing of suspended filamentary micro- and nanostructures from liquid polymers.* Nano Letters, 2004. **4**(10): p. 1931-1937.

55. Kendall, K., *Thin-film peeling-the elastic term.* Journal of Physics D: Applied Physics, 1975. **8**(13): p. 1449.

56. Tian, Y., et al., *Adhesion and friction in gecko toe attachment and detachment.* Proceedings of the National Academy of Sciences, 2006. **103**(51): p. 19320-19325.

57. Autumn, K. and N. Gravish, *Gecko adhesion: evolutionary nanotechnology.* Philosophical Transactions of the Royal Society A: Mathematical, Physical and Engineering Sciences, 2008. **366**(1870): p. 1575-1590.

58. Wang, Y., et al., *Adhesion circle: A new approach to better characterize directional gecko-inspired dry adhesives.* ACS applied materials & interfaces, 2017. **9**(3): p. 3060-3067.

59. Huber, G., et al., *Influence of surface roughness on gecko adhesion.* Acta biomaterialia, 2007. **3**(4): p. 607-610.

60. Gillies, A.G., et al., *Gecko toe and lamellar shear adhesion on macroscopic, engineered rough surfaces.* Journal of Experimental Biology, 2014. **217**(2): p. 283-289.

61. Hui, C.-Y., N. Glassmaker, and A. Jagota, *How compliance compensates for surface roughness in fibrillar adhesion.* The Journal of Adhesion, 2005. **81**(7-8): p. 699-721.

62. Cañas, N., et al., *Effect of nano-and micro-roughness on adhesion of bioinspired micropatterned surfaces.* Acta biomaterialia, 2012. **8**(1): p. 282-288.

63. Bauer, C.T., et al., *Hierarchical macroscopic fibrillar adhesives: In situ study of buckling and adhesion mechanisms on wavy substrates.* Bioinspiration & biomimetics, 2015. **10**(6): p. 066002.

64. Barreau, V., et al., *Fibrillar elastomeric micropatterns create tunable adhesion even to rough surfaces.* Advanced Functional Materials, 2016. **26**(26): p. 4687-4694.

65. Asbeck, A., et al. *Climbing rough vertical surfaces with hierarchical directional adhesion.* in *Robotics and Automation, 2009. ICRA'09. IEEE International Conference on.* 2009. IEEE.

66. Yu, J., et al., *Friction and adhesion of gecko-inspired PDMS flaps on rough surfaces.* Langmuir, 2012. **28**(31): p. 11527-11534.

67. Kasem, H. and M. Varenberg, *Effect of counterface roughness on adhesion of mushroom-shaped microstructure.* Journal of The Royal Society Interface, 2013. **10**(87): p. 20130620.

68.   Ruffatto III, D., A. Parness, and M. Spenko, *Improving controllable adhesion on both rough and smooth surfaces with a hybrid electrostatic/gecko-like adhesive.* Journal of The Royal Society Interface, 2014. **11**(93): p. 20131089.

69.   Kasem, H. and Y. Cohen, *Effect of counterface roughness on the friction of bionic wall-shaped microstructures for gecko-like attachments.* Bioinspiration & biomimetics, 2017. **12**(4): p. 046010.

70.   Bai, Y., et al., *Enhancement of Friction against a Rough Surface by a Ridge–Channel Surface Microstructure.* Langmuir, 2015. **31**(27): p. 7581-7589.

71.   Persson, B. and S. Gorb, *The effect of surface roughness on the adhesion of elastic plates with application to biological systems.* The Journal of chemical physics, 2003. **119**(21): p. 11437-11444.

72.   Gao, H. and H. Yao, *Shape insensitive optimal adhesion of nanoscale fibrillar structures.* Proceedings of the National Academy of Sciences of the United States of America, 2004. **101**(21): p. 7851-7856.

73.   Federle, W., *Why are so many adhesive pads hairy?* Journal of Experimental Biology, 2006. **209**(14): p. 2611-2621.

74.   Kamperman, M., et al., *Functional adhesive surfaces with "gecko" effect: The concept of contact splitting.* Advanced Engineering Materials, 2010. **12**(5): p. 335-348.

75.   Varenberg, M., et al., *Geometry-controlled adhesion: revisiting the contact splitting hypothesis.* Applied Physics A, 2011. **103**(4): p. 933-938.

76.   Dalet, P., E. Papon, and J.-J. Villenave, *Surface free energy of polymeric materials: relevancy of conventional contact angle data analyses.* Journal of adhesion science and technology, 1999. **13**(8): p. 857-870.

77.   Comyn, J., D. Blackley, and L. Harding, *Contact angles of liquids on films from emulsion adhesives, and correlation with the durability of adhesive bonds to polystyrene.* International journal of adhesion and adhesives, 1993. **13**(3): p. 163-171.

78.   Hiller, U., *Untersuchungen zum Feinbau und zur Funktion der Haftborsten von Reptilien.* Zeitschrift für Morphologie der Tiere, 1968. **62**(4): p. 307-362.

79.   Stark, A.Y., et al., *Surface wettability plays a significant role in gecko adhesion underwater.* Proceedings of the National Academy of Sciences, 2013. **110**(16): p. 6340-6345.

80.   Autumn, K. and A.M. Peattie, *Mechanisms of adhesion in geckos.* Integrative and Comparative Biology, 2002. **42**(6): p. 1081-1090.

81.   Autumn, K. and J. Puthoff, *Properties, principles, and parameters of the gecko adhesive system*, in *Biological adhesives*. 2016, Springer. p. 245-280.

82.   Radinovsky, S. and G. Krantz, *The use of Fluon to prevent the escape of stored-product insects from Glass containers.* Journal of Economic Entomology, 1962. **55**: p. 815-816.

83.   Ge, L., et al., *Carbon nanotube-based synthetic gecko tapes.* Proceedings of the National Academy of Sciences of the United States of America, 2007. **104**(26): p. 10792-10795.

84.   Jańczuk, B. and T. Białłopiotrowicz, *Surface free-energy components of liquids and low energy solids and contact angles.* Journal of Colloid and Interface Science, 1989. **127**(1): p. 189-204.

85.   Li, X., et al., *Recent developments in gecko-inspired dry adhesive surfaces from fabrication to application.* Surface Topography: Metrology and Properties, 2019. **7**(2): p. 023001.

86.   Kalpakjian, S., *Manufacturing processes for engineering materials.* 1984: Pearson Education India.

87.   Chary, S., J. Tamelier, and K. Turner, *A microfabricated gecko-inspired controllable and reusable dry adhesive.* Smart Materials and Structures, 2013. **22**(2): p. 025013.

88.   Kim, T.i., et al., *Stooped nanohairs: geometry‑controllable, unidirectional, reversible, and robust gecko‑like dry adhesive.* Advanced Materials, 2009. **21**(22): p. 2276-2281.

89.   Im, H.S., et al., *Highly durable and unidirectionally stooped polymeric nanohairs for gecko-like dry adhesive.* Nanotechnology, 2015. **26**(41): p. 415301.

90.   Stark, A.Y., et al., *The effect of temperature and humidity on adhesion of a gecko-inspired adhesive: implications for the natural system.* Scientific reports, 2016. **6**: p. 30936.

91.   Ma, S., et al., *Gecko‑Inspired but Chemically Switched Friction and Adhesion on Nanofibrillar Surfaces.* Small, 2015. **11**(9-10): p. 1131-1137.

92.   Kwak, J.-S. and T.-W. Kim, *A review of adhesion and friction models for gecko feet.* International Journal of Precision Engineering and Manufacturing, 2010. **11**(1): p. 171-186.

93.   Niewiarowski, P.H., et al., *Sticky gecko feet: the role of temperature and humidity.* PloS one, 2008. **3**(5): p. e2192.

94.   Watson, G.S., et al., *A gecko skin micro/nano structure–A low adhesion, superhydrophobic, anti-wetting, self-cleaning, biocompatible, antibacterial surface.* Acta biomaterialia, 2015. **21**: p. 109-122.

95.   Kim, S., E. Cheung, and M. Sitti, *Wet self-cleaning of biologically inspired elastomer mushroom shaped microfibrillar adhesives.* Langmuir, 2009. **25**(13): p. 7196-7199.

96.   Mengüç, Y., et al., *Staying sticky: contact self-cleaning of gecko-inspired adhesives.* Journal of The Royal Society Interface, 2014. **11**(94): p. 20131205.

97.   Lee, J. and R.S. Fearing, *Contact self-cleaning of synthetic gecko adhesive from polymer microfibers.* Langmuir, 2008. **24**(19): p. 10587-10591.

98.   Sethi, S., et al., *Gecko-inspired carbon nanotube-based self-cleaning adhesives.* Nano letters, 2008. **8**(3): p. 822-825.

99.   Xu, Q., et al., *Biomimetic self-cleaning surfaces: synthesis, mechanism and applications.* Journal of the Royal Society Interface, 2016. **13**(122): p. 20160300.

100.   Alizadehyazdi, V., A. Simaite, and M. Spenko, *Evaluation of Material Properties for Practical Microstructured Adhesives: Low Dust Adhesion and High Shear Strength.* ACS applied materials & interfaces, 2019. **11**(8): p. 8654-8666.

101.   Alizadehyazdi, V., et al. *Ultrasonic and Electrostatic Self-Cleaning Microstructured Adhesives for Robotic Grippers.* in *2018 IEEE/RSJ International Conference on Intelligent Robots and Systems (IROS).* 2018. IEEE.

102.   Autumn, K., et al., *Frictional adhesion: a new angle on gecko attachment.* Journal of Experimental Biology, 2006. **209**(18): p. 3569-3579.

103.   Pesika, N.S., et al., *Peel-zone model of tape peeling based on the gecko adhesive system.* The Journal of Adhesion, 2007. **83**(4): p. 383-401.

104.   Wang, Y., et al., *Fabrication of well-defined mushroom-shaped structures for biomimetic dry adhesive by conventional photolithography and molding.* ACS applied materials & interfaces, 2014. **6**(4): p. 2213-2218.

105.   Murarash, B. and M. Varenberg, *Tribometer for in situ scanning electron microscopy of microstructured contacts.* Tribology letters, 2011. **41**(2): p. 319-323.

106.   Peressadko, A. and S.N. Gorb, *When less is more: Experimental evidence for tenacity enhancement by division of contact area.* Journal of Adhesion, 2004. **80**(4): p. 247-261.

107.   Kim, J.-K. and M. Varenberg, *Drawing-Based Manufacturing of Shear-Activated Reversible Adhesives.* ACS Applied Materials & Interfaces, 2020. **12**(17): p. 20075-20083.

108.   Landau, L. and B. Levich, *Dragging of a liquid by a moving plate*, in *Dynamics of Curved Fronts*. 1988, Elsevier. p. 141-153.

109.   Quéré, D., *Fluid coating on a fiber.* Annual Review of Fluid Mechanics, 1999. **31**(1): p. 347-384.

110.   Brinker, C.J., *Dip coating*, in *Chemical Solution Deposition of Functional Oxide Thin Films*. 2013, Springer. p. 233-261.

111.   Rio, E. and F. Boulogne, *Withdrawing a solid from a bath: How much liquid is coated?* Advances in Colloid and Interface science, 2017. **247**: p. 100-114.

112.   Yang, S., K. Khare, and P.C. Lin, *Harnessing surface wrinkle patterns in soft matter.* Advanced Functional Materials, 2010. **20**(16): p. 2550-2564.

113.   Uchiyama, H., W. Namba, and H. Kozuka, *Spontaneous formation of linear striations and cell-like patterns on dip-coating titania films prepared from alkoxide solutions.* Langmuir, 2010. **26**(13): p. 11479-11484.

114.   Sutera, S.P. and R. Skalak, *The history of Poiseuille's law.* Annual review of fluid mechanics, 1993. **25**(1): p. 1-20.

115.   Shou, D., L. Ye, and J. Fan, *The fastest capillary flow under gravity.* Applied Physics Letters, 2014. **104**(23): p. 231602.

116.   Kim, O. and J. Nam, *Confinement effects in dip coating.* Journal of Fluid Mechanics, 2017. **827**: p. 1-30.

117.   Smit, W.J., et al., *Stress field inside the bath determines dip coating with yield-stress fluids in cylindrical geometry.* Physical Review Letters, 2019. **123**(14): p. 148002.

118.   He, Z., et al., *Adhesion and Friction Enhancement of Film-Terminated Structures against Rough Surfaces.* Tribology Letters, 2017. **65**(4): p. 161.

119.   Kligerman, Y. and M. Varenberg, *Elimination of stick-slip motion in sliding of split or rough surface.* Tribology Letters, 2014. **53**(2): p. 395-399.

120.   Heepe, L., S. Raguseo, and S.N. Gorb, *An experimental study of double-peeling mechanism inspired by biological adhesive systems.* Applied Physics A, 2017. **123**(2): p. 124.

121.   Zhao, B., et al., *Adhesion and friction force coupling of gecko setal arrays: implications for structured adhesive surfaces.* Langmuir, 2008. **24**(4): p. 1517-1524.

122. Kim, J.-K. and M. Varenberg, *Biomimetic wall-shaped adhesive microstructure for shear-induced attachment: the effects of pulling angle and preliminary displacement.* Journal of The Royal Society Interface, 2017. **14**(137): p. 20170832.

123. Gorb, S.N., *Visualisation of native surfaces by two-step molding.* Microsc. Today, 2007. **15**: p. 44-46.

124. Greenwood, J. and J.P. Williamson, *Contact of nominally flat surfaces.* Proc. R. Soc. Lond. A, 1966. **295**(1442): p. 300-319.

125. Kalin, M., et al., *Comparing surface topography parameters of rough surfaces obtained with spectral moments and deterministic methods.* Tribology International, 2016. **93**: p. 137-141.

126. Zurek, D.B., S.N. Gorb, and D. Voigt, *Changes in tarsal morphology and attachment ability to rough surfaces during ontogenesis in the beetle Gastrophysa viridula (Coleoptera, Chrysomelidae).* Arthropod structure & development, 2017. **46**(1): p. 130-137.

127. Frost, K.F., S.N. Gorb, and J.O. Wolff, *Adhesion and friction in hunting spiders: The effect of contact splitting on their attachment ability.* Zoologischer Anzeiger, 2018. **273**: p. 231-239.

128. Raja, J., B. Muralikrishnan, and S. Fu, *Recent advances in separation of roughness, waviness and form.* Precision Engineering, 2002. **26**(2): p. 222-235.

129. Vajpayee, S., A. Jagota, and C.-Y. Hui, *Adhesion of a fibrillar interface on wet and rough surfaces.* The Journal of Adhesion, 2010. **86**(1): p. 39-61.

130. Kim, J.-K. and M. Varenberg, *Contact splitting in dry adhesion and friction: reducing the influence of roughness.* Beilstein Journal of Nanotechnology, 2019. **10**(1): p. 1-8.

131. Owens, D.K. and R. Wendt, *Estimation of the surface free energy of polymers.* Journal of applied polymer science, 1969. **13**(8): p. 1741-1747.

132. Cappelletti, G., et al., *Wettability of bare and fluorinated silanes: a combined approach based on surface free energy evaluations and dipole moment calculations.* Journal of colloid and interface science, 2013. **389**(1): p. 284-291.

133. Das, S.C., et al., *Determination of the polar and total surface energy distributions of particulates by inverse gas chromatography.* Langmuir, 2011. **27**(2): p. 521-523.

134. Siciński, M., et al., *Low-temperature plasma modification of carbon nanofillers for improved performance of advanced rubber composites.* Polymer Bulletin, 2020. **77**(2): p. 1015-1048.

135. Marmur, A., *Wetting on hydrophobic rough surfaces: to be heterogeneous or not to be?* Langmuir, 2003. **19**(20): p. 8343-8348.

136. Greiner, C., et al., *Contact splitting and the effect of dimple depth on static friction of textured surfaces.* ACS applied materials & interfaces, 2014. **6**(11): p. 7986-7990.

137. Fuller, K. and D. Tabor, *The effect of surface roughness on the adhesion of elastic solids.* Proceedings of the Royal Society of London. A. Mathematical and Physical Sciences, 1975. **345**(1642): p. 327-342.

138. Acito, V., et al., *Adhesive contact of model randomly rough rubber surfaces.* Tribology Letters, 2019. **67**(2): p. 54.

139. Seo, S., et al., *Anisotropic adhesion of micropillars with spatula pads.* ACS applied materials & interfaces, 2014. **6**(3): p. 1345-1350.

140. Sameoto, D. and C. Menon, *Direct molding of dry adhesives with anisotropic peel strength using an offset lift-off photoresist mold.* Journal of Micromechanics and Microengineering, 2009. **19**(11): p. 115026.

141. Kovalev, A.E., M. Varenberg, and S.N. Gorb, *Wet versus dry adhesion of biomimetic mushroom-shaped microstructures.* Soft Matter, 2012. **8**(29): p. 7560-7566.

142. Daltorio, K.A., et al., *A robot that climbs walls using micro-structured polymer feet*, in *Climbing and walking robots*. 2006, Springer. p. 131-138.

143. Song, J., Y. Mengüç, and M. Sitti, *Enhanced fabrication and characterization of gecko-inspired mushroom-tipped microfiber adhesives.* Journal of adhesion science and technology, 2013. **27**(17): p. 1921-1932.

144. Murphy, M.P., S. Kim, and M. Sitti, *Enhanced adhesion by gecko-inspired hierarchical fibrillar adhesives.* ACS applied materials & interfaces, 2009. **1**(4): p. 849-855.

145. Kendall, K., *The adhesion and surface energy of elastic solids.* Journal of Physics D: Applied Physics, 1971. **4**(8): p. 1186.

146. Israelachvili, J.N., *Intermolecular and surface forces*. 2011: Academic press.

147. Jin, K., et al., *Biomimetic bidirectional switchable adhesive inspired by the gecko.* Advanced Functional Materials, 2014. **24**(5): p. 574-579.

148. Li, Y., D. Sameoto, and C. Menon. *Properties validation of an anisotropic dry adhesion designed for legged climbing robots*. in *2009 IEEE International Conference on Robotics and Biomimetics (ROBIO)*. 2009. IEEE.

149. Lee, J., et al., *Gecko-inspired combined lamellar and nanofibrillar array for adhesion on nonplanar surface.* Langmuir, 2009. **25**(21): p. 12449-12453.

150. Lee, J., R.S. Fearing, and K. Komvopoulos, *Directional adhesion of gecko-inspired angled microfiber arrays.* Applied Physics Letters, 2008. **93**(19): p. 191910.

151. Zhang, H., et al., *Fabrication and adhesion of hierarchical micro-seta.* Chinese Science Bulletin, 2012. **57**(11): p. 1343-1349.

152. Asbeck, A., et al. *Climbing rough vertical surfaces with hierarchical directional adhesion.* in *2009 IEEE International Conference on Robotics and Automation.* 2009. IEEE.